

**Study on Formation and Characterization of  
Fe-based Silicide Nanodots on Ultrathin SiO<sub>2</sub> for  
Functional Memories**

**Hai ZHANG**

# **Ph. D THESIS**

## **Study on Formation and Characterization of Fe-based Silicide Nanodots on Ultrathin SiO<sub>2</sub> for Functional Memories**

**Hai ZHANG**

**2016**

**Department of Electrical Engineering and Computer Science**

**Graduate School of Engineering**

**Nagoya University**

# Acknowledgements

This dissertation entitled “Study on Formation and Characterization of Fe-based Silicide Nanodots on Ultrathin SiO<sub>2</sub> for Functional Memories” is the author’s research achievements in Ph. D program in Department of Electrical Engineering and Computer Science, Graduate School of Engineering, Nagoya University, Japan.

First and foremost, I would like to express my sincere gratitude to my supervisor Prof. Seiichi Miyazaki and Associate Prof. Katsunori Makihara for offering a great research environment and their constructive guidance. Here, I have my utmost respect for their vast knowledge, experience, and patience.

I appreciate Profs. Masaru Hori, Hiroataka Toyoda, Hirokazu Tatsuoka and Masaya Ichimura for providing valuable comments on my PhD dissertation. I would like to thank Designated Assistant Prof. Akio Ohta, Prof. Satoshi Iwata, Associate Prof. Takeshi Kato, Assistant Prof. Daiki Oshima, and Dr. Mitsuhsa Ikeda for beneficial discussions and experimental supports.

My gratitude also goes to all of members in Miyazaki’s laboratory not only for their help in my research, but also for growth together in Miyazaki’s laboratory for three years. Especially, I would like to thank Daichi Takeuchi, Ryo Fukuoka, and Yuuki Kabeya for their research cooperation and communication.

I am grateful to the NGK Foundation for International Students Scholarship for two years support, which helped me to accomplish this work.

Finally, I would like to thank family including parents, sisters, my wife, and my son for their love, support and encouragement in all of my life.

*December 2015, Hai ZHANG*

# Contents

|   |    |
|---|----|
| <b>Acknowledgements</b> .....   | I  |
| <b>Chapter 1 Introduction</b> .....   | 1  |
| 1.1 Background and motivation .....   | 1  |
| 1.2 Physical properties of Fe-silicides .....   | 3  |
| 1.3 Fabrication processes of Fe-silicide nanostructures .....   | 6  |
| 1.4 Applications of Fe-silicide nanodots .....  | 7  |
| 1.5 Purpose of this work .....  | 8  |
| References  |    |
| <br>  |    |
| <b>Chapter 2 Formation processes and characterization methods</b> .....                                   | 12 |
| 2.1 Formation methods of metallic nanodots .....  | 12 |
| 2.2 Remote H <sub>2</sub> plasma induced formation of metallic nanodots on SiO <sub>2</sub> .....         | 14 |
| 2.3 Characterization methods .....  | 19 |
| 2.3.1 Atomic Force Microscope (AFM) .....   | 19 |
| 2.3.2 Alternating Gradient-field Magnetometer (AGM) .....   | 26 |
| 2.3.3 X-ray Photoelectron Spectroscopy (XPS) .....  | 27 |
| 2.3.4 Raman Scattering Spectroscopy .....   | 30 |
| 2.3.5 X-ray Diffraction (XRD) .....   | 31 |
| References  |    |
| <br>  |    |
| <b>Chapter 3 Formation of Fe nanodots on SiO<sub>2</sub> induced by remote H<sub>2</sub> plasma</b> ..... | 37 |
| 3.1 Introduction .....  | 38 |

|       |  |    |
|-------|--|----|
| 3.2   | Experimental details .....   | 39 |
| 3.3   | Results and discussion .....   | 40 |
| 3.3.1 | Impact of remote H <sub>2</sub> plasma exposure on Fe atom migration on SiO <sub>2</sub> ... | 40 |
| 3.3.2 | Formation mechanism of Fe nanodots induced by remote H <sub>2</sub> plasma ...               | 53 |
| 3.3.3 | Magnetic properties of Fe nanodots .....   | 54 |
| 3.4   | Conclusions .....  | 57 |
|       | References   |    |

**Chapter 4 Formation of Fe-silicide nanodots on SiO<sub>2</sub> from Fe/Si/Fe trilayer stacks by remote H<sub>2</sub> plasma exposure .....**

|       |  |    |
|-------|--|----|
| 4.1   | Introduction .....   | 61 |
| 4.2   | Experimental procedure .....   | 63 |
| 4.3   | Results and discussion .....   | 64 |
| 4.3.1 | Evaluation of chemical composition and bonding features of nanodots ..         | 64 |
| 4.3.2 | Structural characterization of nanodots .....                                  | 68 |
| 4.3.3 | Charging and discharging characteristics of β-FeSi <sub>2</sub> nanodots ..... | 70 |
| 4.4   | Conclusions .....  | 73 |
|       | References   |    |

**Chapter 5 Phase controlled formation of Fe<sub>3</sub>Si nanodots .....**

|       |   |    |
|-------|---|----|
| 5.1   | Introduction .....  | 78 |
| 5.2   | Experimental procedure .....  | 80 |
| 5.3   | Results and discussion .....  | 81 |
| 5.3.1 | Impact of H <sub>2</sub> pressure of remote H <sub>2</sub> plasma<br>on Fe <sub>3</sub> Si nanodots formation ..... | 81 |

|  |           |
|--|-----------|
| 5.3.2 Room temperature magnetic properties of Fe <sub>3</sub> Si nanodots..... | 84        |
| 5.4 Conclusions .....  | 91        |
| References   |           |
| <b>Chapter 6 Conclusions</b> .....   | <b>95</b> |
| List of paper and international conference .....                               | 99        |

## **Chapter 1**

### **Introduction**

#### **1.1 Background and motivation**

Since the invention of bipolar transistor by American physicists John Bardeen, Walter Brattain, and William Shockley in 1945 [1], microelectronics based on Si technology has been greatly developed in accordance with the development of advanced information society. As well known, the performance of Si ultralarge scale integration circuits (Si-ULSICs) has been growing exponentially following commonly known "Moore's Law" for decades by continuous downscaling of electronic devices for higher and higher levels of integration [2, 3]. Nowadays, our life is becoming more and more convenient owing to the rapid development of the Si-ULSICs in consumer electronics, national defense, aerospace, communication, industry control, automobile electronics and so on. With the coming of big data age in the future, both faster data processing and larger capacity data storage are urgently required. However, as the integration level of circuits is more and more advanced, the physical problems and limitations become obstacles in many aspects, such as rapidly increasing leakage currents at the gate and source-drain in metal-oxide-semiconductor field-effect transistor (MOSFET)

[4], and the diminishing improvement in the drive current with reduced channel length [5]. In addition, at the high integration level, the power consumption and the signal delay in the interconnect due to an increase in the resistance and capacitance of metal interconnection are also a stumbling block for evolution of ultralarge scale and high-performance chips [4, 6], which are required for data processing and transfer via optical connections. Furthermore, the fundamental process for geometry scaling, photolithography is facing the most significant challenges. Therefore, many constant efforts have been continued to overcome the obstacles to the continued growth of integration level. For instance, new structures that promise better control over the channel current flow to reduce the source-to-drain leakage current, such as, double gate [7], fin-FET [8], ultra-thin body (UTB) silicon-on-insulator (SOI), and metal gate devices, combinations of metal gates and high-k dielectrics [9], have been aggressively pursued. One of alternative promising approach is nanoelectronics which could provide novel unique advantages originating from unique physical properties and phenomena in nanometer-sized structures and materials, such as size effects, quantized energy level, Coulomb blockade phenomena. Some new devices such as single-electron transistor [10–13] and dot floating gate memory [14–18] have attracted considerable interest because these devices can lead to breakthrough of the scaling limitations. In various nanostructures including nanodots (NDs) have unique features different from other nanostructures. For example, semiconducting-NDs are often called artificial atoms, because, like real atoms, they confine electrons to quantized states with discrete energies [19, 20]. Therefore, the application of

semiconducting-NDs as a floating gate to MOSFETs has been attracting much attention because it will lead us to new functionality such as multivalued memory operations even at room temperature [14, 15, 17, 21]. On the other hand, considerable efforts have been concentrated on the charge storage in metallic-NDs embedded in dielectric layers because superior charge retention can be expected for metals with proper work functions [22–24]. Recently, magnetic metal NDs, making use of the spin polarization or magnetic tunneling effect, have attracted considerable interests owing to its potentials for new applications in the future including ultrahigh density magnetic data storage and a novel nonvolatile memory [25–27]. Therefore, the research on NDs as novel materials with unique optical, electrical, and magnetic properties has been extensively performed [16, 17, 26–35]. Among these materials, Fe-silicides are prospective candidate because of the varieties of physical properties depending on their composition and phases.

## **1.2 Physical properties of Fe-silicides**

Over the past decades, the interest in the Fe-Si system was triggered both from a fundamental and a technological point of view. Among the applications, Fe-silicides have found significant interests as materials for magnetic storage devices. The phase diagram of Fe-silicide was delivered as early as 1951. Since then, additional efforts were aimed at further understanding the physics and the chemistry of these compounds, which reveal their properties and lead to the synthesis of new phases.

According to the Fe-Si binary phase diagram shown in Fig. 1.1, when Fe reacted

with Si, it forms numerous stable compounds. These compounds, known as Fe-silicides, are  $\alpha$ -FeSi<sub>2</sub>,  $\beta$ -FeSi<sub>2</sub>, Fe<sub>3</sub>Si, Fe<sub>5</sub>Si<sub>3</sub>, and  $\epsilon$ -FeSi [36–41], and some of their crystal structures are shown in Fig.1.2.

The  $\beta$ -FeSi<sub>2</sub> phase is a direct band gap semiconductor with a band gap of 0.84-0.87eV at room temperature, corresponding to the minimum-absorption window of silica-based fibers making it a potential candidate for the use in near infrared detectors and light emitters. This is the primary reason for the rise in the research interest in Fe-silicides. The crystal structure of  $\beta$ -FeSi<sub>2</sub> is base-centered orthorhombic space group having 48 atoms per unit cell and lattice parameters of  $a=0.986$  nm,  $b=0.779$  nm, and  $c=0.783$  nm. The unit cell has two inequivalent Fe sites, each occupied by 8 atoms as well as two equivalent Si sites with 16 atoms in each [42].

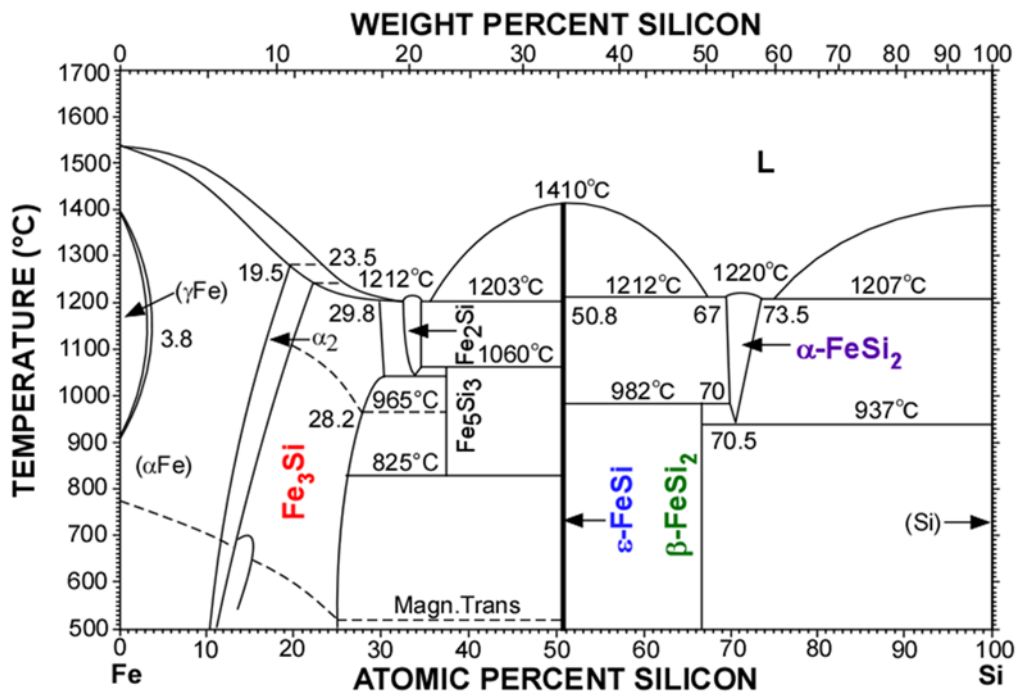
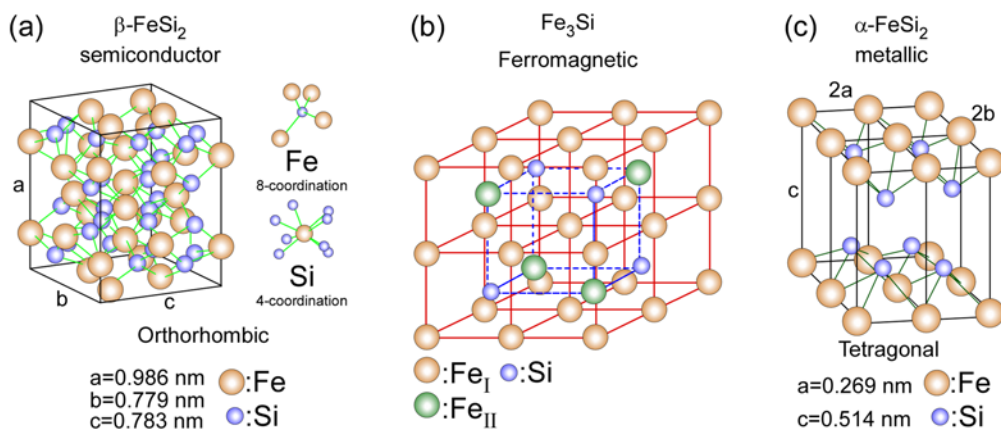


Fig. 1.1. Fe-Si phase diagram.

The ferromagnetic silicide  $\text{Fe}_3\text{Si}$  has a high Curie temperature above  $\sim 800$  K, and it possesses two distinct Fe sites with magnetic moments  $\mu_{\text{Fe}}^{\text{I}} = 2.2\mu_{\text{B}}/\text{atom}$  and  $\mu_{\text{Fe}}^{\text{II}} = 1.35\mu_{\text{B}}/\text{atom}$ , where  $\mu_{\text{B}}$  is the Bohr magneton [43]. Thus,  $\text{Fe}_3\text{Si}$  can be regarded as a Heusler alloy  $\text{Fe}_{\text{II}2}\text{Fe}_{\text{I}}\text{Si}$ , ( $\text{DO}_3$  type), and a candidate for being half-metallic which is spin-polarized at the Fermi level [36, 37]. Therefore,  $\text{Fe}_3\text{Si}$  is an attractive material for Si-based spintronic applications.

The crystal structure of  $\alpha\text{-FeSi}_2$  is tetragonal with lattice parameters of  $a = b = 0.269$  nm and  $c = 0.514$  nm. The composition is not stoichiometric and about 13% of the Fe lattice spots are vacant. The  $\alpha\text{-FeSi}_2$  phase exhibits the metallic electrical conduction. This phase of  $\text{FeSi}_2$  is thought to be unstable at temperatures below  $\sim 937^\circ\text{C}$ .

The monosilicide  $\epsilon\text{-FeSi}$  is commonly referred to as simply  $\text{FeSi}$ . The silicide melts at  $1410^\circ\text{C}$  and has a  $\text{Fe}:\text{Si}=1:1$  stoichiometry with a compositional variation of less than 1 atomic percent.



**Fig. 1.2.** Schematic crystal structures of (a)  $\beta\text{-FeSi}_2$ , (b)  $\text{Fe}_3\text{Si}$ , and (c)  $\alpha\text{-FeSi}_2$ .

### **1.3 Fabrication processes of Fe-silicide nanostructures**

There are many efforts to fabricate Fe-silicide NDs. Typical technique and processes are introduced as below.

Nakamura et al. developed a technique for epitaxially growing Fe-silicide NDs on Si substrates [44]. This method involves an ultrathin SiO<sub>2</sub> layer as thin as a few monolayers on a clean Si surface. A Si layer was predeposited on the ultrathin SiO<sub>2</sub>, and the deposited Si atoms reacted with the SiO<sub>2</sub> films accompanied with voids formation in the ultrathin SiO<sub>2</sub> layer at ~600 °C. The Fe film was subsequently deposited. The Fe film reacted with Si on the formed voids, and Fe-silicide NDs with a dot areal density of 10<sup>10</sup> cm<sup>-2</sup> were formed. However, because the control of the reaction between SiO<sub>2</sub> and predeposited Si is very difficultly, the SiO<sub>2</sub> voids was randomly formed, which led to the non-uniformly size distribution or the continuous film like morphologies.

Sun et al. reported a method for Fe-silicide NDs synthesis in which Fe<sup>+</sup> ions were implanted into the Si substrate and annealing was performed [45]. This provides the atomic mixing and avoids the influence of the wafer surface impurities completely, as they are left at the surface while the silicides form underneath. Thermal annealing was performed during Fe implantation, afterwards, or both. This method has limitations, because the fluence of Fe<sup>+</sup> implantation is restricted and only Si rich phase is preemptively formed.

As mentioned above, there are still some issues such as low areal dot density formation, non-uniformly size distribution and electrically unseparated NDs.

Especially, by using these methods, the control of crystalline phase of NDs and the formation of NDs on SiO<sub>2</sub> are also difficult because the high temperature annealing as high as 600 °C for interdiffusion between the Si substrate and metal-NDs is needed. Considering about device application of Fe-silicide-NDs to Si-based light emitters and spintronic devices, the formation of Fe-silicide NDs on SiO<sub>2</sub> over 10<sup>11</sup>cm<sup>-2</sup> and, control of the size and phase are still matters of research.

#### **1.4 Applications of Fe-silicide nanodots**

Fe-silicides NDs have been applied to some devices. Specifically, semiconducting β-FeSi<sub>2</sub> has been proposed as a promising material that is compatible with Si-based microelectronics technology for optoelectronic applications, such as light-emitting diodes (LEDs) [46–51], photovoltaics [52], and near-infrared (NIR) photodetectors in optical fiber telecommunications [53].

For ferromagnetic Fe<sub>3</sub>Si NDs, due to the spin polarization effect, it has been used for the injection and detection of spin polarized electrons in Spin FET [54]. Some other magnetic properties such as interlayer coupling and magneto resistive (MR) effect have also been found in current-perpendicular-to-the-plane magnetic tunnel junctions (CPP-MTJ) memories [55].

## **1.5 Purpose of this work**

As mentioned in previous sections, considering compatibility with Si-based microelectronics technology, the development of Si-Based NDs is desired. As one of Si-based materials, Fe-silicides have been studied extensively because of their various electronic and magnetic properties depending on their composition and phases. The purpose of this work is to develop an approach of Fe-based silicide nanodot formation to improve the performance of Si-based nanoelectronic devices and innovate the technologies for Si-ULSI. In this work, we focused on the formation of semiconducting and ferromagnetic phase Fe-silicide NDs by controlling the phase structures of Fe-silicide, and characterization of their physical properties.

---

## References

- [1] J. Bardeen and W. H. Brattain, *Phys. Rev.* **74**, 230 (1948).
- [2] A. Hirohata and K. Takanashi, *J. Phys. D. Appl. Phys.* **47**, 193001 (2014).
- [3] J. Liu, M. Beals, J. Michel, and L. Kimerling, in *ECS Trans.*, edited by Intergovernmental Panel on Climate Change (ECS, Cambridge, 2009), pp. 17–28.
- [4] S. Luryi, J. Xu, and A. Zaslavsky, in *Futur. Trends Microelectron.* (John Wiley & Sons, Inc., Hoboken, NJ, USA, 2007), pp. 203–211.
- [5] S.-H. O. S.-H. Oh, D. Monroe, and J. M. Hergenrother, *IEEE Electron Device Lett.* **21**, 3 (2000).
- [6] D. A. B. Miller, *IEEE J. Sel. Top. Quantum Electron.* **6**, 1312 (2000).
- [7] P. Beckett, in *2002 IEEE Int. Conf. Field-Programmable Technol. 2002. (FPT). Proceedings.* (IEEE, 2002), pp. 260–267.
- [8] R. Katsumata, N. Tsuda, J. Idebuchi, M. Kondo, N. Aoki, et al., in *2003 Symp. VLSI Technol. Dig. Tech. Pap. (IEEE Cat. No.03CH37407)* (Japan Soc. Applied Phys, 2003), pp. 61–62.
- [9] K. Mistry, C. Allen, C. Auth, B. Beattie, D. Bergstrom, et al., *Tech. Dig. - Int. Electron Devices Meet. IEDM 247* (2007).
- [10] M. Kastner, *Rev. Mod. Phys.* **64**, 849 (1992).
- [11] D. L. Klein, R. Roth, A. K. L. Lim, A. P. Alivisatos, and P. L. McEuen, *Nature* **389**, 699 (1997).
- [12] H. Ishikuro and T. Hiramoto, *Appl. Phys. Lett.* **71**, 3691 (1997).
- [13] Y. Takahashi, A. Fujiwara, K. Yamazaki, H. Namatsu, K. Kurihara, et al., *Appl. Phys. Lett.* **76**, 637 (2000).
- [14] S. Tiwari, F. Rana, H. Hanafi, A. Hartstein, E. F. Crabbé, et al., *Appl. Phys. Lett.* **68**, 1377 (1996).
- [15] S. Miyazaki, K. Makihara, and M. Ikeda, *Thin Solid Films* **517**, 41 (2008).
- [16] T. SHIBAGUCHI, *IEICE Trans. Electron.* **E88-C**, 709 (2005).
- [17] S. Miyazaki, K. Makihara, and M. Ikeda, *Thin Solid Films* **518**, S30 (2010).
- [18] N. Morisawa, M. Ikeda, S. Nakanishi, A. Kawanami, K. Makihara, et al., *Jpn. J. Appl. Phys.* **49**, 04DJ04 (2010).
- [19] E. Leobandung, L. J. Guo, Y. Wang, and S. Y. Chou, *Appl. Phys. Lett.* **67**, 938 (1995).

- 
- [20] S. Fölsch, J. Martínez-Blanco, J. Yang, K. Kanisawa, and S. C. Erwin, *Nat. Nanotechnol.* **9**, 505 (2014).
- [21] D. Tsoukalas, P. Dimitrakis, S. Kolliopoulou, and P. Normand, *Mater. Sci. Eng. B Solid-State Mater. Adv. Technol.* **124-125**, 93 (2005).
- [22] Y. Pei, T. Kojima, and T. Hiraki, *Jpn. J. Appl. Phys.* **49**, 066503 (2010).
- [23] J. Dufourcq, S. Bodnar, G. Gay, D. Lafond, P. Mur, et al., *Appl. Phys. Lett.* **92**, 2006 (2008).
- [24] T. Hikono, T. Matsumura, A. Miura, Y. Uraoka, T. Fuyuki, et al., *Appl. Phys. Lett.* **88**, 23108 (2006).
- [25] C.-K. Yin, M. Murugesan, J.-C. Bea, M. Oogane, T. Fukushima, et al., *Jpn. J. Appl. Phys.* **46**, 2167 (2007).
- [26] T. Sakaguchi, Y.-G. Hong, M. Kobayashi, M. Takata, H. Choi, et al., *Jpn. J. Appl. Phys.* **43**, 2203 (2004).
- [27] C. K. Yin, T. Fukushima, T. Tanaka, M. Koyanagi, J. C. Bea, et al., *Appl. Phys. Lett.* **89**, (2006).
- [28] Z. Liu, C. Lee, V. Narayanan, G. Pei, and E. C. Kan, *IEEE Trans. Electron Devices* **49**, 1606 (2002).
- [29] R. J. Walters, G. I. Bourianoff, and H. A. Atwater, *Nat. Mater.* **4**, 143 (2005).
- [30] K. Makihara, H. Deki, M. Ikeda, and S. Miyazaki, *Jpn. J. Appl. Phys.* **51**, 04DG08 (2012).
- [31] S. Sun, *Science (80-. )*. **287**, 1989 (2000).
- [32] X. Sun, Y. Huang, and D. E. Nikles, *Int. J. Nanotechnol.* **1**, 328 (2004).
- [33] S. M. Park, C. H. Bae, W. Nam, S. C. Park, and J. S. Ha, *Appl. Phys. Lett.* **86**, 15 (2005).
- [34] A. J. Nozik, *Phys. E Low-Dimensional Syst. Nanostructures* **14**, 115 (2002).
- [35] M. Kroutvar, Y. Ducommun, D. Heiss, M. Bichler, D. Schuh, et al., *Nature* **432**, 81 (2004).
- [36] W. a. Hines, a. H. Menotti, J. I. Budnick, T. J. Burch, T. Litrenta, et al., *Phys. Rev. B* **13**, 4060 (1976).
- [37] K. Kobayashi, T. Sunohara, M. Umada, H. Yanagihara, E. Kita, et al., *Thin Solid Films* **508**, 78 (2006).
- [38] O. K. von Goldbeck, *IRON—Binary Phase Diagrams* (Springer Berlin Heidelberg, Berlin, Heidelberg, 1982).

- [39] M. C. Bost and J. E. Mahan, *J. Appl. Phys.* **58**, 2696 (1985).
- [40] C. Fu, M. Krijn, and S. Doniach, *Phys. Rev. B* **49**, 2219 (1994).
- [41] K. Hamaya, K. Ueda, Y. Kishi, Y. Ando, T. Sadoh, et al., *Appl. Phys. Lett.* **93**, 132117 (2008).
- [42] J. Tani, M. Takahashi, and H. Kido, *Phys. B-Condensed Matter* **405**, 2200 (2010).
- [43] A. Hjmsel and K. Kleinstuck, **541**, 541 (1980).
- [44] Y. Nakamura, Y. Nagadomi, S.-P. Cho, N. Tanaka, and M. Ichikawa, *Phys. Rev. B* **72**, 075404 (2005).
- [45] C. M. Sun, H. K. Tsang, S. P. Wong, W. Y. Cheung, N. Ke, et al., *Appl. Phys. Lett.* **92**, 211902 (2008).
- [46] D. Leong, M. Harry, K. J. Reeson, and K. P. Homewood, *Nature* **387**, 686 (1997).
- [47] T. Suemasu, Y. Negishi, K. Takakura, and F. Hasegawa, *Jpn. J. Appl. Phys.* **39**, L1013 (2000).
- [48] T. Suemasu, K. Takakura, C. Li, Y. Ozawa, Y. Kumagai, et al., *Thin Solid Films* **461**, 209 (2004).
- [49] M. Takauji, N. Seki, T. Suemasu, F. Hasegawa, and M. Ichida, *J. Appl. Phys.* **96**, 2561 (2004).
- [50] Y. Maeda, *Thin Solid Films* **515**, 8118 (2007).
- [51] M. Suzuno, T. Koizumi, and T. Suemasu, *Appl. Phys. Lett.* **94**, 213509 (2009).
- [52] Y. Maeda, K. Umezawa, Y. Hayashi, K. Miyake, and K. Ohashi, *Thin Solid Films* **381**, 256 (2001).
- [53] S. Izumi, M. Shaban, N. Promros, K. Nomoto, and T. Yoshitake, *Appl. Phys. Lett.* **102**, 032107 (2013).
- [54] Y. Ando, K. Ichiba, S. Yamada, E. Shikoh, T. Shinjo, et al., *Phys. Rev. B* **88**, 140406 (2013).
- [55] K. Sakai, T. Sonoda, S. Hirakawa, K. Takeda, and T. Yoshitake, *Jpn. J. Appl. Phys.* **51**, 028004 (2012).

## **Chapter 2**

### **Formation processes and characterization methods**

#### **2.1 Formation methods of metallic nanodots**

Metallic-nanodots (NDs) have been applied to advanced devices such as nonvolatile memories and ultrahigh density magnetic data medium to realize the next generation information technology compatible with Si processes [1–3]. In order to further improve the performance of such devices, a good uniformity in size and a high areal density are key factors. For instance, in the floating gate memory applications, the formation of NDs with an areal density as high as  $10^{11} \text{ cm}^{-2}$  is required.

The typical procedures for metal NDs formation include techniques such as magnetron sputtering [4], laser deposition [5, 6] and e-beam evaporation [7–12] to form a thin metal film on a thin layer of oxide, followed by annealing at elevated temperatures close to its eutectic temperature [13]. The deterioration of device characteristics due to the metal diffusion into the oxide is a concern in high-temperature processes. As an example of the floating gate memory, the metal diffusion into a gate dielectric layer due to high temperature often causes the degradation in the oxide reliability and variation in the memory window. Therefore, it is necessary to develop a low temperature formation method for ultrahigh density NDs, which enables to suppress

the diffusion of metal and to precisely control the dot size and density. Remote H<sub>2</sub> plasma (H<sub>2</sub>-RP) process is considered to meet such requirements. It was reported that pure metallic NDs, such as Pt, Ni and Pd, were formed on thermally-grown SiO<sub>2</sub> with an areal density as high as  $\sim 10^{11}$  cm<sup>-2</sup> by exposing ultrathin pure metal films to H<sub>2</sub>-RP without any external heating [14–16]. Based on this method, we extend our research to the formation of binary alloy Fe-silicide NDs. H<sub>2</sub>-RP process is also promising for the formation of Fe-silicide NDs.

In this chapter, the formation method of metallic-NDs on SiO<sub>2</sub> by using H<sub>2</sub>-RP, and the physics behind the methodologies will be introduced.

## 2.2 Remote H<sub>2</sub> plasma induced formation of metallic nanodots on SiO<sub>2</sub>

The schematic view of remote H<sub>2</sub> plasma (H<sub>2</sub>-RP) treatment equipment used in this work is shown in Fig. 2.1. The H<sub>2</sub> gas was introduced from the top of a quartz tube with a diameter of 10 cm and the plasma was generated in the quartz tube by inductive coupling with an external single-turn antenna connected to power generator through a matching circuit. We employed a 60 MHz very high frequency (VHF) power generator, rather than a conventional radio-frequency (RF) power source (13.6 MHz) in the experiment because 60 MHz-VHF plasma has higher plasma density and lower electron temperature compared with those of conventional 13.6 MHz-RF plasma [17]. The substrate was placed on a susceptor at a distance of 23 cm away from the position

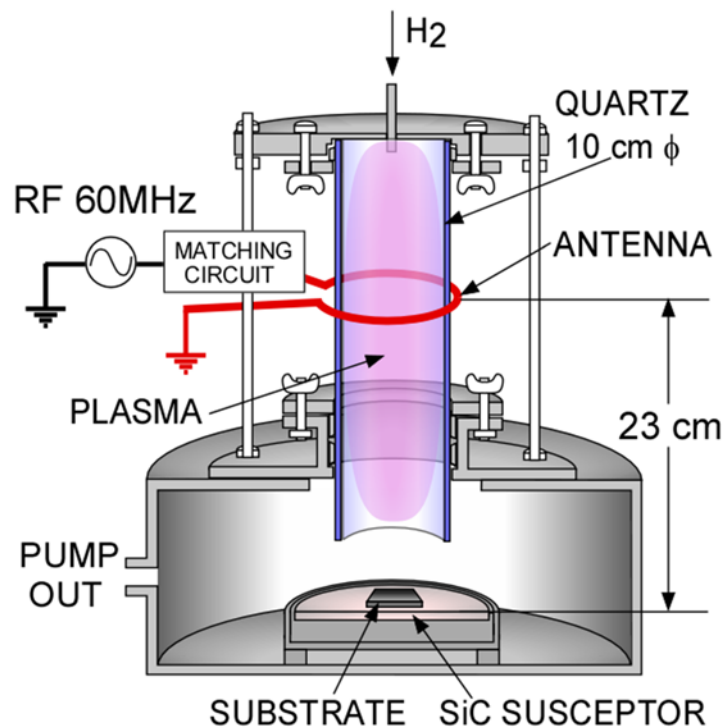


**Fig. 2.1.** Schematic view of remote H<sub>2</sub> plasma treatment equipment.

of the antenna. In the glow discharge of H<sub>2</sub> gas, there existed ionized species, electrons, monatomic (free-radical) hydrogen and vacuum-ultraviolet (VUV) photons. In particular, some damaging effects, namely, charged particle bombardment and VUV irradiation, arise from direct interaction of the plasma and the substrate [18, 19]. The ion bombardment and VUV irradiation can easily be suppressed from sample surface by keeping a sufficient distance between the antenna and sample in contrast to the direct plasma immersion [18]. Thereby, only homogeneous activated hydrogen radicals can reach to the surface of sample [18]. Based on such designs, referred to as the remote plasma, damaging effects can be avoided. Taking into account these beneficial features of the remote hydrogen plasma, we have employed this technique for the metal-NDs formation.

Here we explain the typical procedure for the formation of metallic NDs on SiO<sub>2</sub> induced by the H<sub>2</sub>-RP treatment. After conventional wet-chemical cleaning steps of Si wafers, a thin SiO<sub>2</sub> layer was grown at 1000 °C. A few nanometer-thick metal films are first deposited uniformly on the SiO<sub>2</sub> by sputtering or electron beam evaporation. Subsequently, the films so-prepared were simply exposed to H<sub>2</sub>-RP without external heating. As just representative results, Figure 2.2 shows changes in the surface morphologies of Pt and Al layers due to the H<sub>2</sub>-RP treatment, which was evaluated by AFM. AFM images for the as-deposited metal films on SiO<sub>2</sub> showed a fairly smooth surface morphology with a root-mean-square (RMS) roughness as small as ~0.18 nm, being almost identical to that for the as-grown SiO<sub>2</sub> surface. These results confirm uniform surface coverage with the ultrathin metal films. After the H<sub>2</sub>-RP exposure,

the formation of metallic NDs with an areal density over  $10^{11}$  cm<sup>-2</sup> is clearly observed for the case of Pt [Fig. 2.2 (b')]. This result can be explained that, during the H<sub>2</sub>-RP exposure, the local heating caused by the surface recombination of atomic hydrogen on the metal surface promotes the surface migration and agglomeration of metal atoms for minimizing surface free energy [13–16]. In contrast, for the case of the Al film [Fig. 2.2 (c), (c')], there is no change in surface morphologies before and after H<sub>2</sub>-RP exposure. The result can be interpreted in terms of native oxide on the Al film surface, which prevents adsorption and recombination of atomic hydrogen on Al surface.

To confirm the influence of atomic hydrogen exposure on surface temperature of metal films, the raise in the surface temperature during remote plasma exposure was investigated by using thermocouple covered with these metal foils as shown in Fig. 2.3. The thermocouple covered with an Al foil with native oxide showed a surface temperature as low as ~50°C during H<sub>2</sub> exposure, while over 300 °C for Pt, under the same conditions.

Therefore, we have to take into account the tendency of metals to be oxidized for the formation of metal NDs induced by the H<sub>2</sub>-RP exposure. Figure 2.4 shows the standard reduction potentials of metallic elements summarized from chemical thermodynamic data [20], which imply most easily oxidized metals have negative values in standard reduction potential. Thus, Al and Fe are easily oxidized at room temperature in comparison to Pt, Ni and Pd.

Therefore, the formation of NDs from easily oxidizable metal layers such as Fe is still a challenge.

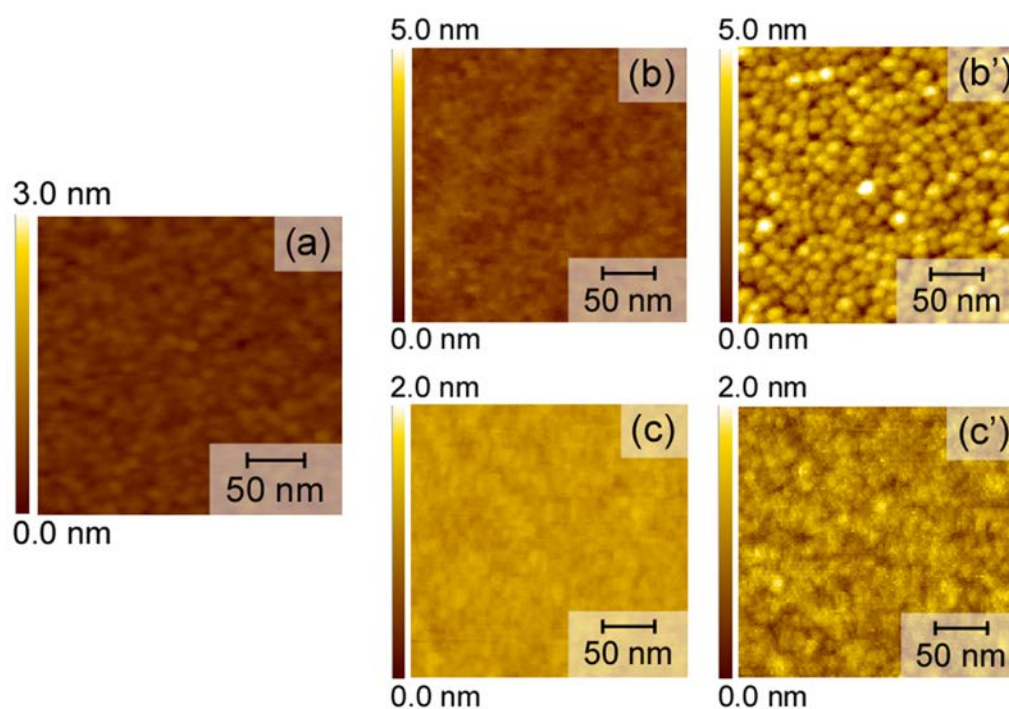


**Fig. 2.2.** AFM images of (a) as-grown SiO<sub>2</sub>, (b) ultrathin Pt and (c) Al films deposited on SiO<sub>2</sub> and (b') (c') their surfaces after exposing to H<sub>2</sub>-RP at VHF power of 350 W. H<sub>2</sub> pressure and substrate temperature were maintained at 0.26 Torr and room temperature, respectively.

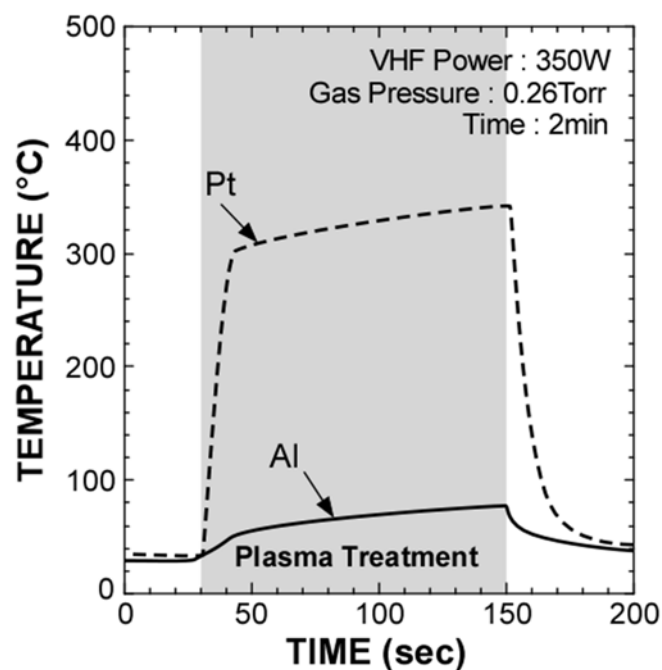


Fig. 2.3. Temperature change of metal foils during H<sub>2</sub>-RP exposure, in which a thermocouple was covered with the metal foils.

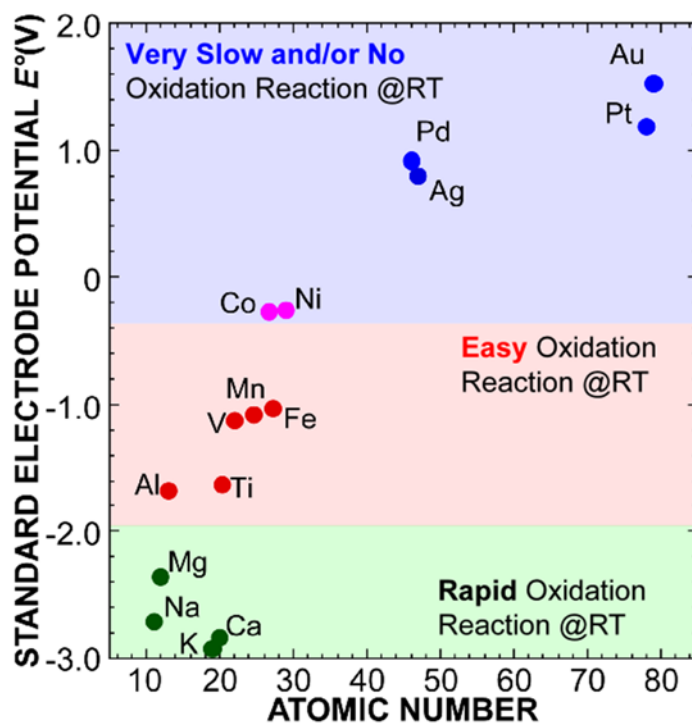


Fig. 2.4. Standard reduction potentials of metallic elements.

## 2.3 Characterization methods

In this section, characterization methods of structural and physical properties of NDs will be introduced.

### 2.3.1 Atomic Force Microscope (AFM)

Atomic force microscopy (AFM) is a technique to obtain surface morphology images and other information from a wide variety of samples, at extremely high (nanometer) resolution [21, 22]. As shown in Figure 2.5(a), atomic force (or other physical interaction) acting between the probe tip and the sample surface is measured from the displacement of the cantilever. AFM works by scanning a very sharp (end radius ca. 10 nm) probe along the sample surface, carefully maintaining the force between the probe and surface. Figure 2.5(b) shows the schematic view of AFM setup, in which the vertical deflection of the cantilever due to forces acting on the tip is detected by a laser focused on the back side of the cantilever. The laser is reflected by the cantilever into a photo diode detector. The movement of the laser spot on the detector gives a

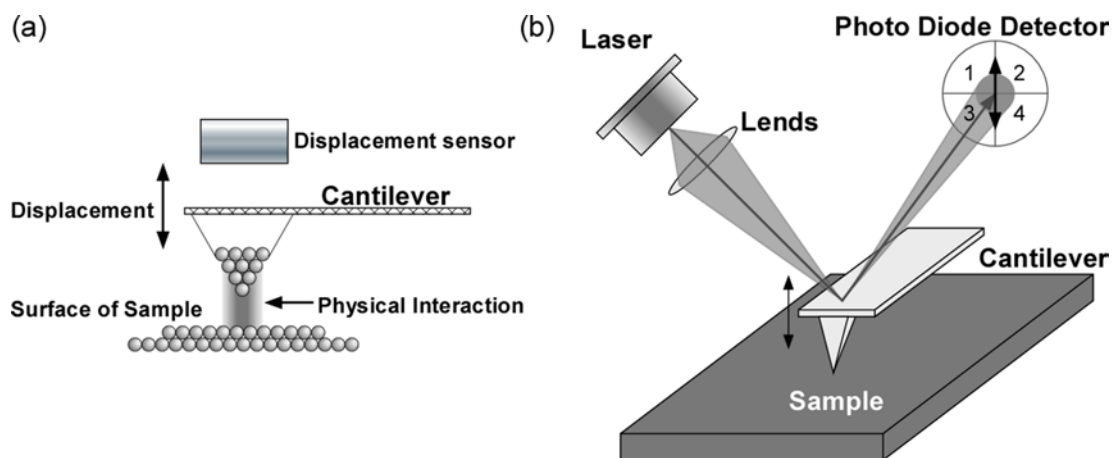


Fig. 2.5. The principle and schematic view of an AFM [25].

greatly exaggerated measurement of the movement of the probe. In the simplest mode, the probe gently touches the sample as it moves over the surface. The movement of the probe over the surface is controlled by a scanner in the x, y, and z axes. The signal from the photodetector passes through a feedback circuit, and into the z-movement part of the scanner, in order to maintain the probe-sample distance at a set value. Because the cantilever acts as a spring [21], this fixed cantilever deflection means that a fixed probe-sample force is maintained. The amount by which the scanner has to move in the z axis to maintain the cantilever deflection is taken to be equivalent to the sample topography. A great advantage of AFM, compared to TEM and SEM, is that it is simple to operate in almost any environment, such as aqueous solutions, but also other solvents, in air, vacuum, or other gases [15]. Depending on the details of the experiment, the resolution can be very high. Resolution of z (height) is extremely high and can be sub-angstrom, whereas lateral resolution could be of the order of 1 nm.

There are a variety of modes of scanning, the most commonly used operation modes of an AFM are:

- Contact mode AFM (AFM/Contact Mode)
- Tapping mode AFM (AFM/Tapping Mode)
- Non-contact mode (AFM/Non-Contact Mode).

Apart from the topographic modes that collect images, there are many modes designed to measure other properties of the sample. For example:

- ◆ Kelvin Force Microscopy (KFM)
- ◆ Magnetic Force Microscopy (MFM)

**a) AFM/Contact Mode**

The most common imaging mode is the contact mode. In this case, the AFM tip is brought in contact with the sample surface by keeping constant force, and set to scan the sample in an x-y direction. A feedback keeps a predetermined deflection of the cantilever at a constant value with respect to the sample surface by adjusting the z scanner for each x-y coordinate. This change ( $\Delta Z$ ) in z axis corresponds with the

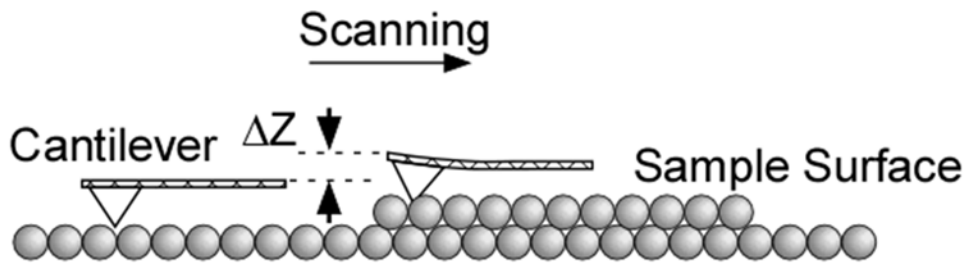


**Fig. 2.6.** A schematic view of AFM/Contact Mode [25].

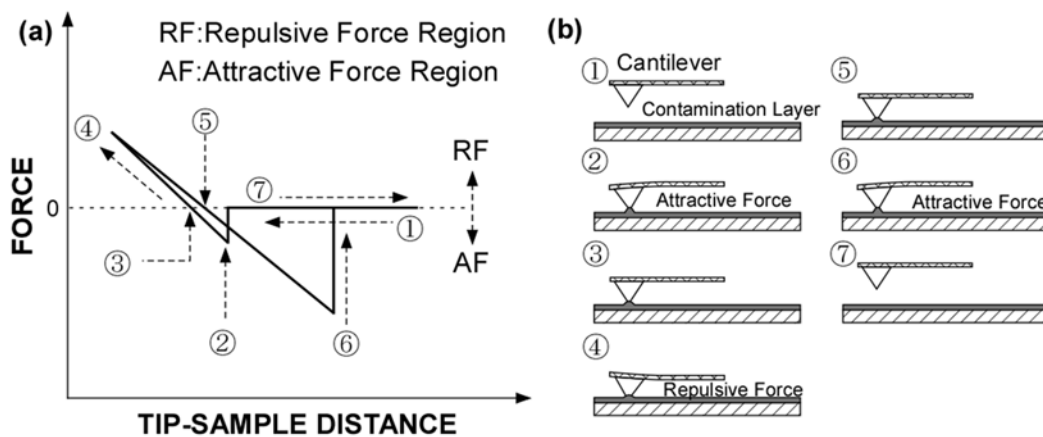


**Fig. 2.7.** The relationship between (a) the force acting on the probe and distance of tip-sample and (b) schematic view of a contact state of the tip and the sample [25].

topographical height at the sample at each measured point. By adjusting the predetermined force accordingly, the image varied in contrast can be obtained and the damage to the sample can be minimized.

Figure 2.7(a) shows a typical characteristic curve (force curve) of the force acting on the cantilever with respect to the distance between sample and tip. Figure 2.7 (b) shows a schematic view of a contact state of the tip and the sample at each point marked in ①~⑦ in Figure 2.7 (a). As shown in Figure 2.7 (b), due to the presence of adsorbed water layer on the sample surface in the air, when the probe is in contact with or detached from the sample, an interaction between the probe and the adsorbed water layer will occur. If the probe tip and the surface of the sample are sufficiently distant, because only weak forces to the cantilever, distinct deformation of cantilever does not appear ①. As the probe tip approaches to the sample surface enough, strong attractive force acts between the sample surface and the cantilever, the cantilever is in contact with the sample surface ②. As the probe tip approaches to the sample surface continually, simultaneously with the attractive force, the repulsive force begins acting and gradually becomes stronger, the cantilever becomes horizontal at equilibrium when the magnitude of the attractive and repulsive forces are balanced equally ③. As the cantilever approaches even closer to the surface, repulsive force will increase and cause the cantilever to deflect away from the sample surface ④. When the probe tip draw back from the sample surface, the force between the tip and sample gradually decreases, the cantilever become horizontal at equilibrium once again when the magnitudes of the attractive and repulsive forces are balanced equally ⑤. And if adhesions occurred

between the probe and sample surface; the force causes the cantilever to bend downward ⑥. When all adhesions are broken, the cantilever returns to the original position ⑦.

### **b) AFM/Tapping Mode**

For very soft materials, contact mode might not be suitable due to the friction between AFM tip and the sample surface. In tapping mode, the cantilever vibrates at its resonant frequency (bounces up and down) by applying an external electrical excitation. While scanning the sample in x-y directions, the AFM tip briefly strikes against the sample surface at each oscillation cycle, causing a decrease in the oscillation amplitude. Similar to the constant force in contact mode, the feedback maintains a constant decrease in oscillation amplitude by moving the piezoelectric element, and a height image can be detected.

### **c) Kelvin Force Microscopy (KFM)**

KFM (surface potential microscope / Kelvin force microscope) [23] is one of the measurement modes in scanning probe microscopy (SPM). It's possible to image the value of the surface potential which doesn't appear in the surface morphology image and observe a surface morphology image and a surface potential image, simultaneously. Figure 2.8 shows the principle diagram of KFM mode measurement. In KFM measurement mode, by applying an AC and DC voltage ( $V_{DC} + V_{AC} \sin \omega t$ ) between the conductive cantilever and the sample, the surface potential will be detected by the response of the cantilever vibration by electrostatic force while measuring the surface by DFM. Here, the output signal from the cantilever is separated into two frequency

components by the lock-in amplifier. The applied frequency components of the AC voltage (1:  $\omega$  component) is used for the surface potential measurement. On the other hand, DFM operating frequency component (2:  $\omega_r$  component) is used for surface morphology measurement. The  $\omega$  component of amplitude ( $A_\omega$ ) is represented by the following formula:

$$A_\omega = -S \frac{dC}{dZ} V_{DC} V_{AC} = -S \frac{dC}{dZ} (V_{off} + V_s) V_{AC} \quad (2.1)$$

where C is electrostatic capacitance between the tip and sample, and S is the correction constant determined by the device and  $V_s$  is the surface potential of a sample.

As the  $A_\omega$  becomes zero, if the  $V_s$  is compensated by the offset voltage  $V_{off}$ , surface potential  $V_s$  of the sample can be determined by  $V_s = -V_{off}$  (always control  $V_{off}$  to keep  $A_\omega = 0$ ).

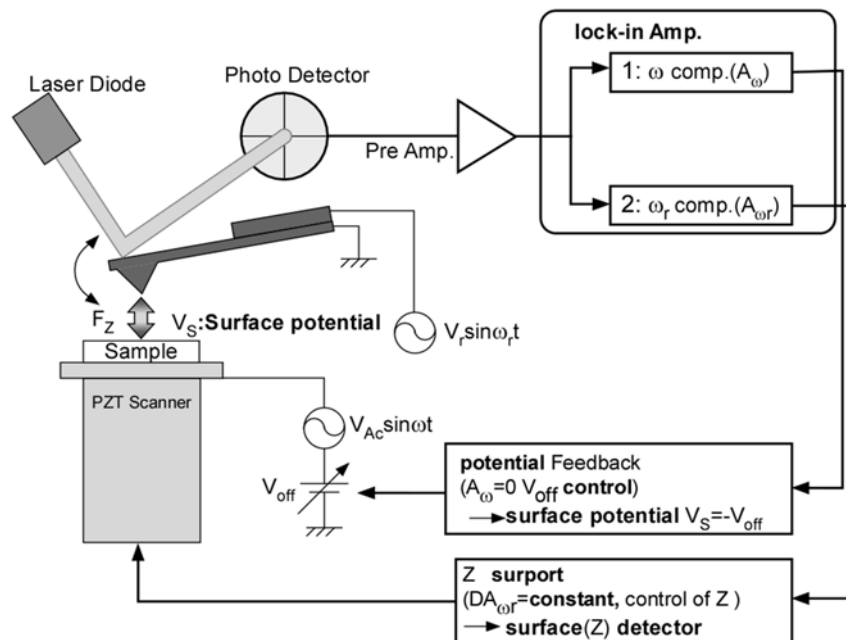


**Fig. 2.8.** Schematic diagram of KFM system [35, 36].

#### d) Magnetic Force Microscopy (MFM)

MFM (magnetic force microscope) detects the phase shift of the cantilever vibration due to the magnetic interaction between the magnetic probe and the magnetic field of the sample surface to obtain the distribution of the magnetic force gradient (magnetic force image). In fact, the MFM probe is a cantilever probe made of silicon that is coated with a magnetic film (CoPtCr) with a thickness of 10~100 nm by sputtering film deposition, that is then magnetized and made into the MFM probe [24]. The MFM image is obtained by detecting the attraction or repulsion magnetic force acting between the probe and the sample. If attractive and repulsive forces act between the probe and the sample, the phase is delayed and advance, respectively, this is reflected in the contrast of the MFM image [21, 24, 25]. In MFM measurement, the sample is scanned twice to characterize the signals. In the first scan, the tip scans the surface in AFM/tapping mode to obtain the topography of the sample. In the second scan (lift mode), the tip-sample distance is increased and the tip is scanned along the topography

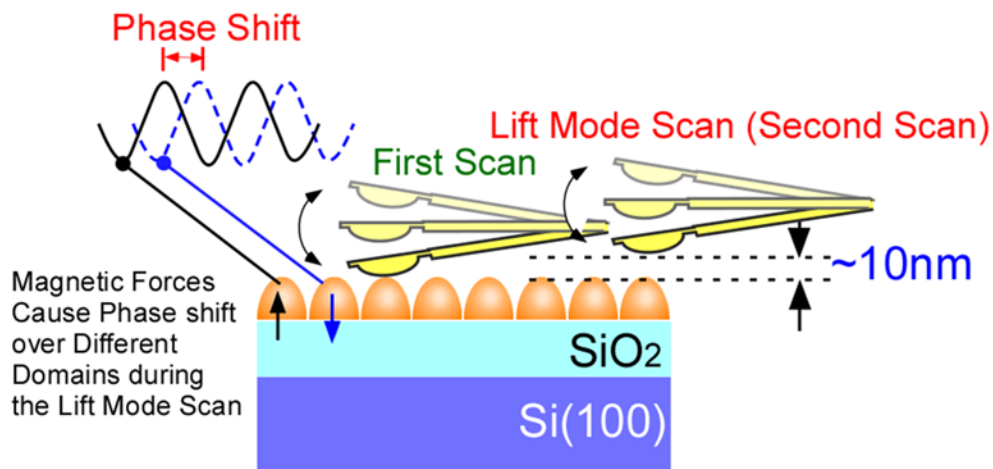


Fig. 2.9. Schematic diagram of MFM system.

line obtained from the first scan, as illustrated schematically in Fig. 2.9.

In practical measurements, if the tip is close to the surface, where standard non-contact AFM is operated, the image will be predominantly topographic. With increasing the distance between the tip and the sample, magnetic effects become apparent. In this work, we set tip height at about 10 nm.

### 2.3.2 Alternating Gradient-field Magnetometer (AGM)

The AGM (Alternating Gradient-Field Magnetometer, also called AGFM) was used to measure the magnetic moments ( $M$ ) of the magnetic thin films. The AGM uses a set of AC gradient field coils that produce an alternating field. The alternating field generates a force  $F_x$  to apply to the sample that causes the sample to vibrate and the amplitude of this vibration is relative to the magnetic moment of the sample [26]. The

Force  $F_x$  is given by:

$$F_x = M \frac{\partial H_x}{\partial X} \quad (2.2)$$

The schematic diagram of AGM is shown in Fig. 2.10. The sample is set on the probe of a cantilevered rod that connects to a piezoelectric element. The sample is magnetized by a DC field and a small alternating field gradient is applied simultaneously to

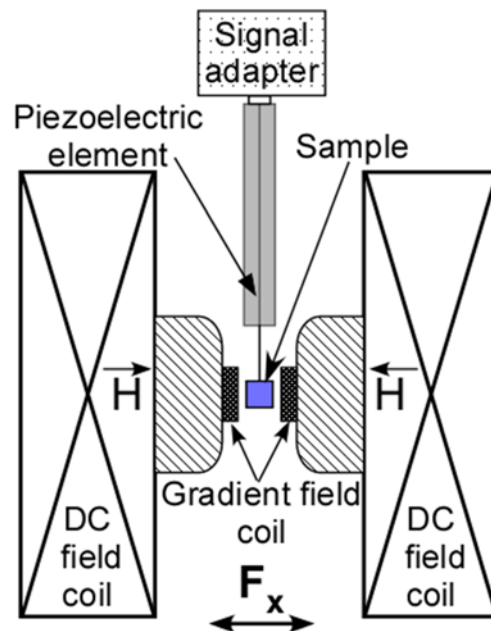


**Fig. 2.10.** Schematic diagram of alternating gradient-field magnetometer.

the sample. The top end of the cantilevered rod is attached to the piezoelectric element. The actual sensor in the system is a displacement sensor or a force sensor, usually a piezoelectric element [26]. The output from the piezoelectric element is synchronously detected at the frequency of the gradient field [26]. The amplitude of this voltage is proportional to the magnetic moment of the sample, which can be varied by changing the applied DC magnetic field  $H_{\text{ext}}$ . To enhance the signal to noise ratio (SNR), the sample is vibrated at a frequency close to the resonance frequency of the sample cantilever. The gradient field varies in orders smaller than the coercive fields of the investigated sample and is applied by the small coil placed in the greater field coils providing the magnetic bias field. The maximum field of the AGM used in this research is 22 kOe and the measurement frequency is from 100 to 1000 Hz. The sensitivity of this system reaches to  $10^{-8}$  emu.

### **2.3.3 X-ray Photoelectron Spectroscopy (XPS)**

X-ray photoelectron spectroscopy (XPS) is one of the most widely used in technology of surface analysis. Figure 2.11 shows XPS basic principle and schematic diagram of photoelectron emission processes in solids [27]. A solid surface to be analyzed is incident with soft X-ray photons. When a photon with an energy  $h\nu$  interacts with an electron in a level with binding energy  $E_B$ , the entire photon energy is transferred to the electron, with the result that a photoelectron is ejected with kinetic energy  $E_k$  [27]:

$$E_k = h\nu - E_B - q\phi_s \quad (2.3)$$

Where,  $\Phi_s$  is difference in work function between spectrometer and sample.

$h\nu$  is the X-ray photon energy which must be greater than  $E_B$ . The ejected electron may originate from a core level or from the occupied portion of the valence band. Because no two elements have the same set of electronic energy levels, XPS enables elemental analysis by measurement of the photoelectron kinetic energies. In addition, Equation 2.3 indicates that any changes in  $E_B$  are reflected in  $E_k$ . So that the changes in the chemical states of an atom can be followed by inspecting changes in the photoelectron energies, referred to as chemical shift, leading to the provision of chemical information [27–30].

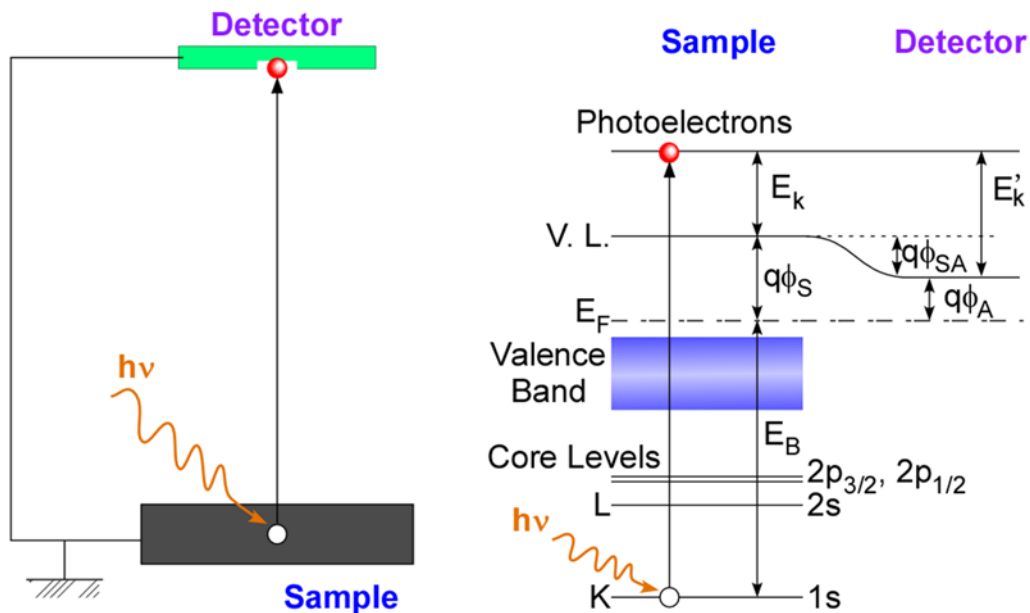


**Fig. 2.11.** XPS basic principle and schematic diagram of photoelectron emission processes in solids.

Since the mean free path of the electrons is very small, only the electrons that are generated in a few nanometer-thick layers of the surface can reach the detector. Hence XPS is thought as a surface sensitive technique. The most commonly used X-ray sources are Mg K $\alpha$ , Al K $\alpha$ , and monochromatized Al K $\alpha$ .

### **Chemical Shifts and Spectral Information [27,29–32]**

For typical XPS investigation, a wide scan or survey XPS spectrum (low resolution) is usually obtained first, especially if chemical compound of the sample is unknown. Once the elements are identified from the survey spectrum, detailed (high resolution) scans of selected elements of interest are performed for chemical state identification and quantitative analysis. In this work, wide scan range is ordinarily from 1400 to 0 eV in binding energy which is sufficient for the identification of detectable elements. In a wide scan several peaks are observed in the spectra but the most intense peaks are photoelectron lines. Other peaks often observed are: Auger lines, valence band lines and so on which are not discussed here.

Chemical shift is the change in a photoelectron peak energy from a particular element when the chemical state of that element changes [27]. When an atom bonded with another atom or group of atoms, the change in the valence electron density happens. According to whether valence electron is attracted or distracted, the change in the valence electron density will become positive or negative. This causes a consequent variation in the electrostatic potential affecting the core electron levels. Therefore, the binding energies of the core electrons change, giving rise (according to Eq. 2.3 ) to

shifts in the corresponding photoelectron peaks [27].

### **Quantitative Analysis [29–31]**

In practice, the peak areas for the elements are converted into fractional atomic concentrations using the relative atomic sensitivity factors as shown in the following Equation:

$$C_a = \frac{I_a/S_a}{\sum_n I_n/S_n} \quad (2.4)$$

Where  $C_a$  is the fractional atomic concentration of element a, I is the peak intensity, S is the relative atomic sensitivity factor, and the sum is performed over all elements detected in the sample. Because of the fairly crude assumptions, the concentrations measured using this approach are probably associated with an error of about 10%. Values of  $S_n$  may be calculated from theory or derived empirically by recording spectra from standard materials. XPS instruments are generally provided with the atomic sensitivity factors and appropriate algorithms as a part of a software package for calculating the concentrations.

#### **2.3.4 Raman Scattering Spectroscopy**

One of the important tools that we utilize in our research is Raman scattering spectroscopy [33]. A simple explanation is introduced to understand the process of Raman scattering. When light of a wavelength is irradiated to materials, then this light will interact with molecules of the material. It may be reflected, absorbed or scattered in several different ways. Figure 2.12 shows the process of light scattering.

In general, when the light is scattered by molecules [34], most of scattered light have the same frequency with incident light as shown in Fig. 2.12 (a), which is called Rayleigh scattering. However, the incoming light may lose some part of its energy to the material (or gain some energy from the material) during the process of scattering. According to the vibration of the molecules of the materials, the scattering with a decrease in frequency is called the Stokes scattering [Fig. 2.12 (b)]. On the contrary, the scattering with an increase in frequency is called the Anti-Stokes scattering [Fig.2.12 (c)]. Raman scattering are the changes in the frequency (wavelength) of the light. The change in wavelength of the scattered photon provides the chemical and structural information. Raman shifted photons of light can be either of higher or lower energy, depending on the vibrational states of the materials. Raman spectroscopy has become a primary analytical and research tool. It can be used for applications in wide

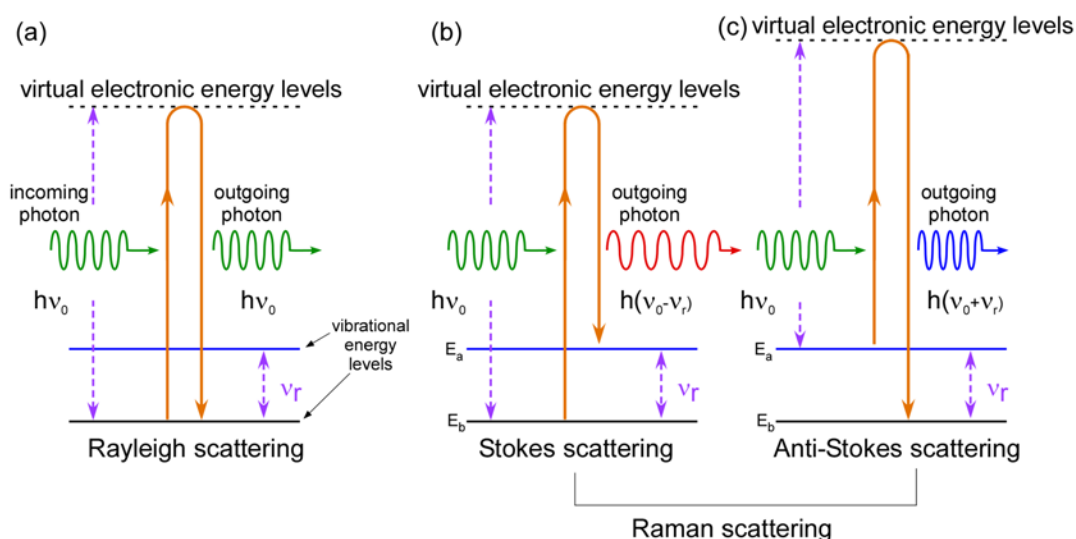


**Fig. 2.12.** The process of light scattering.

range of pharmaceuticals, polymers, thin films, and semiconductors. We can determine unknown materials from their unique Raman spectral features by using databases of known spectra.

### 2.3.5 X-ray Diffraction (XRD)

X-ray diffraction (XRD) is one of the primary techniques in materials characterization often used to determine the crystalline phases and crystalline structures [35]. When an x-ray beam hits an atom, the electrons around the atom start to oscillate with the same frequency as the incoming beam [36].

As shown in figure 2.13 [31], an x-ray beam incident on a pair of parallel planes P1

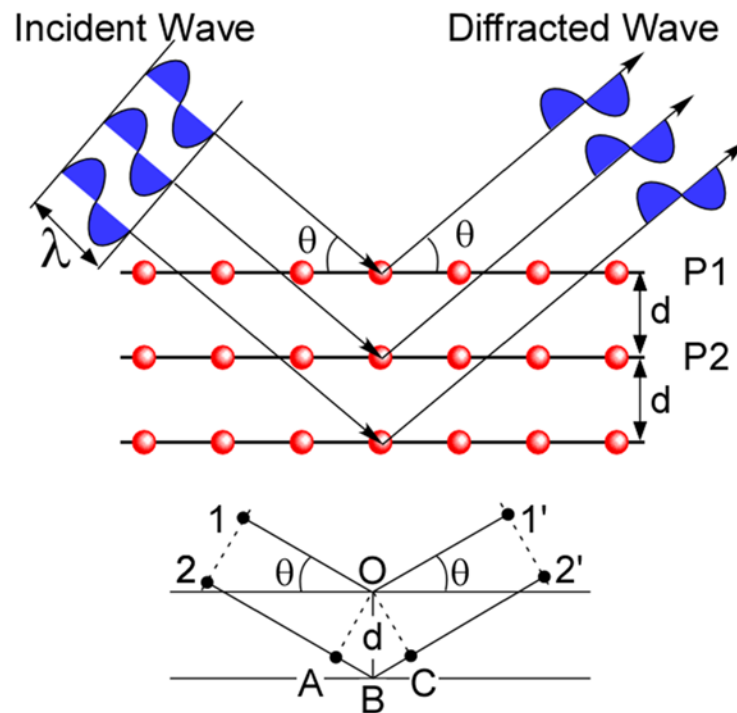


**Fig. 2.13.** Visualization of the Bragg equation. Maximum scattered intensity is only observed when the phase shifts add to a multiple of the incident wavelength  $\lambda$ .

and P2, separated by a lattice spacing ( $d$ ). The two parallel X-rays 1 and 2 are incident to these planes in an angle ( $\theta$ ). A reflected beam of maximum intensity will result if the waves represented by 1' and 2' are in phase [36]. The difference in path length between 1 to 1' and 2 to 2' must then be an integral number of wavelengths. This relationship can be mathematically expressed in Bragg's law as shown in Fig. 2.13:

$$2d \sin \theta = n\lambda \quad (2.5)$$

The process of reflection is shown here by incident and diffracted X-rays, each making an angle  $\theta$  with a fixed crystal plane. Diffraction occurs from planes set at angle  $\theta$  with respect to the incident beam and generates a diffracted beam at an angle  $2\theta$  from the incident beam. The possible  $d$ -spacing defined by the indices  $h, k, l$  are determined by the shape of the unit cell. That is to say, the material with specific crystal structure has a set of corresponding diffraction peaks. The material is determined by the diffraction angle  $2\theta$  and the intensity of the diffraction peak.

## References

- [1] Y. Pei, T. Kojima, and T. Hiraki, *Jpn. J. Appl. Phys.* **49**, 066503 (2010).
- [2] J. Dufourcq, S. Bodnar, G. Gay, D. Lafond, P. Mur, et al., *Appl. Phys. Lett.* **92**, 2006 (2008).
- [3] T. Hikono, T. Matsumura, A. Miura, Y. Uraoka, T. Fuyuki, et al., *Appl. Phys. Lett.* **88**, 23108 (2006).
- [4] J. Dufourcq, P. Mur, M. J. Gordon, S. Minoret, R. Coppard, et al., *Mater. Sci. Eng. C* **27**, 1496 (2007).
- [5] X. Sun, Y. Huang, and D. E. Nikles, *Int. J. Nanotechnol.* **1**, 328 (2004).
- [6] Z. Gai, B. Wu, J. P. Pierce, G. A. Farnan, D. Shu, et al., *Phys. Rev. Lett.* **89**, 235502 (2002).
- [7] A. ShklyaeV and M. Ichikawa, *Phys. Rev. B* **65**, (2001).
- [8] T. Ichitsubo, S. Tojo, T. Uchihara, E. Matsubara, A. Fujita, et al., *Phys. Rev. B* **77**, 094114 (2008).
- [9] Z. Abdullaeva, E. Omurzak, C. Iwamoto, H. Ihara, H. S. Ganapathy, et al., *Jpn. J. Appl. Phys.* **52**, 01AJ01 (2013).
- [10] J. D. McBrayer, *J. Electrochem. Soc.* **133**, 1242 (1986).
- [11] D. Tsoukalas, P. Dimitrakis, S. Kolliopoulou, and P. Normand, *Mater. Sci. Eng. B Solid-State Mater. Adv. Technol.* **124-125**, 93 (2005).
- [12] H. Hosoya, M. Arita, K. Hamada, and Y. Takahashi, *Mater. Sci. Eng. C-Biomimetic Supramol. Syst.* **26**, 1146 (2006).
- [13] Z. Liu, C. Lee, V. Narayanan, G. Pei, and E. C. Kan, *IEEE Trans. Electron Devices* **49**, 1606 (2002).
- [14] K. ShimanoE, K. Makihara, and M. Ikeda, **2**, 616 (2009).
- [15] K. Makihara, K. ShimanoE, A. Kawanami, M. Ikeda, S. Higashi, et al., *J. Optoelectron. Adv. Mater.* **12**, 626 (2010).
- [16] K. Makihara, K. ShimanoE, M. Ikeda, S. Higashi, and S. Miyazaki, *Jpn. J. Appl.*

- Phys. **47**, 3099 (2008).
- [17] A. S. H. Eet, P. Set, and E. N. Park, in *16th Int. Symp. Plasma Chem. Proc. ISPC-16* (2003), pp. 1–5.
- [18] A. M. Wrobel, S. Wickramanayaka, Y. Nakanishi, Y. Fukuda, and Y. Hatanaka, *Chem. Mater.* **7**, 1403 (1995).
- [19] N. M. Johnson, J. Walker, C. M. Doland, K. Winer, and R. A. Street, *Appl. Phys. Lett.* **54**, 1872 (1989).
- [20] D. D. Wagman, W. H. Evans, V. B. Parker, R. H. Schumm, I. Halow, et al., in *J. Phys. Chem. Ref. Data* (1982), pp. 1–407.
- [21] P. Eaton and P. West, *Atomic Force Microscopy* (Oxford University Press, 2010).
- [22] G. Friedbacher, in *Surf. Thin Film Anal.* (Wiley-VCH Verlag GmbH & Co. KGaA, 2011), pp. 443–464.
- [23] M. Nonnenmacher, M. P. O’Boyle, and H. K. Wickramasinghe, *Appl. Phys. Lett.* **58**, 2921 (1991).
- [24] エスアイアイ・ナノテクノロジー株式会社, *MFМ測定ガイド Ver.2a* (2008).
- [25] 森田清三, *走査プローブ顕微鏡* (丸善, 2000).
- [26] R. A. de Groot, F. M. Mueller, P. G. van Engen, and K. H. J. Buschow, *Phys. Rev. Lett.* **50**, 2024 (1983).
- [27] H. Bubert, J. C. Rivière, and W. S. M. Werner, *X-Ray Photoelectron Spectroscopy (XPS)* (Wiley-VCH Verlag GmbH & Co. KGaA, Weinheim, Germany, 2011).
- [28] J. C. Rivière and H. Bubert, in *Surf. Thin Film Anal.* (Wiley-VCH Verlag GmbH & Co. KGaA, Weinheim, Germany, 2011), pp. 1–5.
- [29] S. Oswald, *X-Ray Photoelectron Spectroscopy in Analysis of Surfaces* (2006).
- [30] K. M. Pamidimukkala, in *Encycl. Anal. Chem.* (John Wiley & Sons, Ltd, Chichester, UK, 2006), pp. 1–17.
- [31] J. F. Watts and J. Wolstenholme, in *An Introd. to Surf. Anal. by XPS AES* (2005), pp. 17–58.
- [32] T. Yamashita and P. Hayes, *Appl. Surf. Sci.* **254**, 2441 (2008).

- [33] E. Poliani, M. R. Wagner, J. S. Reparaz, M. Mandl, M. Strassburg, et al., *Nano Lett.* **13**, 3205 (2013).
- [34] K. Kneipp, Y. Wang, H. Kneipp, I. Itzkan, R. R. Dasari, et al., *Phys. Rev. Lett.* **76**, 2444 (1996).
- [35] R. D. Tarey, R. S. Rastogi, and K. L. Chopra, *Rigaku J.* **4**, 11 (1987).
- [36] H. Stanjek and W. Häusler, *Hyperfine Interact.* **154**, 107 (2004).
- [37] 科学機器事業部セイコーインスツルメンツ株式会社, *金属酸化物のKFM観察* (2002).

## **Chapter 3**

### **Formation of Fe nanodots on SiO<sub>2</sub> induced by remote H<sub>2</sub> plasma**

In this chapter, firstly, influences of chemical bonding features and changes in the surface morphologies of ultrathin Fe films formed on thermally-grown SiO<sub>2</sub> exposed to H<sub>2</sub>-RP were discussed in preparation for the formation of Fe-silicide-NDs. After that, to get insight into the formation of NDs on SiO<sub>2</sub>, impacts of VHF power, gas pressure, initial Fe-film thickness and H<sub>2</sub>-RP exposure time on areal dot density were investigated. Finally, electrical and magnetic properties of Fe-NDs so-prepared were also characterized by using AFM/Kelvin force microscopy and AGM, respectively.

### **3.1 Introduction**

Considering about compatibility with Si-ULSI technologies, Fe-based binary alloy-NDs such as Fe-silicide [1–3] and/or germanide NDs [4–6] have been extensively studied because these NDs lead us to the development of novel functional devices such as a ferromagnetic resonance tunneling device [1], spin-dependent single electron transistor [2] and nanodot floating gate memory [3–7].

As the first step to fabricate Fe-silicide NDs, we focused on the Fe-NDs formation on SiO<sub>2</sub> from an electron-beam-evaporated Fe film. In this chapter, a role of hydrogen radicals on the Fe-NDs formation was studied. In particular, effects of VHF power, gas pressure, exposure time, and initial film thickness on areal dot density were discussed.

### **3.2 Experimental details**

A ~5.0-nm-thick SiO<sub>2</sub> layer was thermally grown on p- or n-type Si (100) substrate and treated with a dilute HF solution to terminate the surface with OH bonds. 1.0~15.0 nm-thick Fe films were deposited on the SiO<sub>2</sub> layer by the electron beam evaporation without any extra heating. Subsequently, these Fe films were exposed to the remote plasma of pure H<sub>2</sub>. The plasma was generated in a quartz tube with a diameter of 10 cm by the inductive coupling with an external single-turn antenna connected to a 60 MHz power generator through a matching circuit. The substrate was placed on a susceptor at a distance of 23 cm from the antenna to minimize ion damages. For the H<sub>2</sub>-RP exposure, the gas pressure and very high frequency (VHF) power were changed in the range of 9.0 to 39.9 Pa and 300 to 500 W, respectively. The exposure time during the H<sub>2</sub>-RP exposure was varied in the range from 45 seconds to 22 min. Areal dot density and size uniformity were evaluated by atomic force microscopy (AFM). To evaluate the electrical isolation of the NDs so-prepared, topographic images and their corresponding surface potential images were simultaneously taken with a noncontact Kelvin-probe force microscopy (KFM) mode using an Rh-coated Si cantilever before and after the electron charging to NDs [14, 15, 18]. XPS measurements under monochromatized Al K $\alpha$  (1486.6 eV) radiation were used to investigate the influence of the H<sub>2</sub>-RP exposure on the chemical bonding features in Fe/SiO<sub>2</sub>/Si(100) structures and the work function of the resultant Fe-NDs.

### 3.3 Results and discussion

#### 3.3.1 Impact of remote H<sub>2</sub> plasma exposure on Fe atom migration on SiO<sub>2</sub>

AFM images of as-evaporated 3-nm-thick Fe film show a fairly smooth surface with a root-mean-square roughness of 0.24 nm and they are almost identical to those of the as-grown SiO<sub>2</sub> surface, as shown in Figs. 3.1(a) and (b). After H<sub>2</sub>-RP exposure to Fe film under a gas pressure of 26.6 Pa at a VHF power of 500W, we can clearly see the formation of Fe-NDs with an areal dot density of  $\sim 2.4 \times 10^{11} \text{ cm}^{-2}$  [Fig. 3.1(c)] and an average height of  $\sim 4.2 \text{ nm}$  determined by fitting the measured size distribution to a log-normal function, as represented in Fig. 3.2.

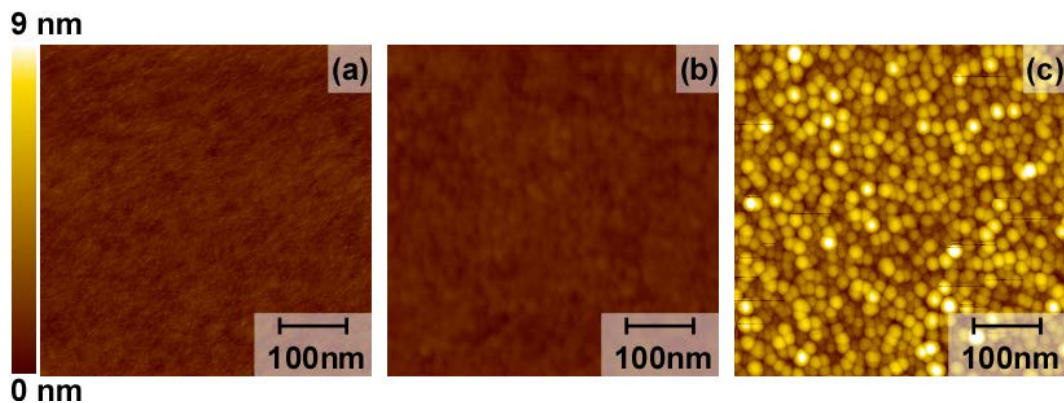


**Fig. 3.1.** AFM topographic images of (a) as-grown SiO<sub>2</sub>, a 3-nm-thick Fe layer deposited on SiO<sub>2</sub> (b) before and (c) after H<sub>2</sub>-RP exposure at VHF power of 500W. The H<sub>2</sub> gas pressure and substrate temperature were maintained at 26.6 Pa and RT, respectively. The exposure time was kept constant at 10 min.

To confirm the electrical isolation among the Fe-NDs so-prepared, changes in the surface potential due to electron charging to NDs were examined as shown in Fig. 3.3. In this experiment, after scanning the sample surface with an electrically-biased AFM tip in a tapping mode, topographic and surface potential images were taken simultaneously by Kelvin-probe force microscopy (KFM). When the surface was scanned with an AFM tip biased at -6.0 V with respect to the substrate in a tapping mode, a distinct surface potential decrease ( $\sim 28\text{mV}$ ) [Fig. 3.3(b)] due to electron injection into the each dot was observed. The distribution of this surface potential along the line AB was very well fitted by a Gaussian function [Fig. 3.3 (c)]. However, in the unbiased area, no change in the surface potential was detectable [Fig. 3.3(a)].

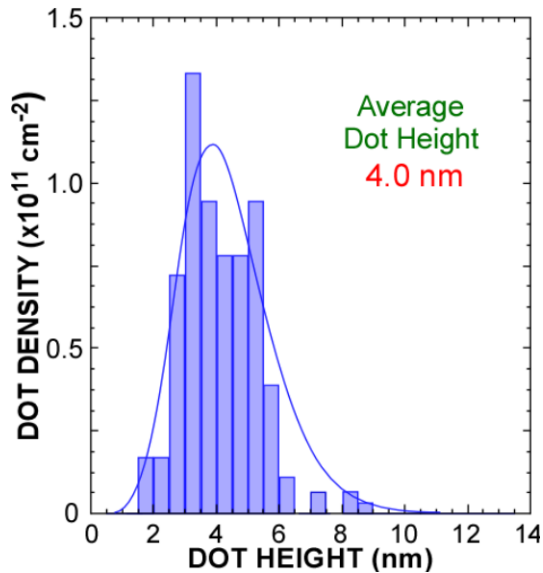


**Fig. 3.2.** Distribution of dot height obtained from AFM images corresponding to Fig. 3.1(c). The solid line denotes the log-normal function well fitted to the measured distribution.

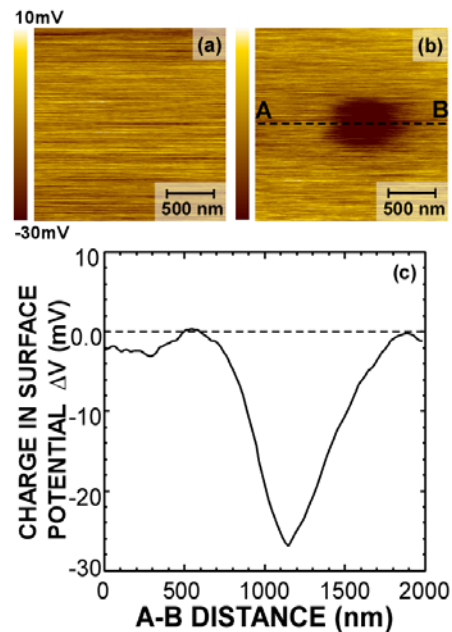


**Fig. 3.3.** Surface potential images measured in a Kelvin probe mode (a) before and (b) after electron injection at a tip bias of -6.0 V and (c) one dimensional potential profile along line A–B.

Additionally, in surface potential images some horizontal lines were observed due to measurement noise. We confirmed that by rotating the sample by angles of 90°. This result indicates that Fe-NDs were electrically isolated from one to another. For the sample just after the Fe film formation prior to the H<sub>2</sub>-RP exposure, no changes in surface potential were observed on images taken before and after applying any biases because of the electrically conductive surface.

XPS measurements were taken to evaluate the influence of the H<sub>2</sub>-RP exposure on the chemical bonding features of Fe film/SiO<sub>2</sub>. Figures 3.4 (a) and (b) show the Fe 2p<sub>3/2</sub> and Si 2p core-line spectra measured for a ~3.6 nm-thick Fe film on SiO<sub>2</sub>/Si(100) before and after the H<sub>2</sub>-RP exposure for 10 min. The chemically shifted Fe 2p<sub>3/2</sub> signals in the higher binding energy side from the metallic Fe component (706.8 eV) are

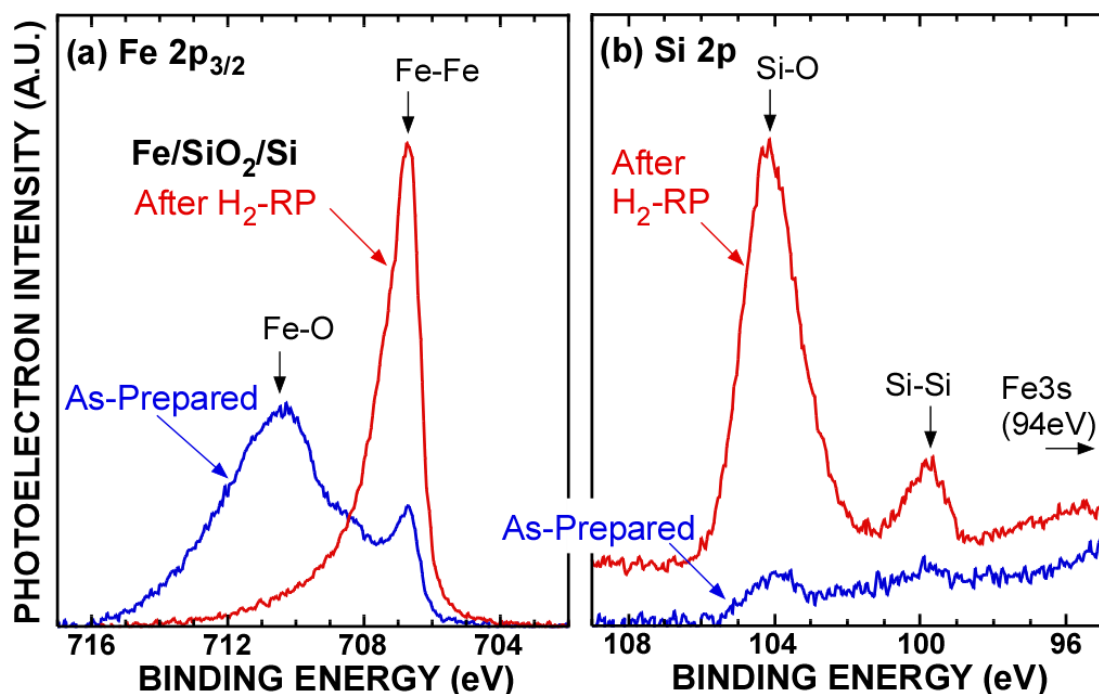


**Fig. 3.4.** (a) Fe 2p<sub>3/2</sub> and (b) Si 2p core-line spectra taken for ~3.6-nm-thick Fe film on SiO<sub>2</sub>/Si(100) before and after H<sub>2</sub>-RP exposure for 10 min. The photoelectron take-off angle in each spectrum was set at 90°.

clearly observed in the Fe 2p<sub>3/2</sub> spectrum for the sample before the H<sub>2</sub>-RP exposure. Taking into account of the fact that the Fe-oxide components exhibit within the 710.9 and 709.6 eV in the binding energy scale [19], such Fe oxides are thought to be formed on the sample surface in the air exposure during the sample transfer to the chamber for H<sub>2</sub>-RP exposure. Note that metallic Fe signals are markedly increased with a decrease in the Fe oxide component after H<sub>2</sub>-RP exposure, which indicates that a reduction reaction in the surface Fe oxide proceeds during H<sub>2</sub>-RP exposure. These result in that a pure Fe surface was produced. The H atoms were adsorbed on the pure Fe surface. Therefore, the migration of Fe atoms is driven by local heating caused by the efficient recombination of atomic hydrogen on pure Fe surface as a result of the formation of Fe-NDs. In addition, the Si 2p signals originating from the Si-O and Si-Si bonding units are significant due to the H<sub>2</sub>-RP exposure. This can be interpreted as revealing the underlying SiO<sub>2</sub>/Si substrate from among the Fe-NDs when taking the AFM analyses results into consideration, as shown in Fig. 3.1. Similar results in core-line signals are obtained from the analyses of the valence band spectra, as shown in Fig. 3.5. A sharp peak due to the valence band top of metallic Fe derived from the Fe 3d state at 0.8 eV in the binding energy scale appears after the H<sub>2</sub>-RP exposure, which indicates that the Fe-NDs have a high density of states in the region near the Fermi level as well as the element Fe.

Furthermore, the work function value of Fe-NDs was quantified from the cut-off energy for the photoemissions in the lower limit of the kinetic energy scale, as shown in Fig. 3.6. When taking into account the thermal broadening in the electron occupation near the Fermi level, the photoemission threshold energy corresponding to the work function can be determined by fitting the measured photoemission spectra near the low kinetic energy side to a Fowler function [20]. The validity of this method was

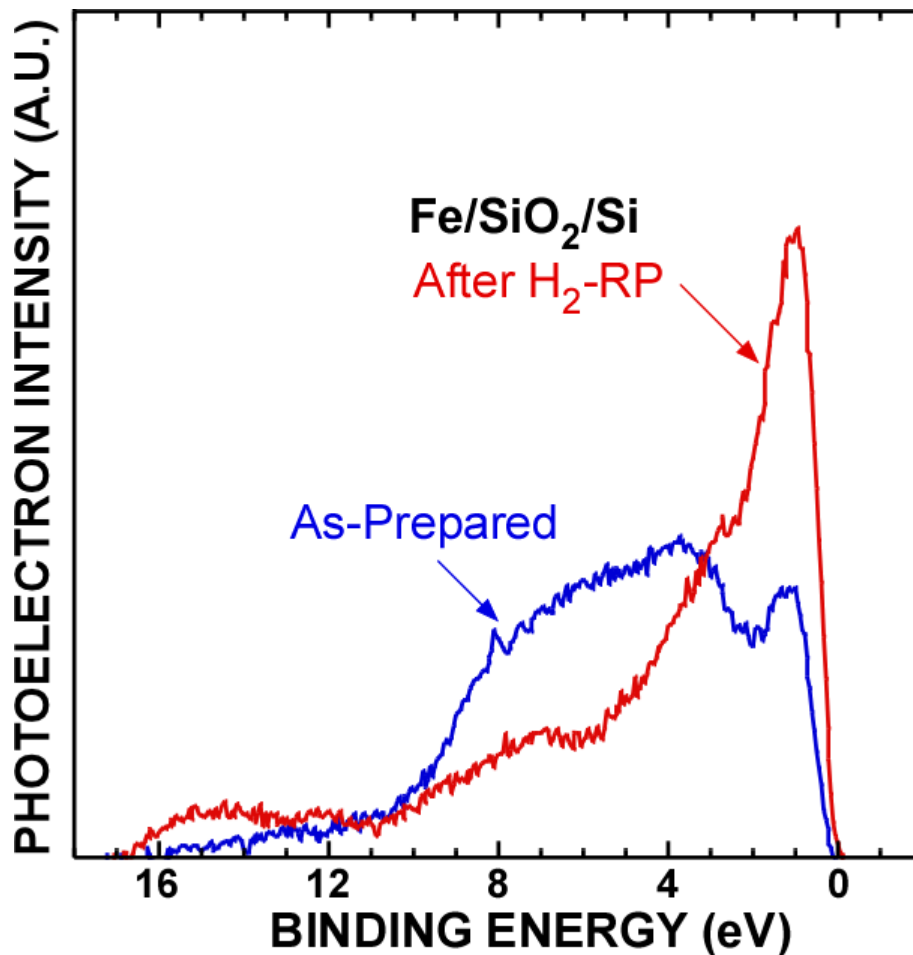


**Fig. 3.5.** Valence band spectra taken for samples before and after H<sub>2</sub>-RP exposure shown in Fig.3.4.

confirmed from the work function values measured for element metals such as Au, Ag, and Ni [21]. The work function value of Fe-NDs was determined to be  $4.48 \text{ eV} \pm 0.05 \text{ eV}$ , which is almost identical to the vacuum work function of pure Fe [22, 23].

To get an insight into the surface migration of Fe atoms enhanced by H<sub>2</sub>-RP exposure, a raise in the surface temperature was monitored during H<sub>2</sub>-RP exposure by using thermocouple covered with a Fe foil, as shown in Fig. 3.7. By exposing the Fe foil to remote plasma of pure H<sub>2</sub>, the surface temperature was sharply increased up to  $\sim 500 \text{ }^\circ\text{C}$ .

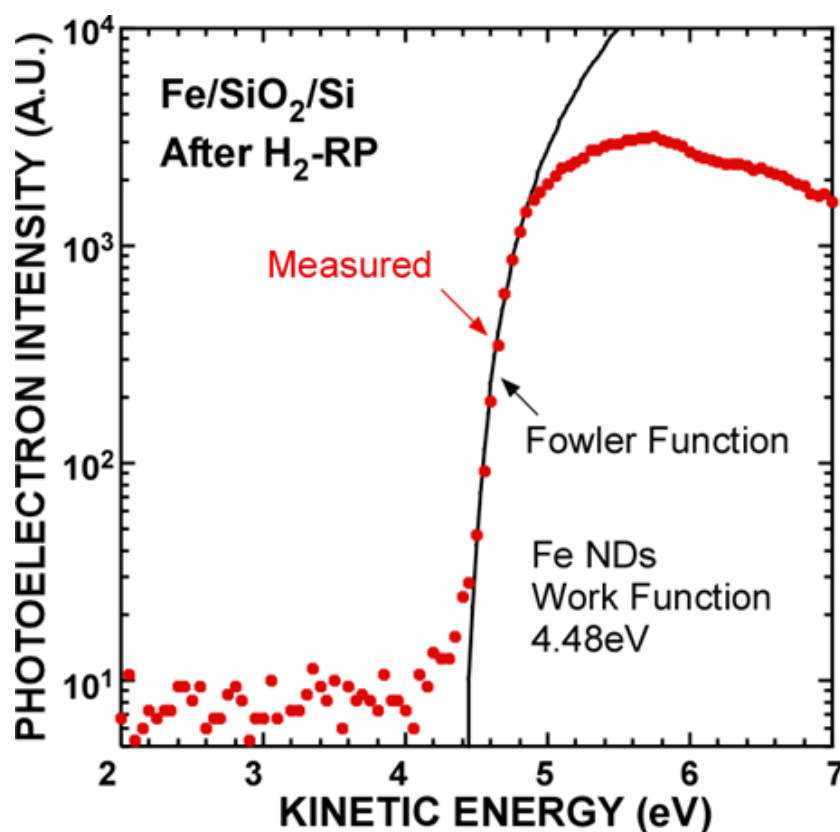


**Fig. 3.6.** Photoelectron yield spectra for Fe film deposited on SiO<sub>2</sub> after H<sub>2</sub>-RP exposure near photoemission threshold in kinetic energy scale.

The cutoff energy extraction by fitting the Fowler function to the measured spectra lines yields the work function of Fe-NDs.

This result indicates that the formation of the NDs is attributed to the surface migration and agglomeration of Fe atoms driven by the local heating caused by the efficient recombination of atomic hydrogen on pure Fe surface.

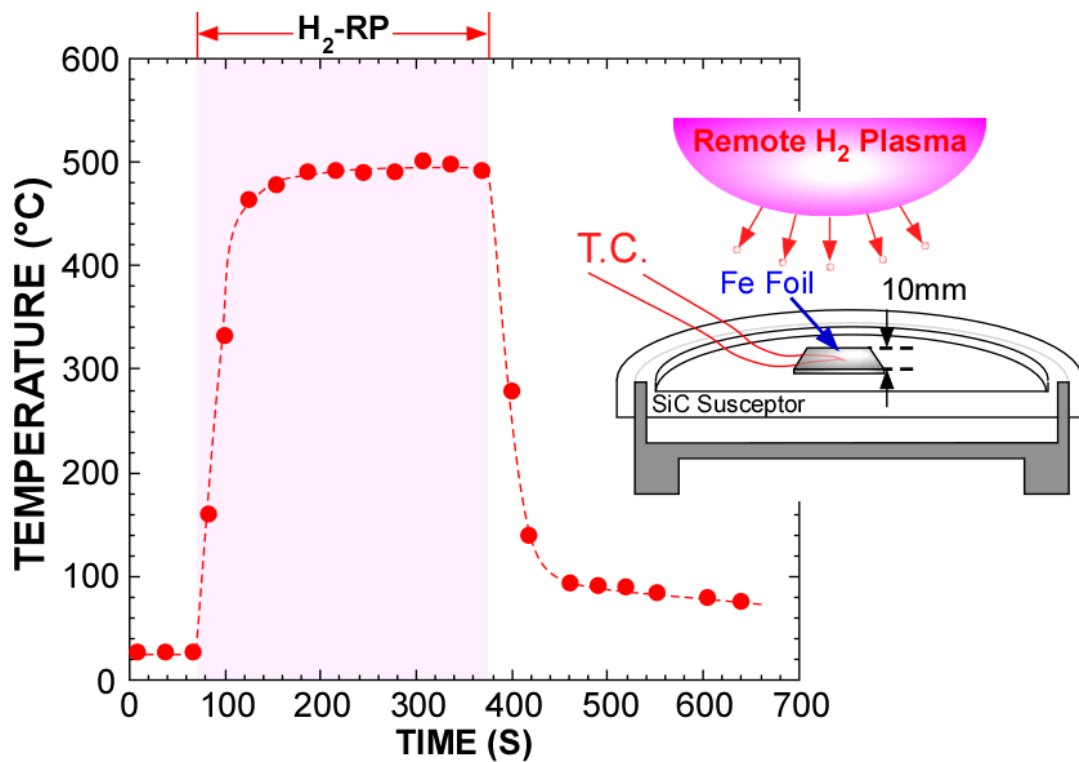


**Fig. 3.7.** Surface temperature change of Fe foil during H<sub>2</sub>-RP exposure. A setup of thermocouple connected with the Fe foil is shown in the inset. The H<sub>2</sub> gas pressure and VHF power were maintained at 26.6 Pa and 500 W, respectively.

We also evaluated the effect of VHF power and pressure on NDs density and maximum temperature as summarized in Figs. 3.8 and 3.9, respectively. As shown in Fig. 3.8, with increasing VHF power, both the dot density and the surface temperature were increased. The result is interpreted in terms of an increase in the flux of atomic hydrogen incident to the surface. On the other hand, H<sub>2</sub> pressure dependence is not

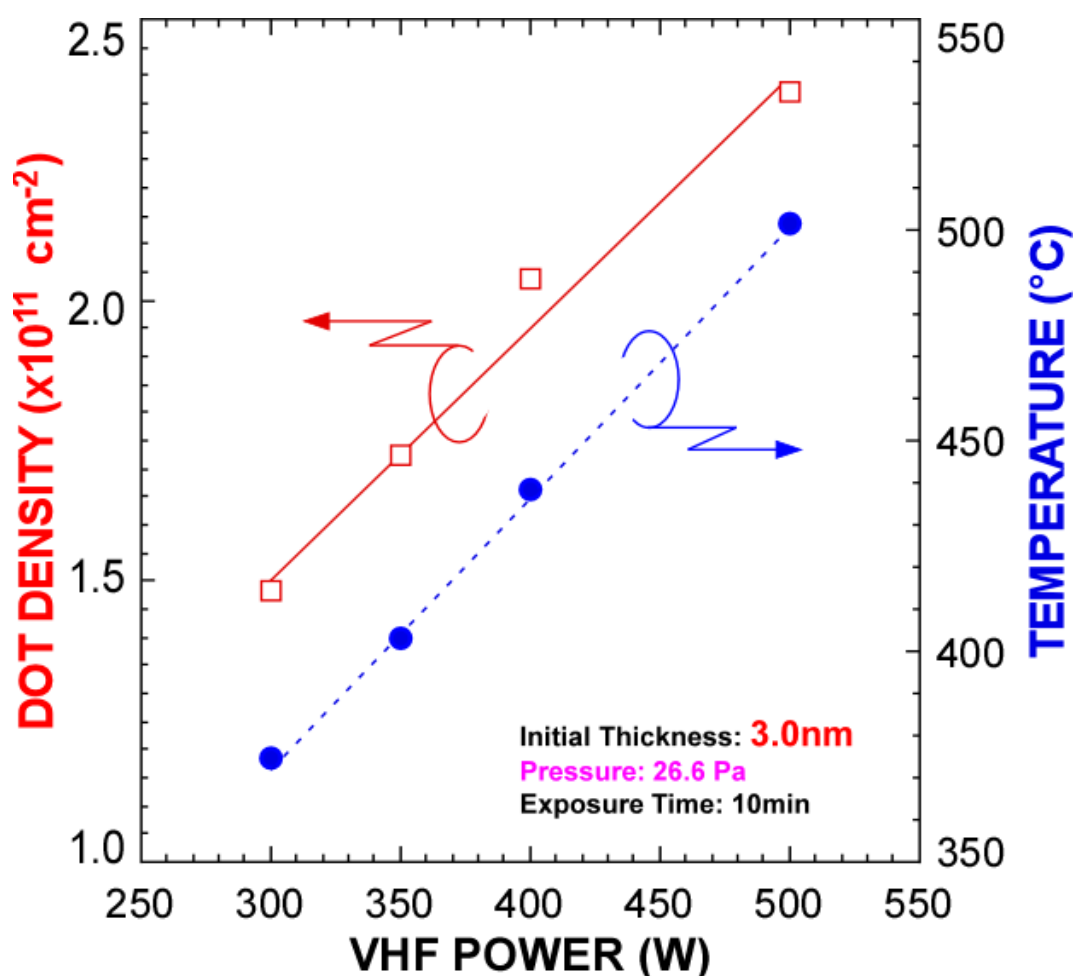


**Fig. 3.8.** Areal density of Fe-NDs formed by H<sub>2</sub>-RP exposure without external heating and the maximum temperature of Fe foil surface as functions of VHF power. The H<sub>2</sub> gas pressure during H<sub>2</sub>-RP exposure was maintained at 26.6 Pa.

such simple as shown in Fig. 3.9. With an increase in the H<sub>2</sub> pressures from 9.0 to ~27 Pa, the dot density was markedly increased but a further increase in the H<sub>2</sub> pressure up to ~40 Pa caused a slight decrease in the dot density. It is likely that, at pressures below ~27 Pa, as the pressure is higher, the atomic hydrogen flux to the surface becomes larger. Under pressures higher than 27 Pa, the diffusion loss of atomic

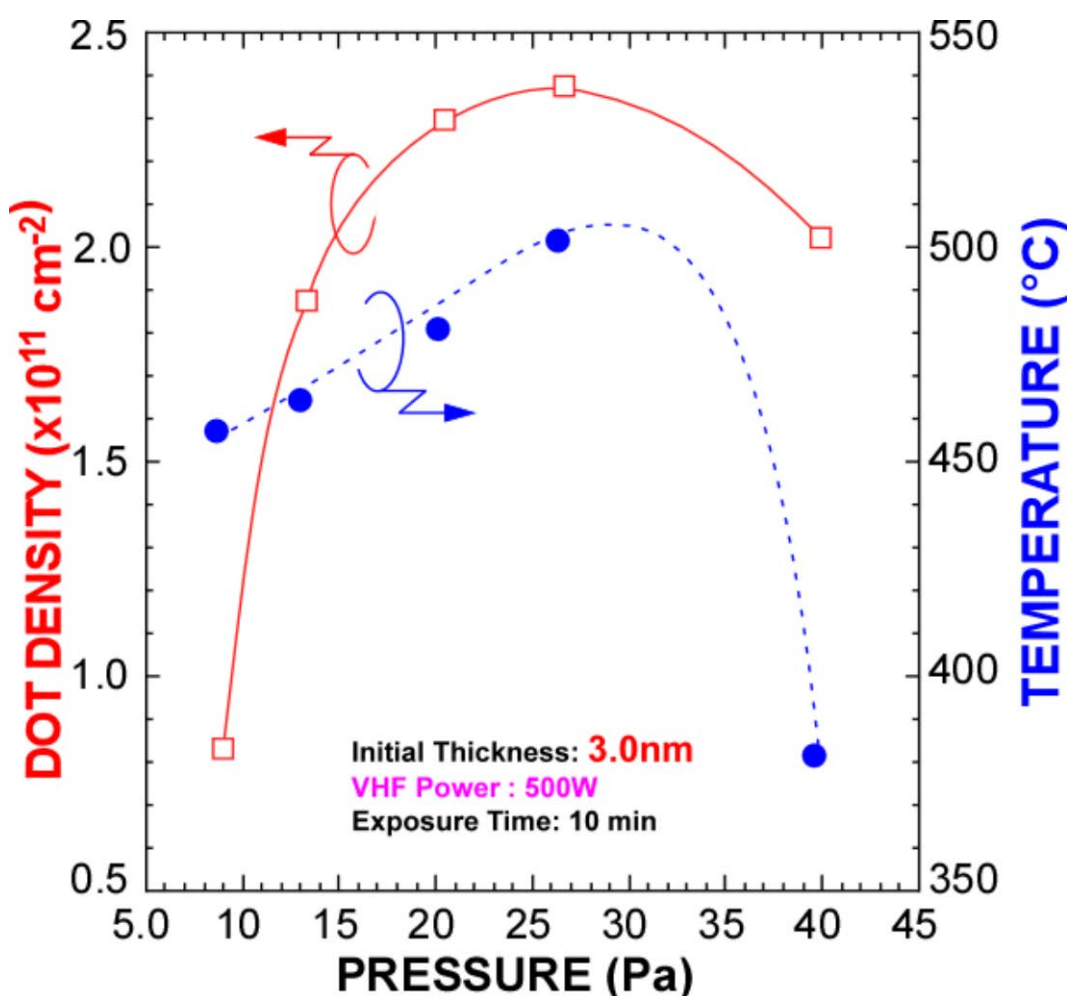


**Fig. 3.9** Areal density of Fe-NDs formed by H<sub>2</sub>-RP exposure without external heating and the maximum temperature of Fe foil surface as functions of H<sub>2</sub> gas pressure. The VHF power during H<sub>2</sub>-RP exposure was maintained at 500 W.

hydrogen before reaching the sample surface becomes significant due to the increased number of collisions in the gas phase. In fact, the maximum surface temperature rose from 450 to 550 °C with pressure increasing from 9.0 to ~27 Pa and then decreased down to 380 °C at 40 Pa.

The initial film thickness dependence on the area density and average dot height of

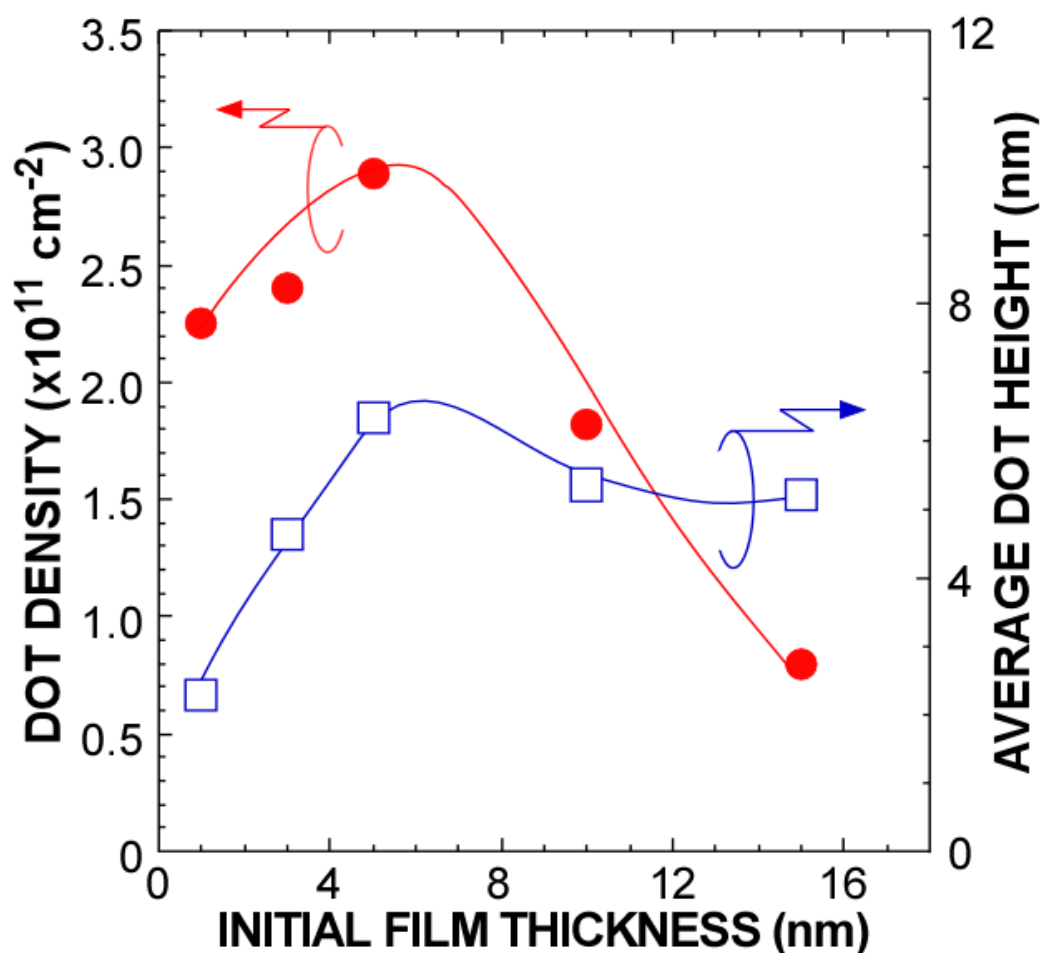


**Fig. 3.10.** Initial film thickness dependence on the area density and average dot height of Fe-NDs formed by H<sub>2</sub>-RP exposure for 10 min. The VHF power and H<sub>2</sub> gas pressure during H<sub>2</sub>-RP exposure were maintained at 500 W and 26.6 Pa, respectively.

Fe-NDs formed by H<sub>2</sub>-RP exposure was also investigated as shown in Fig. 3.10. The Fe films with a thickness from ~1.0 to ~15 nm were exposed to H<sub>2</sub>-RP, where exposure time was kept constant at 10 min. The dot density is considerably increased from  $2.3 \times 10^{11}$  to  $\sim 3.0 \times 10^{11} \text{ cm}^{-2}$  and the average dot high is also increased from ~2.2 to ~6.4 nm by increasing the initial film thickness from ~1.0 to ~5.0 nm. On the other hand, when further increasing the film thickness to over ~5.0 nm, the areal dot density significantly decreased down from  $\sim 3.0 \times 10^{11}$  to  $8 \times 10^{10} \text{ cm}^{-2}$ . While the average dot heights showed a slight decrease in the case of the film thickness of 10 nm, and there was no change for the film thickness between 10 and 15 nm.

Figs. 3.11 show the topographic images of initial film thickness of 5 nm 15 nm after

H<sub>2</sub>-RP exposure, respectively.

Compared with an evident dot

formation in the case of

5-nm-thick initial film, for the

thick film (15 nm), a dots-like

surface morphology was

observed due to the insufficient

surface migration of Fe atoms.

Furthermore, from the surface

potential measurements using

noncontact KFM, the electrical

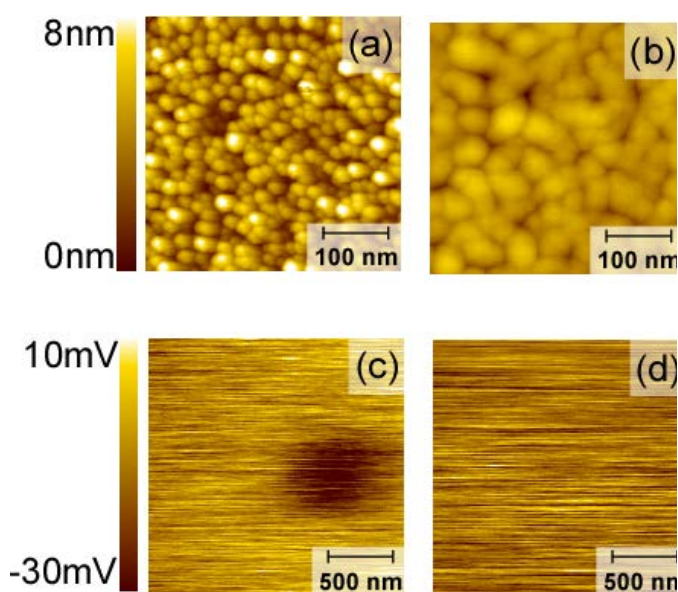


**Fig. 3.11.** Topographic images of initial film thicknesses of (a) 5 nm and (b) 15 nm after H<sub>2</sub>-RP exposure and (c, d) corresponding surface potential images measured in a Kelvin probe mode after electron injection at a tip bias of -5.0 V.

isolation among the Fe-NDs is also confirmed in the cases of the initial Fe-film thickness as below ~5.0 nm as shown in Fig. 3.11 (c). In contrast, for thicker cases (~10.0 and ~15.0 nm), an electrically-connective surface was proven to exist as a result of insufficient surface migration of the Fe atoms for thicker cases (~15nm), as shown in the Fig. 3.11 (d), as a result of insufficient surface migration of Fe atoms. The results indicate that the control of the initial Fe-film thickness to as thin as ~5.0 nm or below is a key point to achieve the high density formation of electrically isolated Fe-NDs.

We also evaluated the impact of the H<sub>2</sub>-RP exposure time on the areal dot density for ~1.0 and ~3.0 nm-thick initial Fe films, as shown in Fig. 3.12. The density of the Fe-NDs is decreased by approximately a quarter with an increase in the exposure time from 45 s to 22 min for ~3.0 nm-thick Fe films. This result indicates that in the case of ~3.0 nm-thick Fe films, the coalescence of the initially-formed Fe-NDs was facilitated to form large dots with increasing H<sub>2</sub>-RP exposure time. It is interestingly noted that, almost no change in the dot density is detectable with the H<sub>2</sub>-RP exposure under the same conditions in the case of ~1.0 nm-thick Fe films although the average dot height increases with an increase in the H<sub>2</sub>-RP exposure time. This result suggests that, after smaller dots are formed well-separately in the early stages, no further coalescence of the initially-formed Fe-NDs are promoted with increasing H<sub>2</sub>-RP exposure time reflecting a larger distance among them.

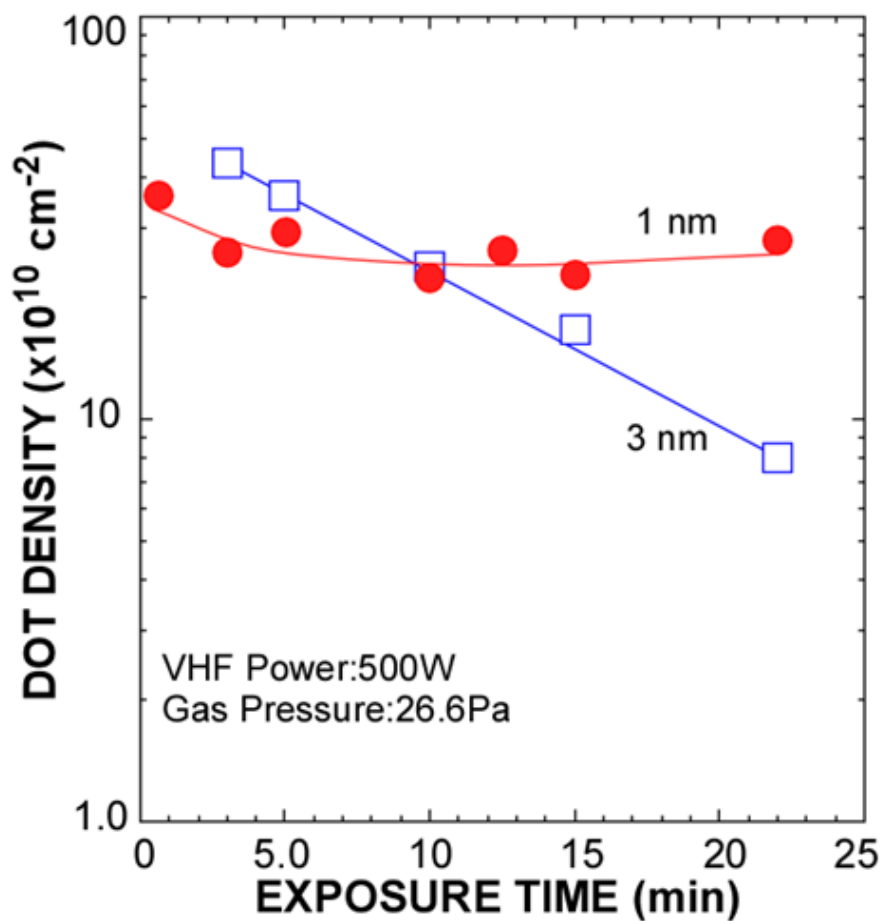


**Fig. 3.12.** Areal density of Fe-NDs formed by H<sub>2</sub>-RP exposure as functions of H<sub>2</sub>-RP exposure time, for ~1.0 and ~3.0 nm-thick initial Fe films. The VHF power and H<sub>2</sub> gas pressure during H<sub>2</sub>-RP exposure were maintained at 500 W and 26.6 Pa, respectively.

### 3.3.2 Formation mechanism of Fe-NDs induced by remote H<sub>2</sub> plasma

We have demonstrated a new technique to form high density Fe-NDs on SiO<sub>2</sub> by exposing an ultrathin Fe films deposition on SiO<sub>2</sub> to the H<sub>2</sub>-RP. The effect of H<sub>2</sub>-RP on the Fe-NDs formation and the influence of H<sub>2</sub>-RP were studied. After H<sub>2</sub>-RP exposures, a significant difference surface morphology in AFM images was obtained. The temperature of the thermocouple covered with a Fe foil was sharply increased during the H<sub>2</sub>-RP exposure. The result suggests that the migration of Fe atoms and agglomeration are promoted with local heating due to the efficient recombination of atomic hydrogen on Fe film surface [15], as shown in Fig. 3.13, because the agglomeration of the Fe atoms can minimize the interface energy by decreasing the contact region between Fe film and SiO<sub>2</sub>.

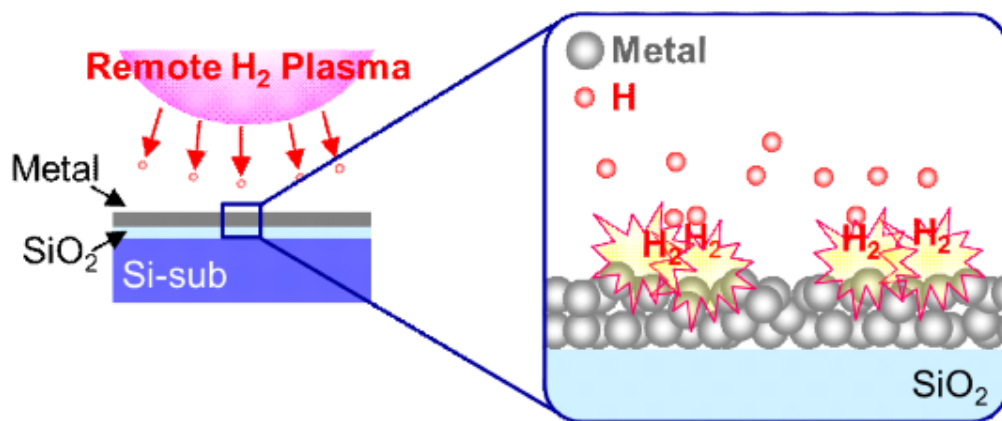


**Fig. 3.13.** Mechanism schematic diagram of metallic-NDs formation induced by H<sub>2</sub>-RP.

### 3.3.3 Magnetic properties of Fe nanodots

The magnetic properties of the Fe-NDs were evaluated by measuring in-plane and out-of-plane hysteresis loops with an applied magnetic field of  $\pm 600$  Oe using an alternation gradient magnetometer (AGM) at room temperature as shown in Fig. 3.14. Evident hysteretic loop showing a soft ferromagnetic nature at room temperature and magnetic anisotropic features were obtained.

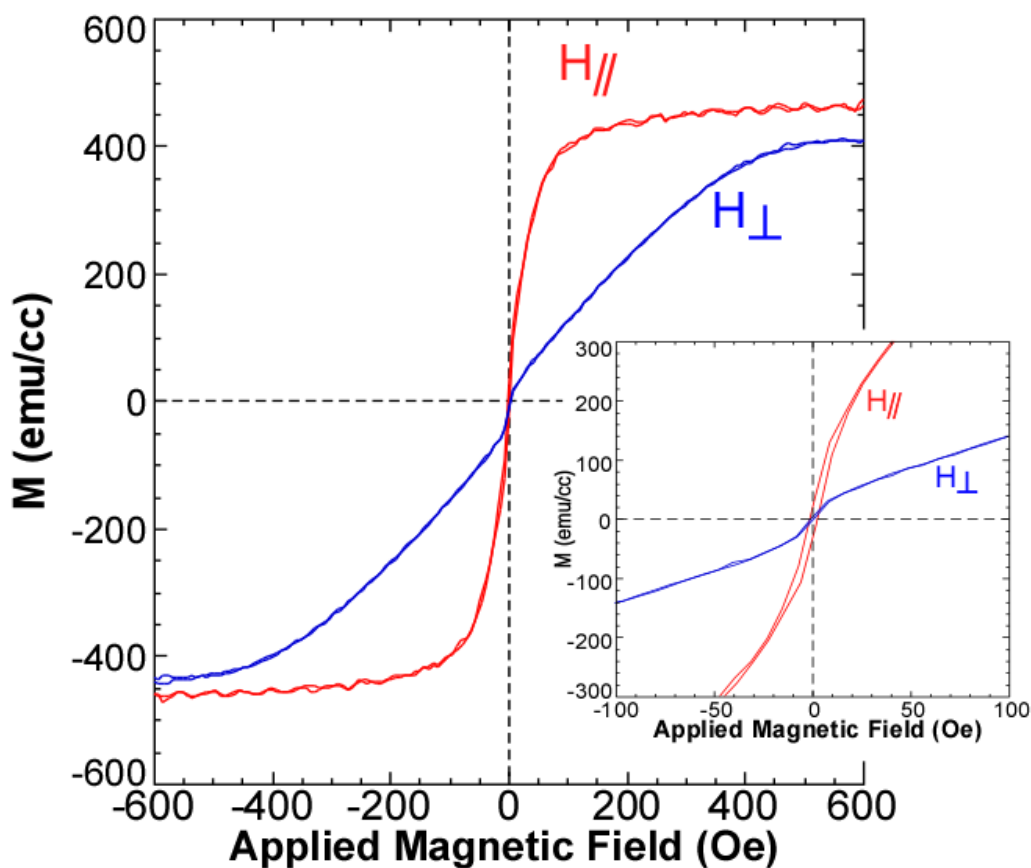


**Fig. 3.14.** In-plane and out-of-plane hysteresis loops taken with an applied magnetic field of  $\pm 600$  Oe at room temperature after H<sub>2</sub>-RP exposure. The hysteresis loops of in-plane and out-of-plane directions with an applied magnetic field of  $\pm 100$  Oe is shown in the inset.

We also measured magnetic force images by magnetic force microscopy (MFM) using a Si AFM tip coated with CoPtCr with a magnetization of 220 Oe, as shown in Fig. 3.15. MFM measurements were carried out in a vibrational mode using a phase detection system to measure the resonance frequency shifts resulting from the magnetic interaction between the AFM tip and the NDs. In the MFM image taken in a noncontact tapping mode with a distance of ~20 nm between the tip and the sample surface, as shown in Fig. 3.15 (b), a clear contrast was obtained with a good correlation to the Fe-NDs in the topographic image taken simultaneously [Fig. 3.15 (a)]. This contrast can be associated with a phase shift in the tip vibration due to the attractive

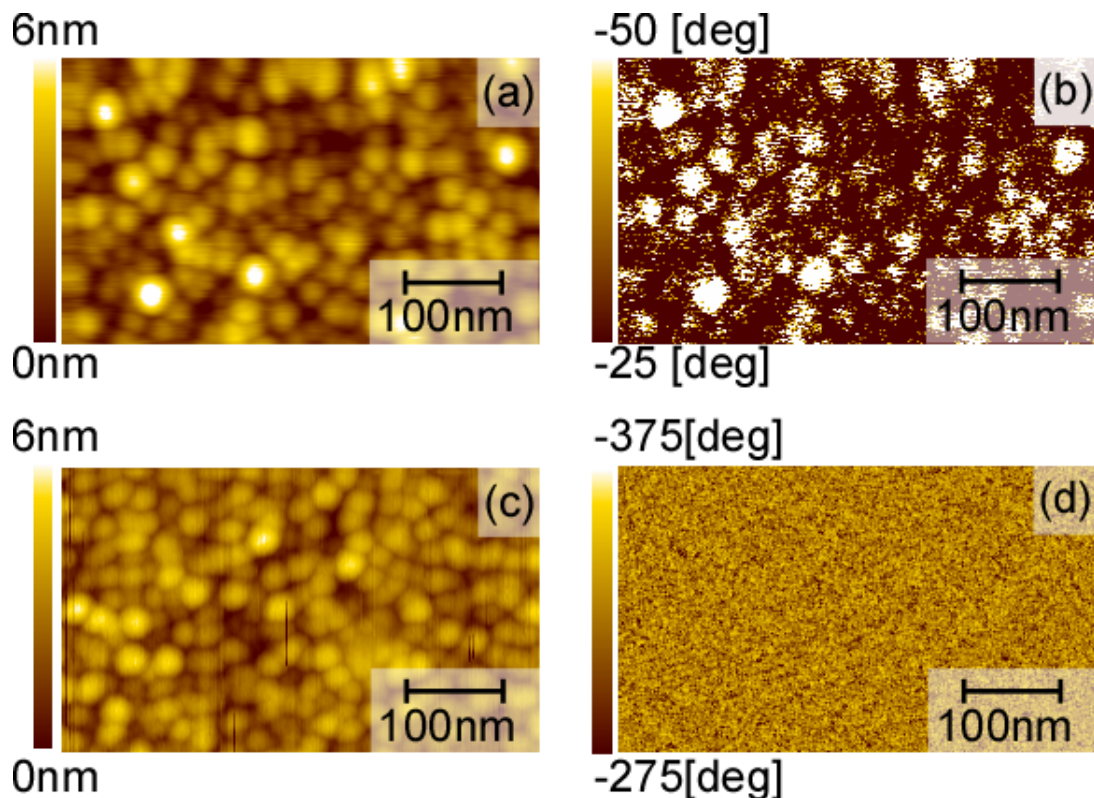


**Fig. 3.15.** (a, c) Topographic and (b, d) corresponding MFM images of Fe-NDs taken by a Si cantilever (a, b) with CoPtCr coating and (c, d) without CoPtCr coating.

interaction between the AFM tip and Fe-NDs [Figs. 3.15(b)]. It should be noted that, such a contrast in the MFM image was never detected by using a Si-cantilever [Fig. 3.15(d)]. These results suggest that Fe-NDs have a potential as spin dependent active elements as well as charge storage nodes.

### **3.4 Conclusions**

High density Fe-NDs have been fabricated by H<sub>2</sub>-RP exposure to nm-thick Fe layer on SiO<sub>2</sub> without external heating. The temperature raising of the Fe foil surface exposing to H<sub>2</sub>-RP indicates that the surface recombination of atomic hydrogen on the clean metal surface plays a role on the enhanced surface migration of Fe atoms. In changing the flux of atomic hydrogen with H<sub>2</sub> pressure and VHF power, the Fe-NDs formation was controlled in an areal density ranging from  $\sim 8.0 \times 10^{10}$  to  $\sim 2.4 \times 10^{11}$  cm<sup>-2</sup>. The results from XPS analysis imply that in the formation process of Fe-NDs, hydrogen radicals generated in H<sub>2</sub>-RP not only enhance surface migration of Fe atoms but also induce the reduction reaction of surface native Fe oxide. To achieve the formation of Fe-NDs electrical isolated each other with an areal density as high as  $10^{11}$  cm<sup>-2</sup>, the initial thickness of Fe films should be controlled below  $\sim 5$  nm. From surface potential and magnetic force image measurements, we also confirmed that the Fe-NDs could serve as spin-dependent charge storage nodes.

## References

- [1] M Mizuguchi, K Takanashi, M. Mizuguchi, and K. Takanashi, *J. Phys. D. Appl. Phys.* **44**, 64007 (2011).
- [2] F. Ernult, K. Yamane, S. Mitani, K. Yakushiji, K. Takanashi, et al., *Appl. Phys. Lett.* **84**, 3106 (2004).
- [3] Z. Liu, C. Lee, V. Narayanan, G. Pei, and E. C. Kan, *IEEE Trans. Electron Devices* **49**, 1606 (2002).
- [4] J. Dufourcq, P. Mur, M. J. Gordon, S. Minoret, R. Coppard, et al., *Mater. Sci. Eng. C* **27**, 1496 (2007).
- [5] T. Hikono, T. Matsumura, A. Miura, Y. Uraoka, T. Fuyuki, et al., *Appl. Phys. Lett.* **88**, 23108 (2006).
- [6] C.-K. Yin, M. Murugesan, J.-C. Bea, M. Oogane, T. Fukushima, et al., *Jpn. J. Appl. Phys.* **46**, 2167 (2007).
- [7] Z. Gai, B. Wu, J. P. Pierce, G. A. Farnan, D. Shu, et al., *Phys. Rev. Lett.* **89**, 235502 (2002).
- [8] C. M. Sun, H. K. Tsang, S. P. Wong, W. Y. Cheung, N. Ke, et al., *Appl. Phys. Lett.* **92**, 211902 (2008).
- [9] Y. Ozawa, *J. Appl. Phys.* **95**, 5483 (2004).
- [10] Y. Nakamura, S. Amari, S.-P. Cho, N. Tanaka, and M. Ichikawa, *Jpn. J. Appl. Phys.* **50**, 015501 (2011).
- [11] Y. Nakamura and M. Ichikawa, *Jpn. J. Appl. Phys.* **54**, 07JD01 (2015).
- [12] B. Matsukura, Y. Hiraiwa, T. Nakajima, K. Narumi, S. Sakai, et al., *Phys. Procedia* **23**, 21 (2012).
- [13] M. Uchida, N. Nagaosa, J. P. He, Y. Kaneko, S. Iguchi, et al., *Phys. Rev. B* **77**, 184402 (2008).
- [14] K. Makihara, K. Shimano, M. Ikeda, S. Higashi, and S. Miyazaki, *Jpn. J. Appl. Phys.* **47**, 3099 (2008).
- [15] K. Makihara, K. Shimano, A. Kawanami, M. Ikeda, S. Higashi, et al., *J. Optoelectron. Adv. Mater.* **12**, 626 (2010).
- [16] K. Shimano, K. Makihara, and M. Ikeda, *J. Appl. Phys.* **105**, 616 (2009).
- [17] T. Kitou, Y. Osaka, G. Yokota, M. Morioki, N. Kobayashi, et al., *J. Japan Soc. Energy Resour.* **33**, 10 (2012).

- [18] A. Kawanami, K. Makihara, M. Ikeda, and S. Miyazaki, *Jpn. J. Appl. Phys.* **49**, 08JA04 (2010).
- [19] A. P. Grosvenor, B. A. Kobe, M. C. Biesinger, and N. S. McIntyre, *Surf. Interface Anal.* **36**, 1564 (2004).
- [20] R. H. Fowler, *Statistical Mechanics, the Theory of the Properties of Mater in Equilibrium* (Cambridge, University Press, 1966) 2nd ed.
- [21] S. Miyazaki, H. Yoshinaga, A. Ohta, Y. Akasaka, K. Shiraishi, K. Yamada, S. Inumiya, M. Kadoshima, and Y. Nara, *ECS Trans.* **13** (6), 67 (2008).
- [22] D. E. Eastman, *Phys. Rev. B* **2**, 1 (1970).
- [23] H. B. Michaelson, *J. Appl. Phys.* **48**, 4729 (1977).

## Chapter 4

### **Formation of Fe-silicide nanodots on SiO<sub>2</sub> from Fe/Si/Fe trilayer stacks by exposure to remote H<sub>2</sub> plasma**

In this chapter, we demonstrated the formation of high-density iron silicide nanodots (NDs) on a thermally grown SiO<sub>2</sub> by exposing an electron-beam-evaporated Fe/amorphous-Si/Fe (Fe/a-Si/Fe) trilayer stack to remote H<sub>2</sub> plasma without any external heating and characterized their silicidation state and crystalline phase. After the remote H<sub>2</sub> plasma exposure, the formation of NDs with an areal density of  $\sim 4.3 \times 10^{11} \text{ cm}^{-2}$  and an average height of  $\sim 7.1 \text{ nm}$  was confirmed. X-ray photoelectron spectroscopy (XPS) analyses indicate the silicidation reaction induced by the remote H<sub>2</sub> plasma exposure, which was accompanied by the agglomeration of Fe and Si atoms on the SiO<sub>2</sub> surface. The formation of a crystalline  $\beta\text{-FeSi}_2$  phase was confirmed by Raman scattering spectroscopy and XRD pattern measurements. The electrical separation among the  $\beta\text{-FeSi}_2$  NDs was confirmed from changes in surface potential due to charging of the dots. The surface potential of the NDs changed in a stepwise manner with respect to the tip voltage because of multistep electron injection into and extraction from the semiconductor  $\beta\text{-FeSi}_2$  NDs.

## 4.1 Introduction

The formation of semiconducting or metallic nanodots (NDs) has attracted considerable interest owing to their potential applications to nanodevices such as optoelectronic [1-4] and information storage devices [5-8]. Therefore, researches on NDs as novel materials with unique optical, electrical, and magnetic properties have been studied extensively. Among these materials, Fe-silicides have received significant attention because of their various electronic and magnetic properties depending on their composition and phases, such as  $\beta$ -FeSi<sub>2</sub> and Fe<sub>3</sub>Si. It is known that  $\beta$ -FeSi<sub>2</sub> is a semiconductor with a direct bandgap of about 0.84-0.87eV, and that Fe<sub>3</sub>Si is a ferromagnetic material [9-13]. Specifically, the semiconducting  $\beta$ -FeSi<sub>2</sub> has been proposed as a promising material that is compatible with Si-based microelectronics technology for optoelectronic applications, such as light-emitting diodes (LEDs) [14-19], photovoltaics [20], and near-infrared (NIR) photodetectors in optical fiber telecommunications [21]. Although various methods including molecular beam epitaxy [17, 19, 22], reactive deposition epitaxy (RDE) [15, 16, 23], magnetron sputtering [21, 24, 25], and ion beam synthesis [20, 26] have been attempted to grow Fe-silicide thin films on Si, the formation of Fe-silicide NDs was rarely reported. Nakamura et al. developed a technique for epitaxially growing iron silicide NDs on Si substrates [27]. However, in the application of iron silicide NDs to Si-based light emitters and spintronic devices, the high-density formation of Fe-silicide NDs on SiO<sub>2</sub> is one of major concerns. Previously, Miyazaki's group reported that metal NDs such as Ni [28], Pt [29], Co [30], and Fe [31] with an areal density as high as  $\sim 10^{11}$  cm<sup>-2</sup> were

*Formation of Fe-silicide nanodots on SiO<sub>2</sub> from Fe/Si/Fe trilayer stacks by exposure to remote H<sub>2</sub> plasma*

---

formed on SiO<sub>2</sub> by exposing ultrathin metal layers to remote H<sub>2</sub> plasma (H<sub>2</sub>-RP) without external heating, in which the migration of metal atoms is driven by local heating caused by the efficient recombination of atomic hydrogen on a metal surface, and demonstrated their charge storage capability [8, 28-30]. In this chapter, we extended our research to the formation of Fe-silicide NDs by exposing an electron-beam-evaporated Fe/a-Si/Fe trilayer stack to the H<sub>2</sub>-RP.

## **4.2 Sample preparation and characterizations**

After conventional wet-chemical cleaning steps for p-type Si(100) wafers, a ~5.0-nm-thick SiO<sub>2</sub> layer was grown at 850 °C in 2% O<sub>2</sub> diluted with N<sub>2</sub>. After that, a ~1.8-nm-thick Fe layer was first deposited uniformly on the SiO<sub>2</sub> layer by electron beam evaporation, and then covered uniformly with a ~1.0-nm-thick amorphous Si (a-Si) layer without air exposure. Subsequently, a ~1.8-nm-thick Fe layer was deposited. As a reference, a ~3.6-nm-thick Fe single layer was also deposited on SiO<sub>2</sub> by electron beam evaporation. Both the as-prepared Fe/a-Si/Fe trilayer stack and the single Fe layer were exposed simply to H<sub>2</sub>-RP without any external heating. The plasma was generated by inductive coupling with an external single-turn antenna connected to a 60 MHz generator through a matching circuit. During the H<sub>2</sub>-RP exposure, hydrogen gas pressure and VHF power were maintained at 13.3 Pa and 500 W, respectively. The areal dot density was evaluated by atomic force microscopy (AFM). The effect of H<sub>2</sub>-RP exposure on chemical bonding features in the Fe/a-Si/Fe trilayer stack was characterized by high-resolution X-ray photoelectron spectroscopy (XPS) using a monochromatized Al K $\alpha$  (1486.6 eV) radiation. The crystal phase of NDs was characterized by Raman scattering spectroscopy and X-ray diffraction (XRD) measurements. Electrical separation among the as-prepared NDs was also verified by surface potential measurements using an AFM/Kelvin force microscopy (KFM) technique as described in detail in our previous works [28-31].

## 4.3 Results and discussion

### 4.3.1 Evaluation of chemical composition and bonding features of nanodots

Figures 4.1(a) and (b) show topographic AFM images for the as-evaporated 1.8-nm-thick Fe layer on a-Si (1.0 nm)/Fe (1.8 nm)/SiO<sub>2</sub> and single-layer 3.6-nm-thick Fe/SiO<sub>2</sub> before H<sub>2</sub>-RP exposure, respectively. Both AFM images show a smooth surface morphology with a root-mean-square (RMS) roughness as small as ~0.28 nm, which is almost identical to that for the as-grown SiO<sub>2</sub> surface. The results confirm a uniform surface coverage with both the ultrathin Fe/a-Si/Fe trilayer stack and the Fe single layer on SiO<sub>2</sub>. By exposing the Fe/a-Si/Fe trilayer stack on SiO<sub>2</sub> to the H<sub>2</sub>-RP for 10 min, the RMS roughness was increased by a factor of ~4 and the formation of

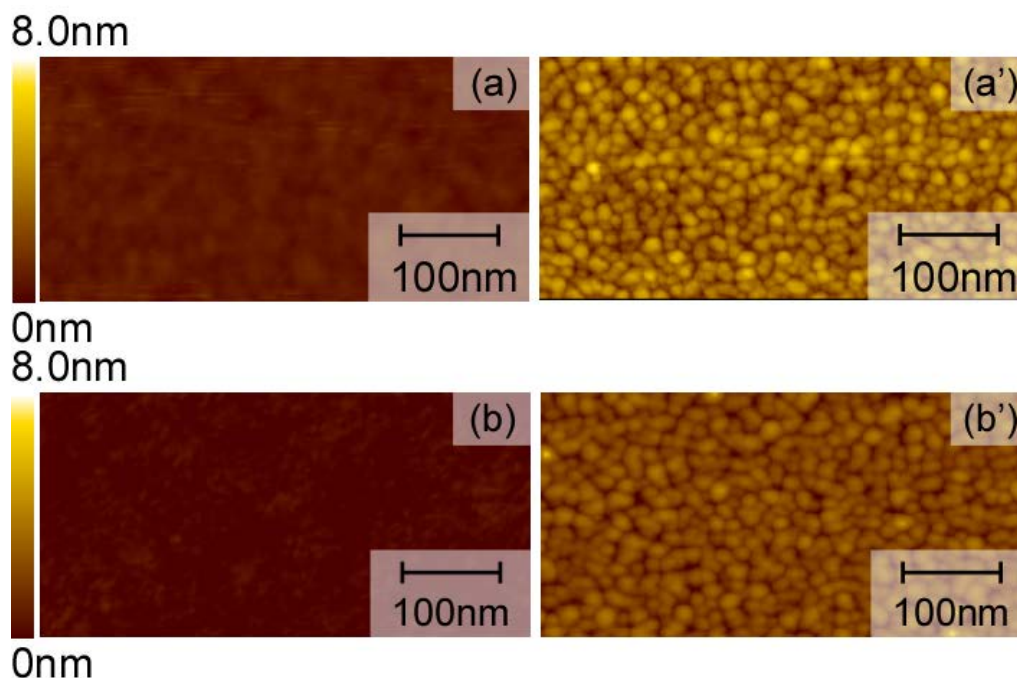


**Fig. 4.1.** Topographic images (a, a') of Fe/a-Si/Fe ultrathin trilayer stack structures and (b, b') single Fe layer taken (a, b) before and (a', b') after H<sub>2</sub>-RP exposure.

NDs with an areal density as high as  $\sim 4.3 \times 10^{11} \text{ cm}^{-2}$  was observed, as shown in Fig. 4.1(a'). In addition, for the single Fe layer with a thickness of  $\sim 3.6 \text{ nm}$ , the formation of Fe-NDs with an areal density of  $\sim 4.0 \times 10^{11} \text{ cm}^{-2}$  and an increase in RMS roughness were observed after H<sub>2</sub>-RP exposure [Fig. 4.1(b')].

By fitting the measured size distribution of NDs to a log-normal function, the average dot height was determined to be  $\sim 4.0$  and  $\sim 7.1 \text{ nm}$  for the single Fe layer and Fe/a-Si/Fe trilayer stack, respectively, as shown in Fig. 4.2. Note that the average dot height of the trilayer stack is increased by a factor of  $\sim 2$  in comparison with that of the Fe single layer. Tanaka et al. reported that the thickness of the  $\beta\text{-FeSi}_2$  film formed by RDE is nearly 3 times larger than that of the initial iron film [23]. In our case, taking into account the agglomeration of Fe and Si atoms in the formation of NDs in a three-dimensional direction, the increase in average dot height is consistent with the

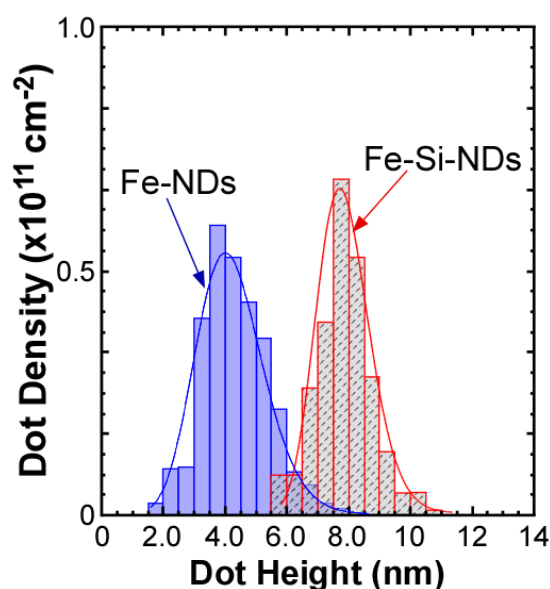


**Fig. 4.2.** Distribution of dot height obtained from AFM images corresponding to Figs. 4.1(a') and (b'). Solid lines denote the log-normal functions well fitted to the measured distributions.

result calculated from the theoretical densities of Fe, Si, and  $\beta$ -FeSi<sub>2</sub>. In addition, it was found that the temperature of an Fe foil increased up to ~500 °C during H<sub>2</sub>-RP exposure [31]. According to the above results, we expect that the silicidation will be promoted by remote H<sub>2</sub> plasma treatment with agglomeration through the cohesive action of Fe and Si atoms on the SiO<sub>2</sub> surface.

To confirm the silicidation of H<sub>2</sub>-plasma-treated Fe/a-Si/Fe trilayer stacked structures, chemical bonding features were characterized by high-resolution XPS. Figure 4.3 shows the Fe 2p<sub>3/2</sub> and Si 2p core-line spectra measured for the Fe/a-Si/Fe trilayer stacked structures on SiO<sub>2</sub>/Si (100) before and after the H<sub>2</sub>-RP exposure with a take-off angle of 90°. In Fe 2p<sub>3/2</sub> spectra, metallic Fe signals such as Fe-Fe and/or Fe-Si bonds markedly increased with a decrease in the amount of the Fe oxide component after the

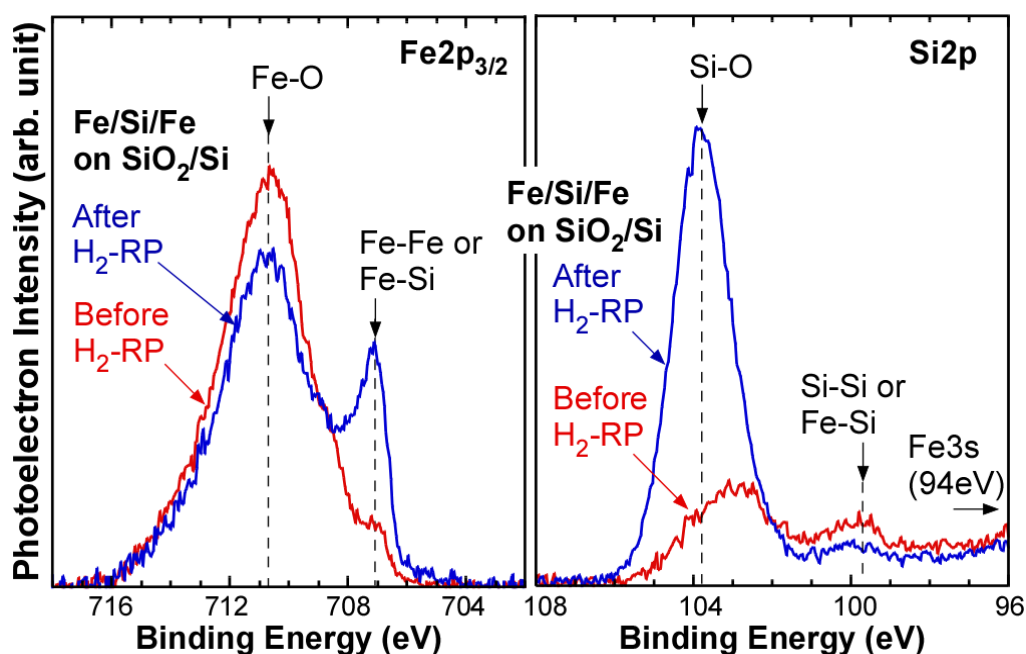


**Fig. 4.3.** Fe 2p<sub>3/2</sub> and Si 2p spectra taken before and after H<sub>2</sub>-RP exposure of Fe/a-Si/Fe ultrathin trilayer stack formed on SiO<sub>2</sub>.

H<sub>2</sub>-RP exposure, which indicates that a reduction reaction in a certain part of the surface Fe oxide proceeds during H<sub>2</sub>-RP exposure. On the other hand, Si 2p signals originating from the Si-O bonding units became significant after the H<sub>2</sub>-RP exposure. This result can be interpreted as revealing the underlying SiO<sub>2</sub> layer resulting from the formation of the Fe-silicide NDs. The formation of Fe-silicide was also confirmed from the depth profiling of the chemical structure based on the photoelectron take-off angle dependence of the core-line signals, as shown in Fig. 4.4. Fe 2p<sub>3/2</sub> and Si 2p spectra were taken with take-off angles of 90 and 30° and photoelectron intensities were normalized by metallic Fe 2p<sub>3/2</sub> signals.

In these spectra, no significant change in intensity ratio between metallic Fe and Si signals with different photoelectron take-off angles was observed. This result implies

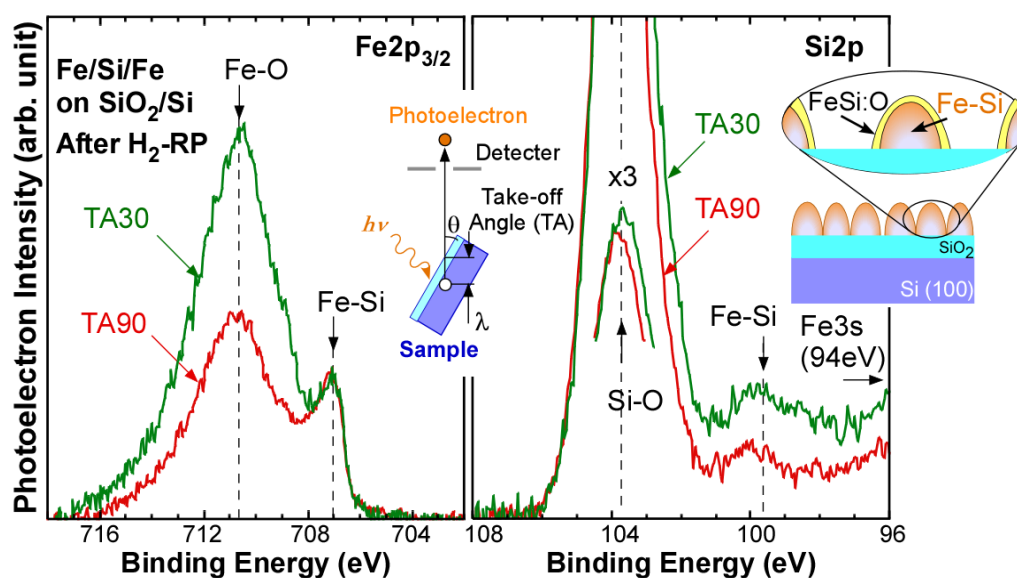


**Fig. 4.4.** Fe 2p<sub>3/2</sub> and Si 2p spectra for the sample after H<sub>2</sub>-RP exposure measured at two different photoelectron take-off angles of 30 and 90°. In each spectrum, the intensity was normalized by Fe 2p<sub>3/2</sub> signals due to the metallic Fe.

that the depth profiles of Fe and Si atom concentrations are constant; in other words, it implies the formation of Fe-silicide. Moreover, an increase in the signal intensity of the Fe-O bonding unit with a decrease in take-off angle indicates the formation of Fe oxide in the region near the dot surface probably owing to air exposure. From these results, we can conclude that the NDs are composed of an Fe-silicide core and a surface iron oxide layer, as represented in the inset of Fig. 4.4.

### 4.3.2 Structural characterization of nanodots

To determine the crystalline phase before and after the H<sub>2</sub>-RP exposure, the Raman scattering spectrum were also measured as shown in Fig. 4.5. For the Fe/a-Si/Fe trilayer stack prior to the H<sub>2</sub>-RP exposure, no characteristic peaks were observed except

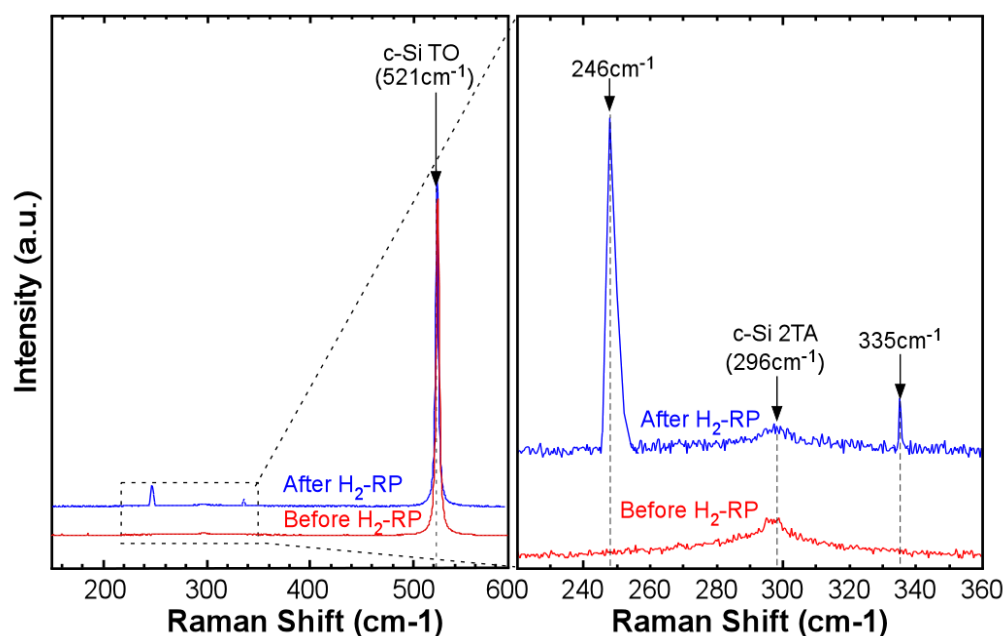


**Fig. 4.5.** Raman scattering spectra taken before and after H<sub>2</sub>-RP exposure of Fe/a-Si/Fe ultrathin trilayer stack.

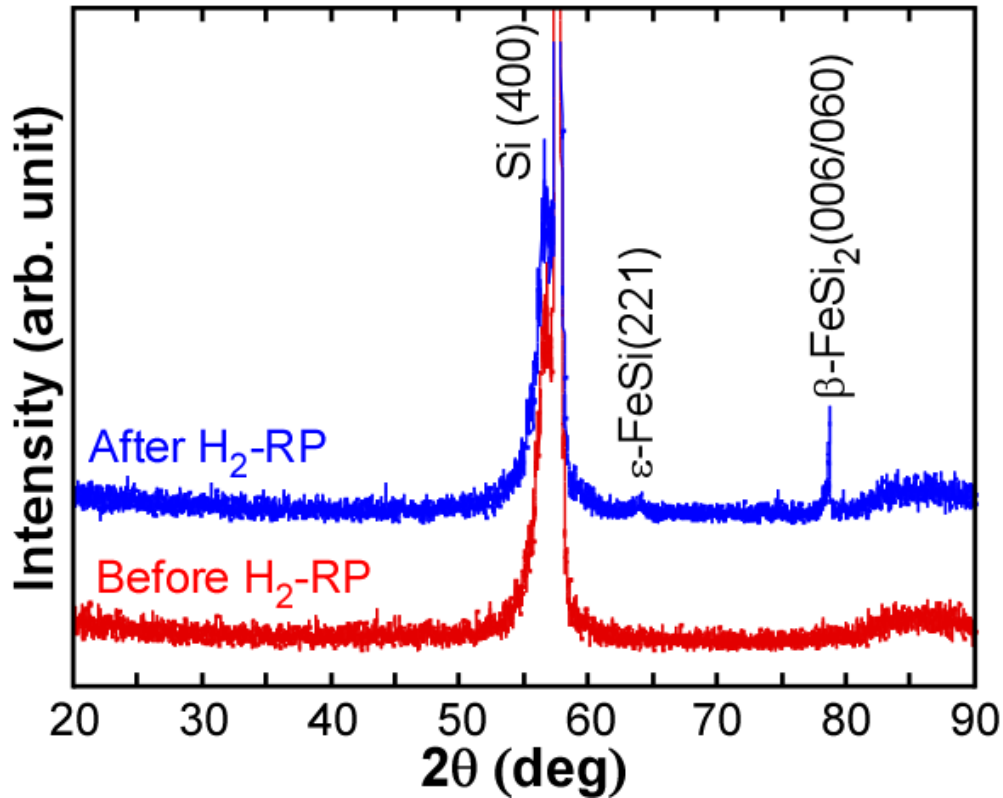


**Fig. 4.6.** XRD patterns of Fe/a-Si/Fe ultrathin trilayer stack structures before and after H<sub>2</sub>-RP exposure measured at an incident angle of 4°.

for the signals at 521 and 296 cm<sup>-1</sup> assigned to the Si substrates. On the other hand, two sharp peaks from the NDs were clearly identified at ~246 and 335 cm<sup>-1</sup>, which originated from Fe-Si vibrational modes, reflecting the formation of the β-FeSi<sub>2</sub> phase [32, 33]. Here, we note that the Raman peaks of the as-prepared NDs are slightly shifted toward the lower wavenumber side by ~5 cm<sup>-1</sup> compared with those obtained theoretically in bulk β-FeSi<sub>2</sub> [34]. This shift is mainly explained by the phonon confinement and the tensile strain in the β-FeSi<sub>2</sub> NDs [35, 36]. The agglomeration of the NDs can minimize the interface energy by decreasing the contact region between β-FeSi<sub>2</sub> and SiO<sub>2</sub>. But, as a result, a strain may be still residual. Another possible reason for the peak shift is that the surface oxidation layer induced a deficiency of iron

atoms in the lattice of  $\beta$ -FeSi<sub>2</sub>, which results in an increase in the bonding length or a decrease in the force constant. These are in very good agreement with the results previously published by Maeda and Miyake [37]. In addition, from XRD patterns, a sharp signal for the NDs was detected at  $\sim 78.8^\circ$ . This signal is originated from  $\beta$ -FeSi<sub>2</sub>, although no characteristic peaks were observed for the Fe/a-Si/Fe trilayer stack prior to the H<sub>2</sub>-RP exposure except with the c-Si (100) substrates, as shown in Fig. 4.6. These results imply that the  $\beta$ -FeSi<sub>2</sub> phase is dominant.

### 4.3.3 Charging and discharging characteristics of $\beta$ -FeSi<sub>2</sub> nanodots

To confirm the electrical isolation among the  $\beta$ -FeSi<sub>2</sub> NDs, the topographic and corresponding surface potential images were simultaneously taken in the KFM mode before and after scanning an electrically biased Rh-coated AFM tip on the sample surface, as shown in Fig. 4.7. Without any bias applied to the sample surface, a

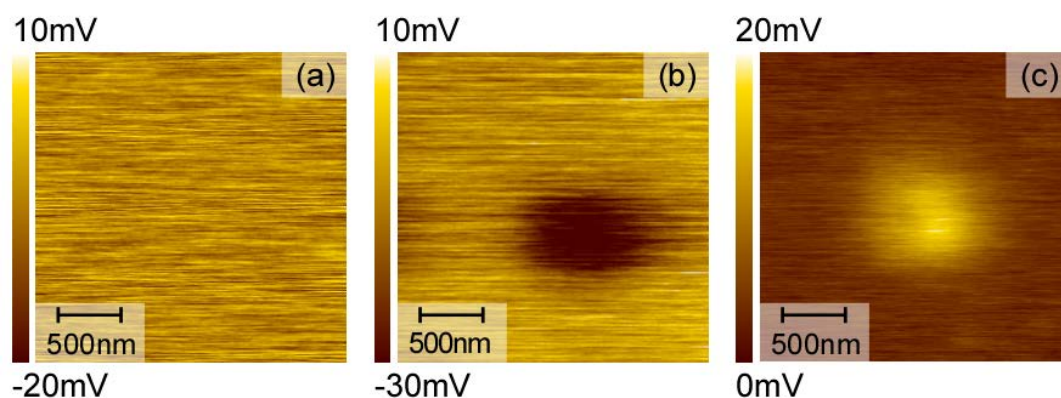


**Fig. 4.7.** Surface potential images of  $\beta$ -FeSi<sub>2</sub> NDs corresponding to Fig. 4.1(a') measured (a) before and after electron injection and extraction at tip biases of (b) -3.0 V and (c) +3.0 V. The surface potential was measured in the non-contact Kelvin probe mode after tapping the sample surface with an electrically biased AFM tip coated with Rh.

uniform surface potential image was observed [Fig. 4.7(a)]. When the AFM tip was biased at -3.0 V with respect to the substrate and scanned on the sample surface with an area of  $500 \times 500 \text{ nm}^2$ , an approximately 30 mV decrease in surface potential in the scanned area owing to electron charging to the dots was observed. However, in the unbiased area, no change in surface potential was detected [Fig. 4.7(b)]. On the other hand, by scanning with the tip biased at +3.0 V, the surface potential was increased [Fig. 4.7(c)]. These results indicate that the NDs were electrically isolated from each other. In addition, before the H<sub>2</sub>-RP exposure of the trilayer, no change in the surface potential

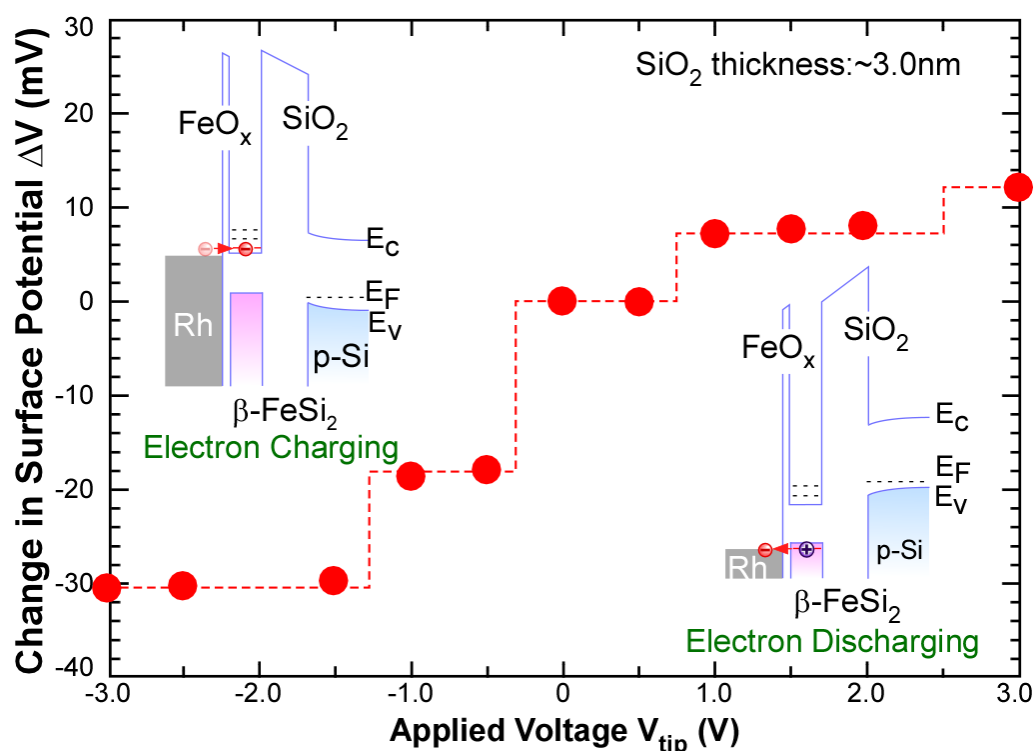


**Fig. 4.8.** Change in surface potential caused by electron injection into and extraction from  $\beta\text{-FeSi}_2$  NDs on SiO<sub>2</sub> (~3.0 nm)/p-Si (100) as a function of tip-bias voltage. The energy band diagram is schematically illustrated in the inset, which shows electron injection and hole injection to the dots from the Rh-coated tip at -0.5 and 1.0 V, respectively.

was observed after applying tip biases because of an electrically conductive surface. The difference between the surface potential changes observed before and after the plasma treatment indicates the migration of Fe and Si atoms in between the dots to reveal the SiO<sub>2</sub> surface during the H<sub>2</sub>-RP treatment.

The change in surface potential as a function of applied tip bias was evaluated from the surface potential images, as summarized in Fig. 4.8. In this case, the NDs were formed on the 3-nm-thick SiO<sub>2</sub> layer. In the tip biases in the range from -3 to +3 V, the surface potential on the dots was changed in a stepwise manner by electron injection to and emission from the  $\beta$ -FeSi<sub>2</sub> NDs. This result can be interpreted in terms of the multistep electron and hole charging characteristics of  $\beta$ -FeSi<sub>2</sub> NDs associated with the discrete charging energy of  $\beta$ -FeSi<sub>2</sub> NDs, as described in the inset of Fig. 4.8.

#### **4.4 Conclusions**

We demonstrated a novel technique for the formation of iron silicide NDs on thermally grown SiO<sub>2</sub> with an areal density as high as  $\sim 10^{11}$  cm<sup>-2</sup>, in which the silicidation reaction and the agglomeration of an ultrathin Fe/a-Si/Fe trilayer stack with cohesive Fe and Si atoms on the SiO<sub>2</sub> surface were promoted by the H<sub>2</sub>-RP exposure without external heating. This technique is very promising for the formation of various phases of iron silicide NDs on SiO<sub>2</sub>.

## References

- [1] R. J. Walters, G. I. Bourianoff, and H. A. Atwater, *Nat. Mater.* **4**, 143 (2005).
- [2] S. M. Park, C. H. Bae, W. Nam, S. C. Park, and J. S. Ha, *Appl. Phys. Lett.* **86**, 15 (2005).
- [3] A. J. Nozik, *Physica E* **14**, 115 (2002).
- [4] M. Kroutvar, Y. Ducommun, D. Heiss, M. Bichler, D. Schuh, G. Abstreiter, and J. J. Finley, *Nature* **432**, 81 (2004).
- [5] Z. Liu, C. Lee, V. Narayanan, G. Pei, and E. C. Kan, *IEEE Trans. Electron Devices* **49**, 1606 (2002).
- [6] T. Sakaguchi, Y. G. Hong, M. Kobayashi, M. Takata, H. Choi, J. C. Shim, H. Kurino, and M. Koyanagi, *Jpn. J. Appl. Phys.* **43**, 2203 (2004).
- [7] T. Shibaguchi, M. Ikeda, H. Murakami, and S. Miyazaki, *IEICE Trans. Electron.* **E88-C**, 709 (2005).
- [8] S. Miyazaki, K. Makihara, and M. Ikeda, *Thin Solid Films* **518**, S30 (2010).
- [9] W. A. Hines, A. H. Menotti, J. I. Budnick, T. J. Burch, T. Litrenta, V. Niculescu, and K. Raj, *Phys. Rev. B* **13**, 4060 (1976).
- [10] O. K. von Goldbeck, *IRON—Binary Phase Diagrams* (Springer, Heidelberg, 1982) p. 136.
- [11] M. C. Bost and J. E. Mahan, *J. Appl. Phys.* **58**, 2696 (1985).
- [12] C. Fu, M. Krijn, and S. Doniach, *Phys. Rev. B* **49**, 2219 (1994).
- [13] K. Hamaya, K. Ueda, Y. Kishi, Y. Ando, T. Sadoh, and M. Miyao, *Appl. Phys. Lett.* **93**, 132117 (2008).
- [14] D. Leong, M. Harry, K. J. Reeson, and K. P. Homewood, *Nature* **387**, 686 (1997).
- [15] T. Suemasu, Y. Negishi, K. Takakura, and F. Hasegawa, *Jpn. J. Appl. Phys.* **39**, L1013 (2000).
- [16] T. Suemasu, K. Takakura, C. Li, Y. Ozawa, Y. Kumagai, and F. Hasegawa, *Thin Solid Films* **461**, 209 (2004).
- [17] M. Takauji, N. Seki, T. Suemasu, F. Hasegawa, and M. Ichida, *J. Appl. Phys.* **96**, 2561 (2004).
- [18] Y. Maeda, *Thin Solid Films* **515**, 81 (2007).
- [19] M. Suzuno, T. Koizumi, and T. Suemasu, *Appl. Phys. Lett.* **94**, 213509 (2009).

- [20] Y. Maeda, K. Umezawa, Y. Hayashi, K. Miyake, and K. Ohashi, *Thin Solid Films* **381**, 256 (2001).
- [21] S. Izumi, M. Shaban, N. Promros, K. Nomoto, and T. Yoshitake, *Appl. Phys. Lett.* **102**, 032107 (2013).
- [22] T. Suemasu, Y. Ugajin, S. Murase, T. Sunohara, and M. Suzuno, *J. Appl. Phys.* **101**, 124506 (2007).
- [23] M. Tanaka, Y. Kumagai, T. Suemasu, and F. Hasegawa, *Jpn. J. Appl. Phys.* **36**, 3620 (1997).
- [24] S. Nakamura, T. Aoki, T. Kittaka, R. Hakamata, H. Tabuchi, S. Kunitsugu, and K. Takarabe, *Thin Solid Films* **515**, 8205 (2007).
- [25] T. Ehara, Y. Sasaki, K. Saito, S. Nakagomi, and Y. Kokubun, *Appl. Surf. Sci.* **175-176**, 96 (2001).
- [26] Y. Maeda, K. Umezawa, Y. Hayashi, and K. Miyake, *Thin Solid Films* **381**, 219 (2001).
- [27] Y. Nakamura, Y. Nagadomi, S. P. Cho, N. Tanaka, and M. Ichikawa, *Phys. Rev. B* **72**, 075404 (2005).
- [28] K. Makihara, K. Shimano, M. Ikeda, S. Higashi, and S. Miyazaki, *Jpn. J. Appl. Phys.* **47**, 3099 (2008).
- [29] K. Makihara, K. Shimano, A. Kawanami, M. Ikeda, S. Higashi, and S. Miyazaki, *J. Optoelectron. Adv. Mater.* **12**, 626 (2010).
- [30] A. Kawanami, K. Makihara, M. Ikeda, and S. Miyazaki, *Jpn. J. Appl. Phys.* **49**, 08JA04 (2010).
- [31] H. Zhang, R. Fukuoka, Y. Kabeya, K. Makihara, and S. Miyazaki, *Adv. Mater. Res.* **750-752**, 1011 (2013).
- [32] H. Kakemoto, Y. Makita, Y. Kino, S. Sakuragi, and T. Tsukamoto, *Thin Solid Films* **381**, 251 (2001).
- [33] R. Ayache, A. Bouabellou, and E. Richter, *Mater. Sci. Semicond. Process.* **7**, 463 (2004).
- [34] Y. Maeda, H. Udono, and Y. Terai, *Thin Solid Films* **461**, 165 (2004).
- [35] S. Osswald, V. N. Mochalin, M. Havel, G. Yushin, and Y. Gogotsi, *Phys. Rev. B* **80**, 075419 (2009).
- [36] H. T. Chen, X. L. Wu, Y. Y. Zhang, and W. N. Su, *Appl. Phys. a-Materials Sci. Process.* **97**, 725 (2009).

*Formation of Fe-silicide nanodots on SiO<sub>2</sub> from Fe/Si/Fe trilayer stacks by exposure to remote H<sub>2</sub> plasma*

---

[37] Y. Maeda and K. Miyake, Jpn. J. Appl. Phys. **39**, 4051 (2000).

## Chapter 5

### Phase controlled formation of Fe<sub>3</sub>Si nanodots

We demonstrated formation of Fe<sub>3</sub>Si-NDs by exposing a Fe/a-Si/Fe trilayer stack on SiO<sub>2</sub> to H<sub>2</sub>-RP and characterized their crystalline phases and magnetization properties. The formation of electrically isolated DO<sub>3</sub> ordered Fe<sub>3</sub>Si-NDs with an areal density of  $\sim 10^{11}$  cm<sup>-2</sup> was confirmed. These results imply that the surface migration and agglomeration of Fe and Si atoms induced by H<sub>2</sub>-RP were promoted simultaneously with the ordering crystallization reaction. We examined the dependence of magnetic properties of Fe<sub>3</sub>Si-NDs on the H<sub>2</sub>-RP gas pressure and found that the saturation magnetization at 20 Pa was  $\sim 800$  emu/cc which is almost equal to that of DO<sub>3</sub>-ordered Fe<sub>3</sub>Si film, and the saturation magnetizations of Fe<sub>3</sub>Si-NDs exposed at the different gas pressure show small difference in value. The variation of the saturation magnetization can be interpreted considering that the surface temperature during H<sub>2</sub>-RP exposure, which increased with the H<sub>2</sub> pressure increasing, contributes to crystal structure formation of Fe-silicide-NDs. By controlling the thickness ratio of Fe/a-Si/Fe trilayer stack structure and gas pressure of H<sub>2</sub>-RP, crystalline phase of Fe-silicide-NDs can be controlled.

## **5.1 Introduction**

Iron silicides (Fe-silicides) have attracted considerable attention in the last decade because they have various phases such as the semiconducting  $\beta$ -FeSi<sub>2</sub> [1-4], nonmagnetic metallic FeSi [5–8], and ferromagnetic Fe<sub>3</sub>Si [9-13]. The ferromagnetic silicide Fe<sub>3</sub>Si has a high Curie temperature above ~800 K [10-13], and it possesses two representative types of ordered B2 and DO<sub>3</sub> structures [1, 14]. DO<sub>3</sub> type Fe<sub>3</sub>Si can be regarded as a Heusler alloy Fe<sub>2</sub>FeSi, which is spin-polarized at the Fermi level [15-18]. Therefore, Fe<sub>3</sub>Si is an attractive material for Si-based spintronic applications. On the other hand, in nanostructures such as NDs, large surface to volume ratio and low dimensional properties often lead to novel electronic and crystallographic structures. As a result, their physical properties of nanostructured materials can be changed dramatically in comparison with their bulk state, which are also utilized for achieving enhanced functionality for future technological applications [19, 20]. Magnetic NDs have been intensively studied owing to its potentials for new applications in the future including ultrahigh density magnetic data storage and a novel nonvolatile memory [21]. Fe<sub>3</sub>Si-NDs have also attracted much interest due to high saturation magnetization and a relatively high spin polarization. So far, although various methods including pulsed-laser deposition (PLD) [22, 23], solid phase epitaxy(SPE) [24], molecular-beam epitaxy (MBE) [13, 16, 18, 25-27] and sputtering [14] have been attempted to grow Fe<sub>3</sub>Si thin films on Si or Ge, there are few reports on the formation of Fe<sub>3</sub>Si-NDs on SiO<sub>2</sub>. Recently, Nakamura et al. developed a technique for epitaxial growth of Fe<sub>3</sub>Si-NDs on Si substrates and investigated magnetic properties of Fe<sub>3</sub>Si-NDs [28, 29].

While they observed small saturation magnetization ( $M_S$ ) in Fe<sub>3</sub>Si-NDs at room temperature (RT), the discrepancy in the  $M_S$  between NDs and film has not been elucidated yet. In the application of Fe<sub>3</sub>Si-NDs to Si-based spintronic devices such as magnetic nanodots floating gate memory and high density record medium [30], high density NDs are required. Therefore, the high-density formation of ferromagnetic Fe<sub>3</sub>Si-NDs on SiO<sub>2</sub> and clarification of their magnetic properties are one of major concerns. In chapter 4, we demonstrated the formation of the  $\beta$ -FeSi<sub>2</sub> NDs with an areal density as high as  $\sim 10^{11}$  cm<sup>-2</sup> by exposure of a Fe/amorphous-Si/Fe trilayer stack structures to H<sub>2</sub>-RP without external heating [31]. In this chapter, we described the successful formation of high-density ferromagnetic Fe<sub>3</sub>Si-NDs on SiO<sub>2</sub> by controlling the initial Fe/Si thickness ratio and the H<sub>2</sub>-RP gas pressure based on the result of Chapter 4. The influences of the H<sub>2</sub>-RP gas pressure on magnetic properties and the crystal phase of Fe<sub>3</sub>Si-NDs are also discussed.

## **5.2 Experimental procedure**

After conventional wet-chemical cleaning steps for p-type Si(100) wafers, a ~3.6-nm-thick SiO<sub>2</sub> layer was grown at 850 °C in 2% O<sub>2</sub> diluted with N<sub>2</sub>. After that, a ~2.0-nm-thick Fe layer was first deposited uniformly on the SiO<sub>2</sub> layer by electron beam evaporation, and then covered uniformly with a ~2.0-nm-thick amorphous Si (a-Si) layer without air exposure. Subsequently, a ~1.5-nm-thick Fe layer was deposited, where the film thicknesses were designed with stoichiometric ratios of Fe:Si=3:1. The deposition rate was ~0.1nm/s. The Fe/a-Si/Fe trilayer stack so-prepared was exposed to a H<sub>2</sub>-RP without external heating. Gas pressure was changed in the range from 9 to 27 Pa. The plasma was generated by inductive coupling with an external single-turn antenna connected to a 60-MHz generator through a matching circuit. The VHF power and the exposure time were kept constant at 500 W and 10 min, respectively. The surface morphologies before and after H<sub>2</sub>-RP exposure were observed by the atomic force microscopy (AFM). We measured the magnetic properties of Fe-silicide-NDs using an alternation gradient magnetometer (AGM) at RT sweeping the applied magnetic field within a range of ±5 kOe in in-plane direction. We extracted the magnetization curves (M-H) of Fe-silicide-NDs by subtracting that of Si substrates. Electrical separation among the as-prepared NDs was also verified by surface potential measurements using an AFM/Kelvin force microscopy (KFM) technique as described in detail in our previous works [32-35].

## 5.3 Results and discussion

### 5.3.1 Impact of H<sub>2</sub> pressure of remote H<sub>2</sub> plasma on Fe<sub>3</sub>Si nanodots formation

The Fe/a-Si/Fe trilayer stack on SiO<sub>2</sub> shows a fairly smooth surface morphology with a root-mean-square (RMS) roughness as small as ~0.27 nm, which is almost identical to that of the as-grown SiO<sub>2</sub> surface. The result confirms the uniform surface coverage with the ultrathin Fe/a-Si/Fe trilayer (Fig. 5.1(a)). By exposing the Fe/a-Si/Fe trilayer stack to the H<sub>2</sub>-RP, the formation of NDs with an areal density over 10<sup>11</sup> cm<sup>-2</sup> were observed at the gas pressure in the range from 9 to 27 Pa (Fig. 5.1(b-e)).

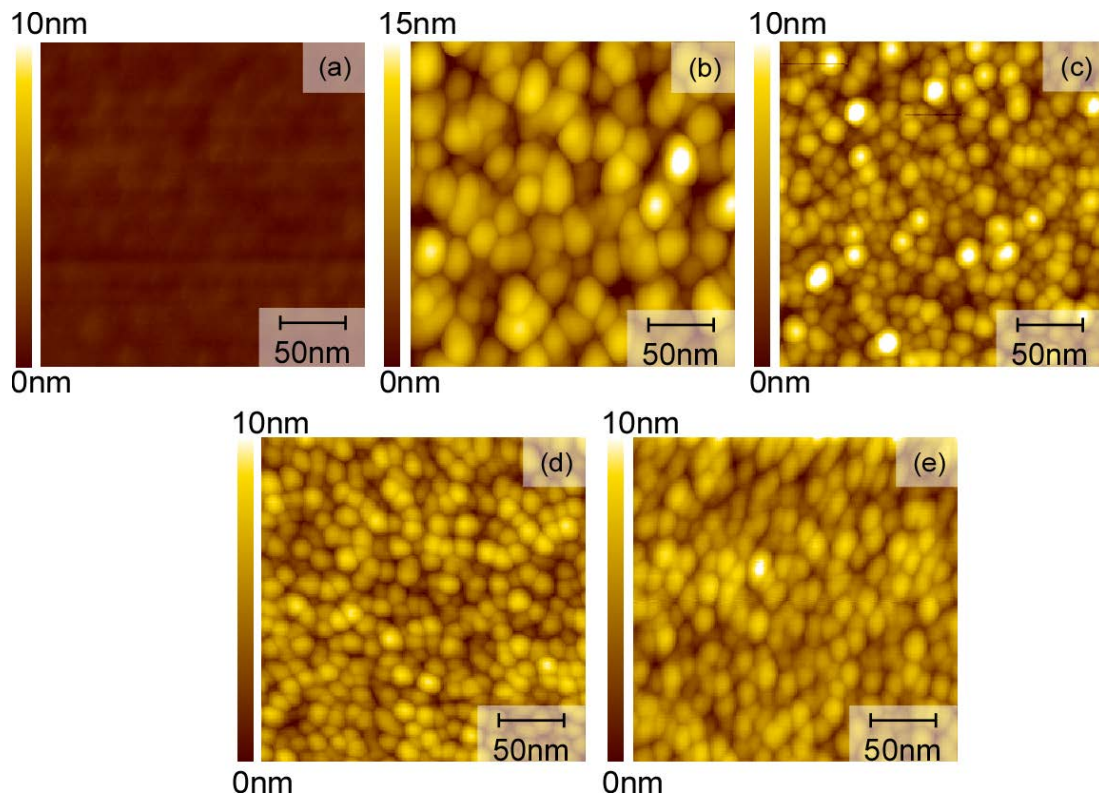


**Fig. 5.1.** Topographic images of Fe/a-Si/Fe ultrathin trilayer stack structures (a) before and after H<sub>2</sub>-RP exposure at gas pressures of 9 Pa (b), 13 Pa (c), 20 Pa (d), and 27 Pa (e).

The size distribution for the NDs was obtained from the AFM images as shown in Fig. 5.2. From the size distribution, average dot heights were evaluated by fitting to a log-normal function. The average dot height and areal dot density evaluated from the AFM images were summarized as a function of the H<sub>2</sub> pressure during RP exposure as shown in Fig.5.3.

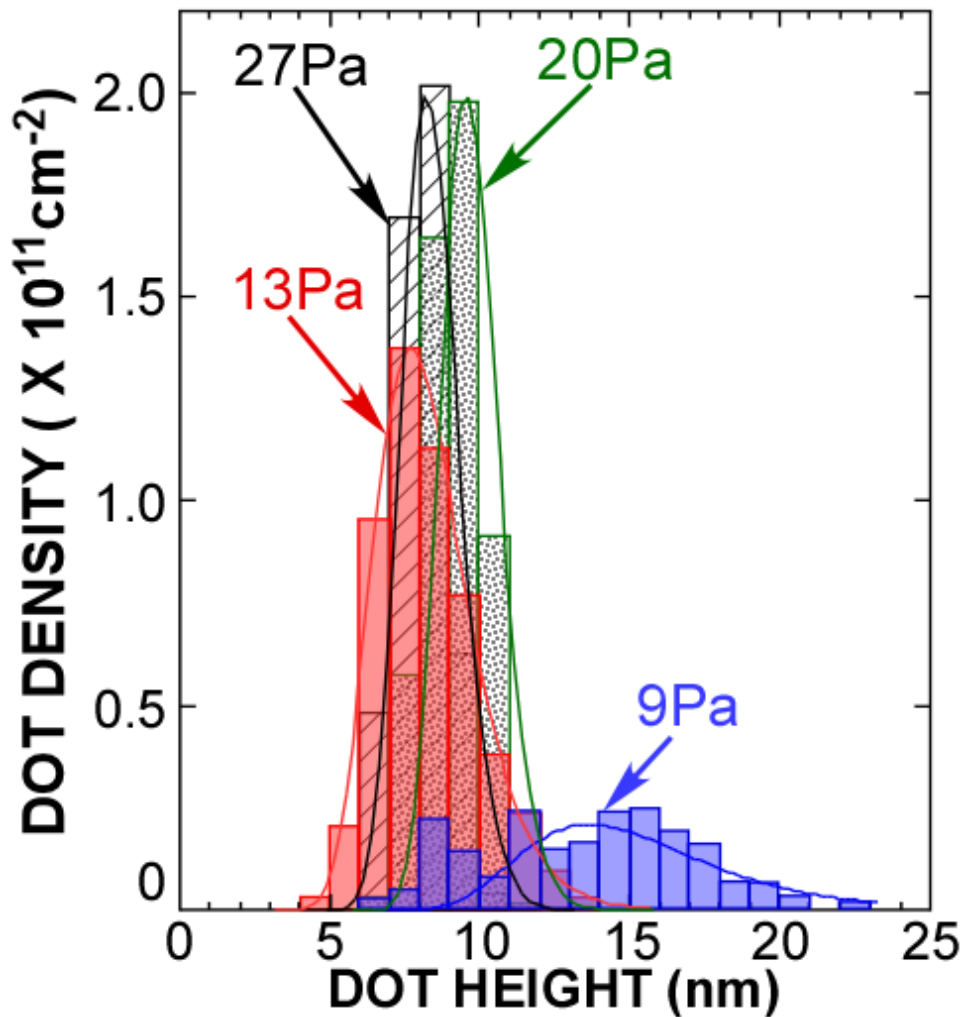


**Fig. 5.2.** Dot height distributions of obtained from AFM images of the samples corresponding to Figs. 5.1 (b)-(e). Solid lines denote the log-normal functions well fitted to the measured distributions.

At the gas pressure of 9 Pa, formation of the NDs with an areal density of  $\sim 2 \times 10^{11}$  cm<sup>-2</sup> and an average height of  $\sim 13.8$  nm was confirmed. With increasing H<sub>2</sub> pressure to 13 Pa, the dot density is increased to  $5 \times 10^{11}$  cm<sup>-2</sup> accompanied with a decrease in the dot height to  $\sim 8$  nm. When the gas pressure is increased over 13 Pa, the areal dot density and the average size tend to be saturated. The result should be explained by

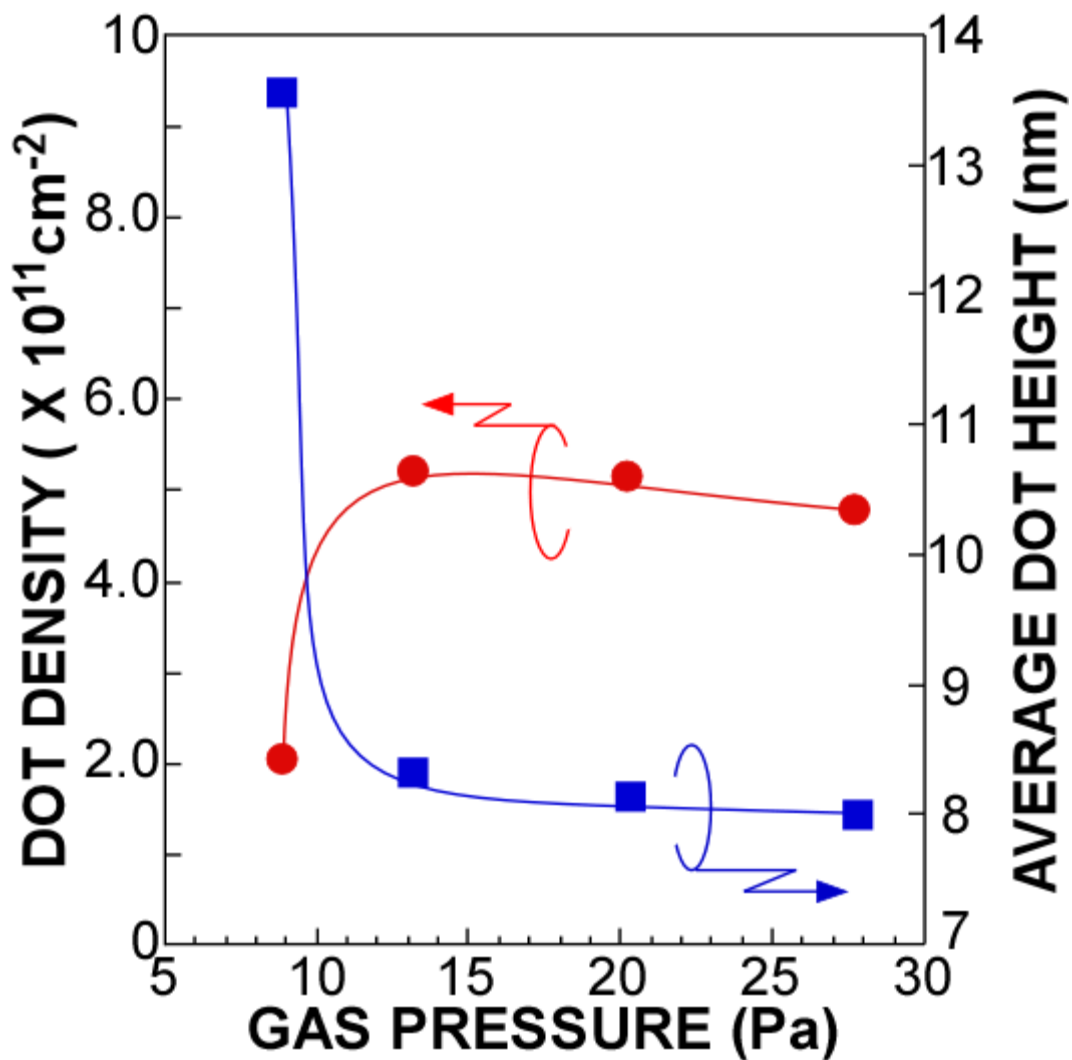


**Fig. 5.3.** Areal density and the average height of NDs formed by exposing Fe/a-Si/Fe ultrathin trilayer stack structures to H<sub>2</sub>-RP as functions of H<sub>2</sub> gas pressure.

the increase in surface temperature with H<sub>2</sub> pressure, as confirmed later, due to the increase in the flux of atomic hydrogen incident to the surface [33], which affect the migration of Fe and Si atoms with the silicidation reaction on the SiO<sub>2</sub> surface, namely resultant dot size and density. Electrical separation among the formed NDs at each condition of H<sub>2</sub> pressure was verified in the similar way described in section 4.3.3, in which surface potential was measured using an AFM/Kelvin force microscopy (KFM) technique as described in detail in our previous works [5]. The difference in surface potential changes due to electron injection before and after the plasma treatment indicates the migration of Fe and/or Si atoms in between the dots to reveal the SiO<sub>2</sub> surface during the H<sub>2</sub>-RP. To determine the Fe-Si chemical composition, X-ray photoelectron spectroscopy (XPS) were measured. From the XPS measurements, we confirmed formation of Fe-silicide where Fe-Si chemical composition ratios were estimated to be approximately 3:1.

### **5.3.2 Room temperature magnetic properties of Fe<sub>3</sub>Si nanodots**

To characterize magnetic properties of these NDs, in-plane magnetization curves (M–H curves) within magnetic field range of  $\pm 5$  kOe were measured by an alternation gradient magnetometer (AGM) at room temperature as shown in Fig. 5.4. M–H curves evidently show a ferromagnetic nature irrespective of the gas pressure. Furthermore, we found that the saturation magnetization ( $M_s$ ) at 20 Pa is estimated to be  $\sim 800$  emu/cc, which is only slightly smaller than that of DO<sub>3</sub> orderd Fe<sub>3</sub>Si (50-nm-thick film) [26]. The smaller magnetization in the case of 20 Pa can be explained by an influence of the

existence of a small amount of natural oxides. However,  $M_s$  for the cases of 9 Pa, 13Pa and 27 Pa are quite smaller than that in case of 20 Pa. To get a better understanding of the difference in  $M_s$ , surface temperature of Fe film was measured during plasma exposure by using a thermocouple covered with a Fe foil as described in detail in our previous works [35]. By exposing the Fe foil to remote plasma of pure  $H_2$ ,

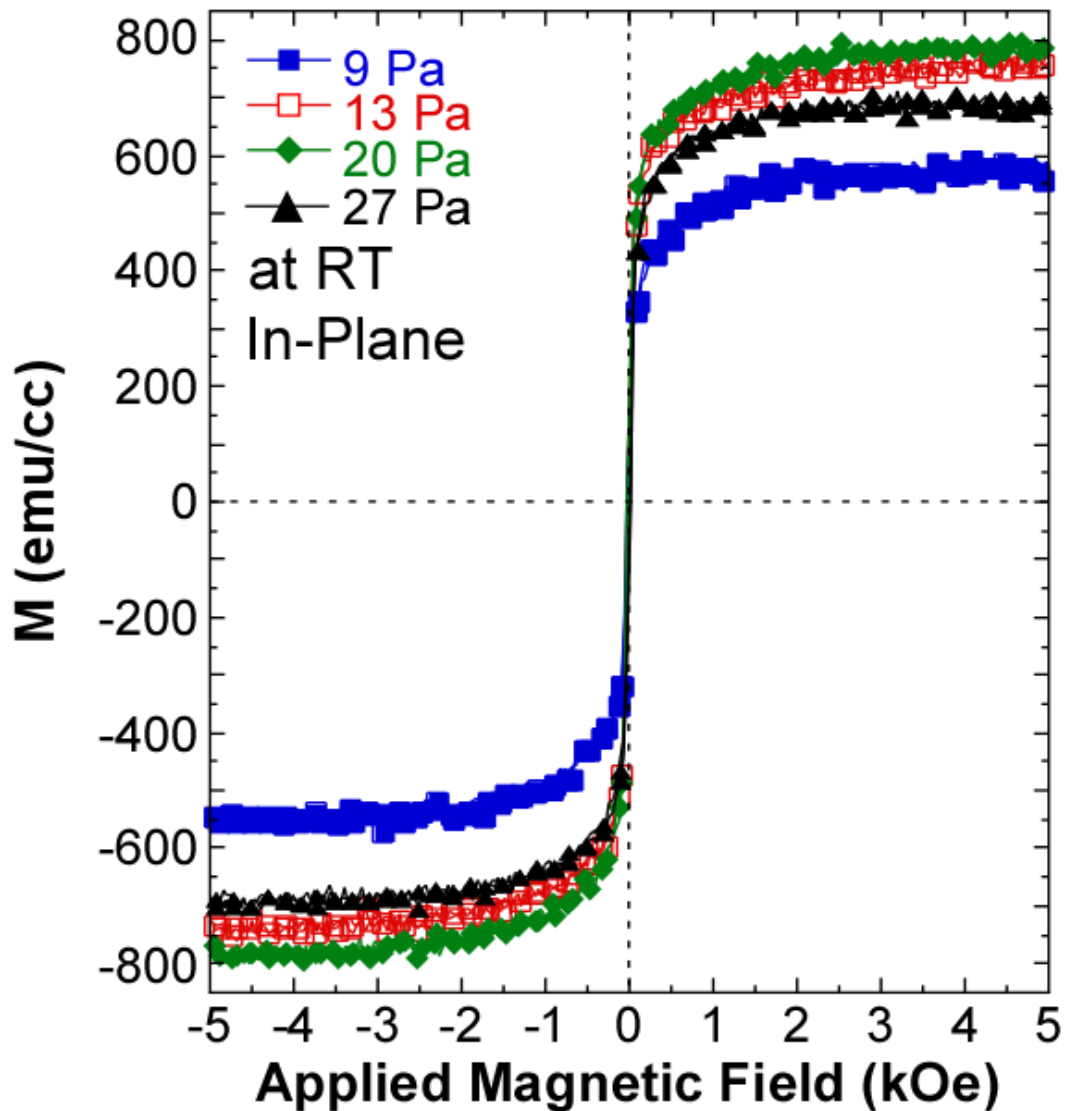


**Fig. 5.4.** In-plane magnetization curves of Fe/a-Si/Fe ultrathin trilayer stack structures taken after  $H_2$ -RP exposure at four different pressures of

the surface temperature was sharply increased and reached its maximum value. The maximum surface temperature measured on the Fe foil and the  $M_s$  of Fe-silicide NDs as functions of the gas pressure are summarized in Fig. 5.5. Obviously, with increasing gas pressure, the maximum surface temperature is increased.

Note that although there are no significant changes in the size and the areal density of

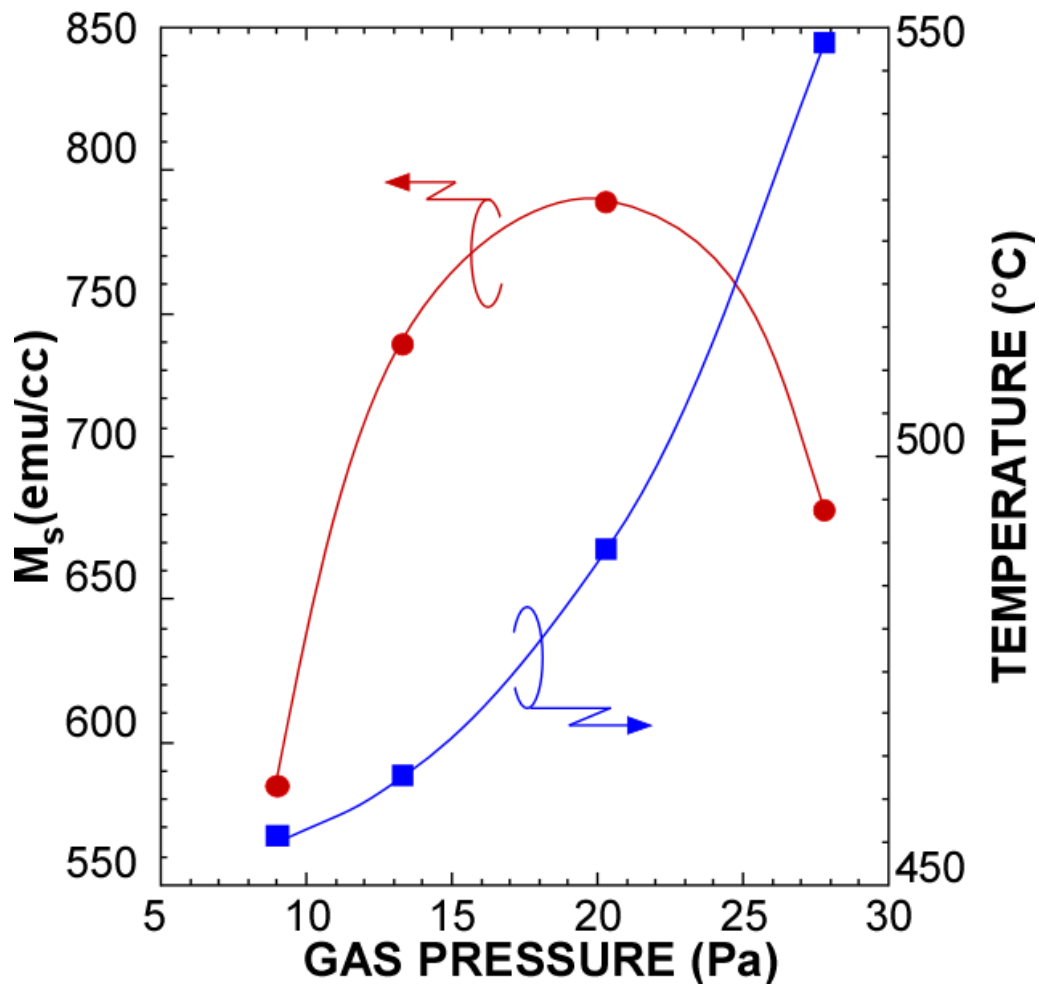


**Fig. 5.5.** Saturation magnetization of Fe/a-Si/Fe ultrathin trilayer stack structures after H<sub>2</sub>-RP exposure and the maximum temperature of Fe foil surface during H<sub>2</sub>-RP exposure as functions of H<sub>2</sub> gas pressure.

the NDs in the H<sub>2</sub> pressure ranging from 13 to 27 Pa, saturation magnetization is increased up to 20 Pa, and with a further increase in the pressure to 27 Pa, a distinct decrease of M<sub>S</sub> was observed. Therefore, the change of the saturation magnetization suggests that the surface temperature contributes to crystalline structure of the NDs.

To get a further insight into the change in the M<sub>S</sub>, the crystalline structures were

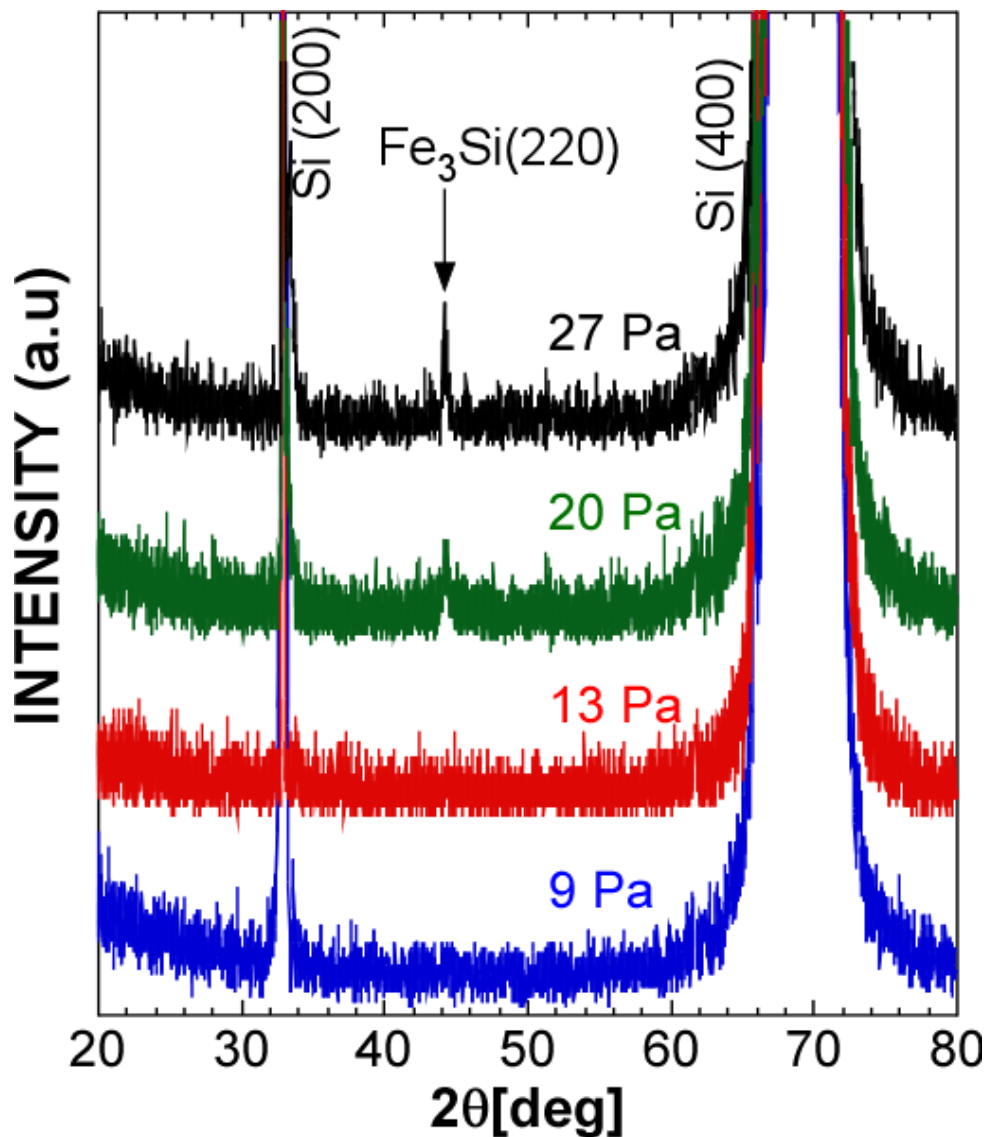


**Fig. 5.6.**  $\theta$ - $2\theta$  XRD patterns of Fe/a-Si/Fe ultrathin trilayer stack structures after H<sub>2</sub>-RP exposure at four different pressures of 9, 13, 20, and 27 Pa.

examined by x-ray diffraction (XRD) measurements. The X-ray diffraction patterns ( $\theta$ - $2\theta$ ) of the NDs exposed at different gas pressures 9, 13, 20, and 27 Pa are shown in Fig. 5.6. Distinct diffraction peaks due to  $Fe_3Si$  (220) plane were observed for the samples formed at 20 and 27 Pa. On the other hand, for the cases of 9 and 13 Pa, no

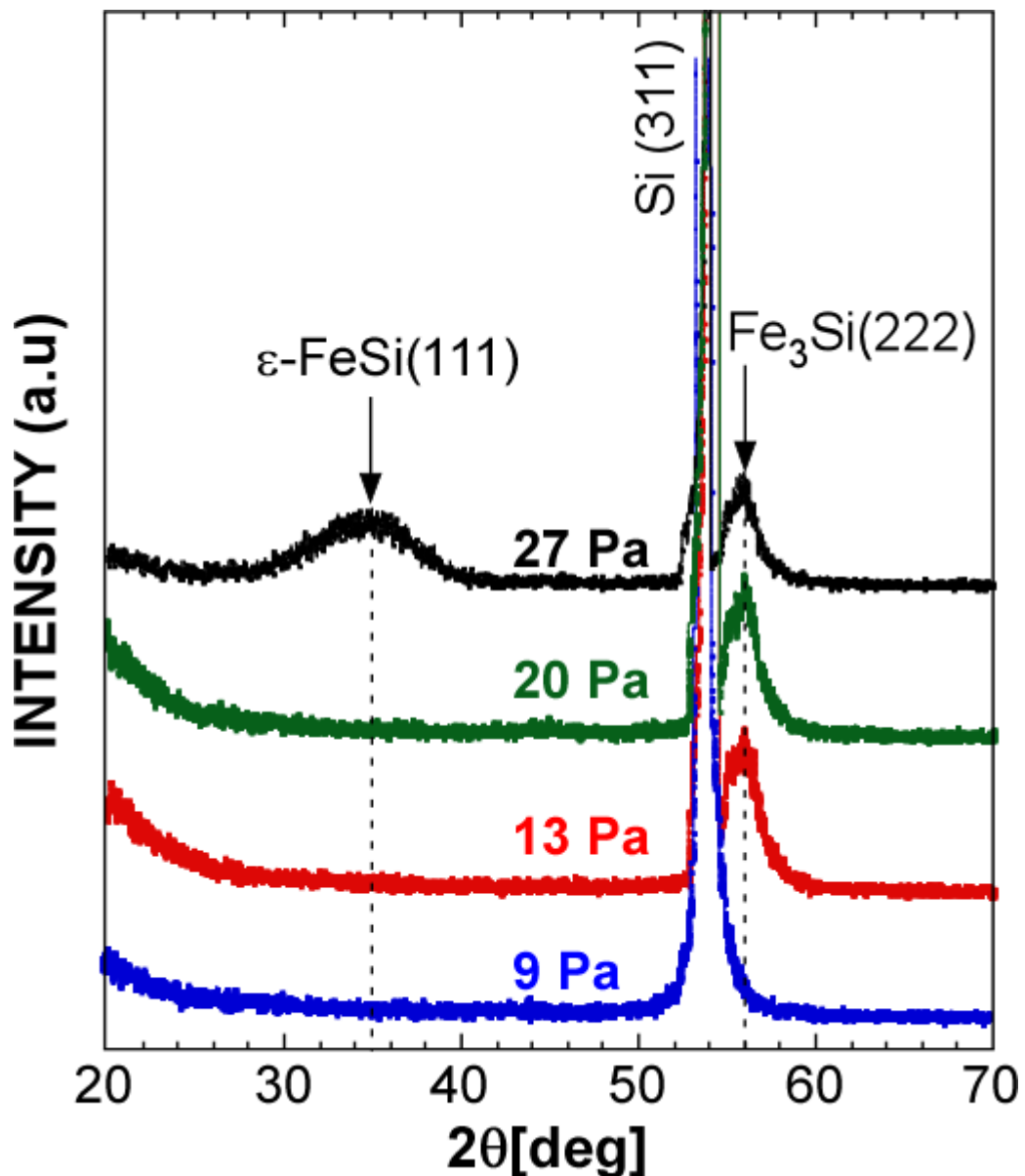


**Fig. 5.7.** Grazing incidence XRD patterns of Fe/a-Si/Fe ultrathin trilayer stack structures after  $H_2$ -RP exposure at four different pressures of 9, 13, 20, and 27 Pa. The X-ray incidence angle was fixed at  $1.75^\circ$ .

characteristic diffraction peaks were observed except for the signals due to Si substrate. These results indicate the formation of Fe<sub>3</sub>Si-NDs when the samples were exposed to the H<sub>2</sub>-RP at 20 and 27 Pa. Because the thickness of the trilayer is very thin, we also measured the XRD by a grazing incidence method with fixed incidence angle of 1.75° as shown in Fig. 5.7. In the case of 9 Pa, there is no peak except for the signals due to the Si substrate. In contrast, in the cases of 13 Pa and over, the XRD patterns of Fe-silicide NDs show distinct diffraction peaks due to Fe<sub>3</sub>Si (222) plane. This result indicates the formation of Fe<sub>3</sub>Si phase above 13 Pa. Here, we note that, in the case of 27 Pa, XRD signals originating from the ε-FeSi (111) plane were also observed. Walser et al. predicted that the first phase compound formed in solid binary couple reactions of bulk equilibrium compounds at temperatures far below the lowest eutectic temperature [36]. As the temperature for annealing is increased, the extent of the interface region increases by diffusion until the region is definitely metastable and nucleation of the first crystalline phase then proceeds [36]. Based on their theory, in Fe-Si binary system, ε-FeSi phase should be firstly formed as the temperature increasing. In our case, since a Fe/a-Si/Fe trilayer stack structures were used and the agglomeration of Fe and Si atoms for the formation of NDs occurred in a three-dimensional direction at nonequilibrium state during H<sub>2</sub>-RP exposure, the diffusion and silicidation reaction mechanism in the interface region of the trilayer become more complicated, which requires more detailed investigation.

Therefore, in our case the reason of the decrease in  $M_s$  at 27Pa is mainly explained by formation of nanocrystalline ε-FeSi phase which is a nonferromagnetic material at room

temperature. According to the above results, the crystalline phase of Fe silicide NDs can be controlled by changing the H<sub>2</sub> pressure.

## **5.4 Conclusions**

We demonstrated a novel technique for formation of Fe<sub>3</sub>Si-NDs on thermally grown SiO<sub>2</sub> with an areal density as high as  $\sim 10^{11}$  cm<sup>-2</sup>, in which the agglomeration with cohesive action of Fe and Si atoms on the SiO<sub>2</sub> was promoted by H<sub>2</sub>-RP exposure without external heating. By controlling the thickness ratio of Fe/a-Si/Fe trilayer stack structure and gas pressure of H<sub>2</sub>-RP, the crystalline phase of Fe-silicide NDs can be controlled. This technique is very promising for the low-temperature fabrication of various phases of Fe-silicide NDs.

## References

- [1] J. Moss and P. J. Brown, *J. Phys. F Met. Phys.* **2**, 358 (1972).
- [2] M. C. Bost and J. E. Mahan, *J. Appl. Phys.* **58**, 2696 (1985).
- [3] N. Christensen, *Phys. Rev. B* **42**, 7148 (1990).
- [4] D. Leong, M. Harry, K. J. Reeson, and K. P. Homewood, *Nature* **387**, 686 (1997).
- [5] T. Yoshitake, T. Ogawa, D. Nakagauchi, D. Hara, M. Itakura, et al., *Appl. Phys. Lett.* **89**, 3 (2006).
- [6] K. Takeda, T. Yoshitake, D. Nakagauchi, T. Ogawa, D. Hara, et al., *Jpn. J. Appl. Phys.* **46**, 7846 (2007).
- [7] S.-J. Oh, J. W. Allen, and J. M. Lawrence, *Phys. Rev. B* **35**, 2267 (1987).
- [8] V. Kinsinger, I. . Dezsi, P. . Steiner, and G. Langouche, *J. Physics-Condensed Matter* **2**, 4955 (1990).
- [9] O. K. von Goldbeck, *IRON—Binary Phase Diagrams* (Springer Berlin Heidelberg, Berlin, Heidelberg, 1982).
- [10] W. a. Hines, a. H. Menotti, J. I. Budnick, T. J. Burch, T. Litrenta, et al., *Phys. Rev. B* **13**, 4060 (1976).
- [11] V. Niculescu, J. I. Budnick, W. a. Hines, K. Raj, S. Pickart, et al., *Phys. Rev. B* **19**, 452 (1979).
- [12] V. Niculescu, T. J. Burch, and J. I. Budnick, *J. Magn. Magn. Mater.* **39**, 223 (1983).
- [13] Y. Maeda, T. Jonishi, K. Narumi, Y. Ando, K. Ueda, et al., *Appl. Phys. Lett.* **91**, 171910 (2007).
- [14] T. Yoshitake, D. Nakagauchi, T. Ogawa, M. Itakura, N. Kuwano, et al., *Appl. Phys. Lett.* **86**, 262505 (2005).
- [15] R. A. de Groot, F. M. Mueller, P. G. van Engen, and K. H. J. Buschow, *Phys. Rev. Lett.* **50**, 2024 (1983).
- [16] K. Ueda, R. Kizuka, H. Takeuchi, A. Kenjo, T. Sadoh, et al., *Thin Solid Films* **515**,

- 8250 (2007).
- [17] K. Ueda, Y. Ando, M. Kumano, T. Sadoh, Y. Maeda, et al., *Appl. Surf. Sci.* **254**, 6215 (2008).
- [18] M. Miyao, K. Ueda, Y. Ando, M. Kumano, T. Sadoh, et al., *Thin Solid Films* **517**, 181 (2008).
- [19] Y. Nakamura and M. Ichikawa, *Jpn. J. Appl. Phys.* **54**, 07JD01 (2015).
- [20] L. Yin, D. Xiao, Z. Gai, T. Z. Ward, N. Widjaja, et al., *Phys. Rev. Lett.* **104**, 167202 (2010).
- [21] C.-K. Yin, M. Murugesan, J.-C. Bea, M. Oogane, T. Fukushima, et al., *Jpn. J. Appl. Phys.* **46**, 2167 (2007).
- [22] T. Yoshitake, D. Nakagauchi, and K. Nagayama, *Jpn. J. Appl. Phys.* **42**, L849 (2003).
- [23] D. Nakagauchi, T. Yoshitake, and K. Nagayama, *Vacuum* **74**, 653 (2004).
- [24] G. Molnár, L. Dózsa, R. Erdélyi, Z. Vértesy, and Z. Osváth, *Appl. Surf. Sci.* **357**, 573 (2015).
- [25] K. Hamaya, K. Ueda, Y. Kishi, Y. Ando, T. Sadoh, et al., *Appl. Phys. Lett.* **93**, 132117 (2008).
- [26] Y. Ando, K. Ichiba, S. Yamada, E. Shikoh, T. Shinjo, et al., *Phys. Rev. B* **88**, 140406 (2013).
- [27] T. Sadoh, H. Takeuchi, K. Ueda, A. Kenjo, and M. Miyao, *Jpn. J. Appl. Phys.* **45**, 3598 (2006).
- [28] Y. Nakamura, S. Amari, S.-P. Cho, N. Tanaka, and M. Ichikawa, *Jpn. J. Appl. Phys.* **50**, 015501 (2011).
- [29] Y. Nakamura, K. Fukuda, S. Amari, and M. Ichikawa, *Thin Solid Films* **519**, 8512 (2011).
- [30] T. Harianto, K. Sadakuni, H. Akinaga, and T. Suemasu, *Jpn. J. Appl. Phys.* **47**, 6310 (2008).

- [31] H. Zhang, K. Makihara, A. Ohta, M. Ikeda, and S. Miyazaki, *Jpn. J. Appl. Phys.* **55**, 01AE20 (2016).
- [32] K. Makihara, K. Shimanoe, M. Ikeda, S. Higashi, and S. Miyazaki, *Jpn. J. Appl. Phys.* **47**, 3099 (2008).
- [33] K. Makihara, K. Shimanoe, A. Kawanami, M. Ikeda, S. Higashi, et al., *J. Optoelectron. Adv. Mater.* **12**, 626 (2010).
- [34] A. Kawanami, K. Makihara, M. Ikeda, and S. Miyazaki, *Jpn. J. Appl. Phys.* **49**, 08JA04 (2010).
- [35] H. Zhang, R. Fukuoka, Y. Kabeya, K. Makihara, and S. Miyazaki, *Adv. Mater. Res.* **750-752**, 1011 (2013).
- [36] R. M. Walser and R. W. Bené, *Appl. Phys. Lett.* **28**, 624 (1976).

## Chapter 6

### Conclusions

The author demonstrated a novel technique for the formation of Fe-NDs and Fe-silicide NDs (ferromagnetic Fe<sub>3</sub>Si and semiconducting β-FeSi<sub>2</sub> phase) on SiO<sub>2</sub> with an areal density as high as ~10<sup>11</sup> cm<sup>-2</sup>. The remote H<sub>2</sub> plasma (H<sub>2</sub>-RP) is effective for the Fe-based nanodot formation caused by local heating because of the reduction of native oxide on the Fe surface and subsequent recombination of hydrogen atoms absorbed on the Fe surface. The Fe/Si/Fe trilayer stack is a key to form the Fe-silicide NDs due to agglomeration and simultaneous silicidation reaction. The stoichiometry of the Fe-silicide can be simply determined by the initial ratio of the film thickness of the Fe/Si/Fe trilayer stack and the phase structure can be controlled by the parameters of H<sub>2</sub>-RP which change the surface temperature depending on atomic hydrogen flux. The Fe-based silicides NDs exhibit a potential advantage for the application to the magnetic NDs memory devices. The principal results of Chapter 3 to 5 are summarized below.

In Chapter 3, the author addressed the nanodot formation from easily oxidizable metal Fe by exposing an electron-beam-evaporated Fe film simply to H<sub>2</sub>-RP without external heating. Emphasis was laid on how effective remote hydrogen plasma

treatment is on the metal NDs formation. The author has found that the initial thickness of Fe films and parameters of H<sub>2</sub>-RP are key factors on the Fe-NDs formation. The Fe-NDs formation processes including a reduction reaction in the surface Fe oxide and correlations between the dot size and these factors were elaborated. These research efforts on the formation of Fe-NDs have great significance for the formation of Fe-based silicide NDs on SiO<sub>2</sub>.

In chapter 4, A Fe/a-Si/Fe trilayer stack structure was employed to be exposed to the remote H<sub>2</sub> plasma without any external heating. The formation of NDs can be attributed to the heat generation due to the recombination of hydrogen atoms on the clean Fe surface, which induce the silicidation reaction accompanied by the agglomeration of Fe and Si atoms on the SiO<sub>2</sub> surface. The formation of a crystalline  $\beta$ -FeSi<sub>2</sub> phase was determined. The electrical separation among the  $\beta$ -FeSi<sub>2</sub> NDs was confirmed from changes in the surface potential due to the charging of the dots. The surface potential of the NDs was changed in a stepwise manner with respect to the tip voltage applied for charge injection by using AFM because of the multistep electron injection to and extraction from the semiconductor  $\beta$ -FeSi<sub>2</sub> NDs. This approach is very promising for the formation of alloy NDs on SiO<sub>2</sub> without any annealing treatment.

In chapter 5, the author described the method to control the crystalline phase of the Fe-silicide NDs, in which he extended the results of Chapter 4 to the formation of high density Fe-silicide NDs on SiO<sub>2</sub> by controlling the ratio of initial film thickness of Fe/a-Si/Fe trilayer stacks and H<sub>2</sub> gas pressure. The influences of the H<sub>2</sub>-RP gas pressure on magnetic properties and the crystal phase of Fe-silicide NDs were

investigated. With increasing  $H_2$  pressure, namely the surface temperature of the sample, saturation magnetization,  $M_s$ , was increased to reach its peak, and then decreased. From the results of XRD measurement, we can conclude that the reasons of the increase and decrease in  $M_s$  are mainly explained by the growth of ferromagnetic  $Fe_3Si$  phase and formation of nanocrystalline  $\epsilon$ - $FeSi$  phase which is nonmagnetic at room temperature, respectively. These results suggest that, by controlling the thickness ratio of Fe/a-Si/Fe trilayer stack structure and gas pressure of  $H_2$ -RP, the crystalline phase of Fe-silicide NDs can be controlled.

In conclusion, this technique is very effective for the low-temperature fabrication of various phases of Fe-silicide NDs.

In this work, there remain several issues that could not be accomplished within the experimental work of this thesis and they are listed below:

In order to realize the application of the Fe-silicide NDs to the practical devices such as floating gate memory, light-emitting diode and Si-based spintronic devices, sophisticating the nanodots formation and the crystalline phase control processes is mandatory. Further examination of phase structure and physical properties of Fe-silicide NDs may lead to discovery of novel functions unique in Fe-silicide NDs. Throughout this work, we have found that the initial thickness of Fe films and parameters of  $H_2$ -RP are critical factors for the control not only of dot density but also of phase structures. However, the layer thickness and  $H_2$ -RP parameters were not optimized to control the phase structural and magnetic properties of Fe-silicides. The optimization of these factors and the establishment of Fe-silicide NDs phase diagram

are needed.

Based on the phase diagram of the bulk Fe-Si binary system,  $\epsilon$ -FeSi phase should be firstly formed as the temperature increase. However, since a Fe/a-Si/Fe trilayer stack structures were used, the diffusion and silicidation reaction mechanism in the interface region of the trilayer become very complicated in this work, which needs more detailed investigation.

For the  $\beta$ -FeSi<sub>2</sub> NDs, which are expected to be applied to the light-emitting devices, the light emission characteristics should be evaluated by luminescence measurement. In the future, we will fabricate a three-dimensional stacked structure with the  $\beta$ -FeSi<sub>2</sub> NDs separated by ultrathin Si oxide interlayers to achieve the efficient light emission.

As mentioned in the introduction of chapter 1, the DO<sub>3</sub> ordered Fe<sub>3</sub>Si is a promising candidate for spintronic applications due to the quasi half-metallic behavior of the Heusler alloy Fe<sub>3</sub>Si. Although we have obtained the crystalline Fe<sub>3</sub>Si NDs, in which the value of saturation magnetization was very close to the DO<sub>3</sub> ordered Fe<sub>3</sub>Si thin film (50-nm-thick), we have to find a way to improve the ordering level of the DO<sub>3</sub> ordered Fe<sub>3</sub>Si NDs to improve the spin polarization ratio. For the application of Fe<sub>3</sub>Si NDs to memory devices such as spin dependent floating gate memory, electronic transport characteristics should be examined in magnetic tunnel junction with the NDs.

The author hopes that the research efforts could provide guideline for the formations of various phase metal-silicides or -germanides NDs based Si or Ge, which offers some opportunities in a next generation information technologies employing semiconductor or spintronic devices with innovative concepts.

## **List of paper and international conference**

### **Journal publications (Peer reviewed)**

1. **H. Zhang**, R. Fukuoka, Y. Kabeya, K. Makihara and S. Miyazaki, “High Density Formation of Iron Nanodots on SiO<sub>2</sub> Induced by Remote Hydrogen Plasma”, *Advanced Materials Research Vols. 750-752*, 1011 (2013).
2. **Hai Zhang**, Katsunori Makihara, Akio Ohta and Seiichi Miyazaki, “Formation and Characterization of High Density FeSi Nanodots on SiO<sub>2</sub> Induced by Remote H<sub>2</sub> Plasma”, *Jpn. J. Appl. Phys.* 55, 01AE20 (2016).

### **Other publications**

1. Akio OHTA, Chong LIU, Takashi ARAI, Daichi TAKEUCHI, **Hai ZHANG**, Katsunori MAKIHARA, and Seiichi MIYAZAKI, “Resistance-Switching Characteristics of Si-Rich Oxide Evaluated by Using Ni Nanodots as Electrodes in Conductive AFM Measurements.” *IEICE Transactions on Electronics E98.C*, 406 (2015).
2. Fukuoka, Ryo, Katsunori Makihara, **Hai Zhang**, Akio Ohta, Takeshi Kato, Satoshi Iwata, Mitsuhsa Ikeda and Seiichi Miyazaki, “High Density Formation of FePt Alloy Nanodots Induced by Remote Hydrogen Plasma and Characterization of Their Magnetic Properties.” *Transactions of the Materials Research Society of Japan*, 40, 347 (2015).

### **International conferences**

1. **H. Zhang**, A. Ohta, K. Makihara and S. Miyazaki, “High Density Formation of Fe-silicide Nanodots Induced by Remote H<sub>2</sub> Plasma and Characterization of Their Crystalline Structure and Magnetic Properties”, *The 37th International Symposium on Dry Process (DPS2015)*, Nov. 5-6, 2015, Awaji Island, Japan, E-1.
2. **Hai Zhang**, Akio Ohta, Katsunori Makihara, Seiichi Miyazaki, “High Density Formation of Fe<sub>3</sub>Si-nanodots on ultrathin SiO<sub>2</sub> Induced by Remote Hydrogen Plasma”, *The 17th Annual Conference and 6th International Conference of the*

- Chinese Society of Micro-Nano Technology(CSMNT2015), Oct.11-14, 2015, Shanghai, China, 96818.
3. **Hai Zhang**, Akio Ohta, Katsunori Makihara, Seiichi Miyazaki, “High Density Formation of Fe silicide-nanodots on SiO<sub>2</sub> Induced by Remote H<sub>2</sub>-plasma”, The 21st Korea-Japan WorkShop on Advanced Plasma Processes and Diagnostics & The Workshop for NU-SKKU Joint Institute for Plasma-Nano Materials, Oct. 3-4, 2015, Yangyang, Republic of Korea.
  4. **Hai Zhang**, Katsunori Makihara, Akio Ohta, and Seiichi Miyazaki, “Formation and Characterization of High Density FeSi Nanodots on SiO<sub>2</sub> Induced by Remote H<sub>2</sub> Plasma” 7<sup>th</sup> International Symposium on Advanced Plasma Science and its Applications for Nitrides and Nano materials / 8<sup>th</sup> International Conference on Plasmas-Nano Technology & Science (ISPlasma2015 / IC-PLANTS2015), March 26-31, 2015, Nagoya University, Nagoya, Japan, C1-P-84L.
  5. **H. Zhang**, K. Makihara, A. Ohta, M. Ikeda and S. Miyazaki, “High Density Formation of Fe-Silicide Nanodots Induced by Remote Hydrogen Plasma”, 8th International Workshop on New Group IV Semiconductor Nanoelectronics and JSPS Core-to Core Program Joint Seminar "Atomically Controlled Processing for Ultralarge Scale Integration" (Sendai, Jan.29-30, 2015), O-13.
  6. Y. Kabeya, **H. Zhang**, A. Ohta, K. Makihara and S. Miyazaki, “Impact of Magnetic-Field Application on Electron Transport Through FePt Alloy Nanodots”, 8th International WorkShop on New Group IV Semiconductor Nanoelectronics and JSPS Core-to-Core Program Joint Seminar "Atomically Controlled Processing for Ultralarge Scale Integration" (Sendai, Jan.29-30, 2015), P-05.
  7. T. Nguyen, A. Ohta, D. Takeuchi, **H. Zhang**, K. Makihara and S. Miyazaki, “Impact of Remote Hydrogen Plasma on Micro-roughness and Electronic States at 4H-SiC(0001) Surface”, 8th International WorkShop on New Group IV Semiconductor Nanoelectronics and JSPS Core-to-Core Program Joint Seminar "Atomically Controlled Processing for Ultralarge Scale Integration" (Sendai, Jan.29-30, 2015), P-08.
  8. **H. Zhang**, K. Makihara, A. Ohta, M. Ikeda and S. Miyazaki, “High Density Formation of Fe-Silicide Nanodots on SiO<sub>2</sub> Induced by Remote H<sub>2</sub> Plasma”, 27th International Microprocesses and Nanotechnology Conference (MNC), Fukuoka, November 4-7, 2014, 5C-2-4.

9. A. Ohta, C. Liu, T. Arai, D. Takeuchi, **H. Zhang**, K. Makihara and S. Miyazaki, “Characterization of Resistance-Switching of Ni Nano-dot/SiO<sub>x</sub>/Ni Diodes”, International Union Material Research Society - International Conference in Asia 2014 (IUMRS-ICA 2014), Fukuoka, Aug. 24-30, 2014, D5-O25-008.
10. Y. Kabeya, **H. Zhang**, R. Fukuoka, A. Ohta, K. Makihara and S. Miyazaki, “Impact of Magnetic-Field Application on Electron Transport Through CoPt Alloy Nanodots”, International Union Material Research Society - International Conference in Asia 2014 (IUMRS-ICA 2014), Fukuoka, Aug. 24-30, 2014, D5-P26-004.
11. K. Makihara, R. Fukuoka, **H. Zhang**, A. Ohta, Y. Tokuda, T. Kato, S. Iwata, and S. Miyazaki, “Crystalline Structure and Magnetic Properties of FePt Alloy Nanodots”, International Union Material Research Society - International Conference in Asia 2014 (IUMRS-ICA 2014), Fukuoka, Aug. 24-30, 2014, D5-P26-005.
12. T. Nguyen, **H. Zhang**, D. Takeuchi, A. Ohta, K. Makihara, H. Murakami, and S. Miyazaki, “Impact of Remote H<sub>2</sub> Plasma on Surface Roughness of 4H-SiC(0001)”, International Union Material Research Society - International Conference in Asia 2014 (IUMRS-ICA 2014), Fukuoka, Aug. 24-30, 2014, D5-P26-016.
13. A. Ohta, C. Liu, T. Arai, D. Takeuchi, **H. Zhang**, K. Makihara and S. Miyazaki, “Resistance-Switching Characteristics of Si-rich Oxide as Evaluated by Using Ni Nanodots as Electrodes in Conductive AFM Measurements”, 2014 Asia-Pacific Workshop on Fundamentals and Applications of Advanced Semiconductor Devices (AWAD 2014), (Kanazawa, Ishikawa, July1-3 2014) 6B-4.
14. **Hai Zhang**, Katsunori Makihara, Ryo Fukuoka, Yuuki Kabeya and Seiichi Miyazaki “Study on Formation of High Density Fe-Nanodots on Ultrathin SiO<sub>2</sub> Induced by Remote H<sub>2</sub> Plasma Exposure”, 6<sup>th</sup> International Symposium on Advanced Plasma Science and its Applications for Nitrides and Nano materials / 7<sup>th</sup> International Conference on Plasmas-Nano Technology & Science (ISPlasma2014 / IC-PLANTS2014), March 2-6, 2014, Meijo Universty, Nagoya, Japan.
15. Ryo Fukuoka, **Hai Zhang**, Katsunori Makihara, Yoshihiro Tokuoka, Takeshi Kato, Satoshi Iwata and Seiichi Miyazaki “High Density Formation of FePt Alloy Nanodots Induced by Remote Hydrogen Plasma and Characterization of Their Magnetic Properties”, 7<sup>th</sup> International WorkShop on New Group IV

- Semiconductor Nanoelectronics and JSPS Core-to-Core Program Joint Seminar "Atomically Controlled Processing for Ultralarge Scale Integration", Tohoku University, Sendai, Japan, January 27-28, 2014, P-05.
16. Yuuki Kabeya, **Hai Zhang**, Ryo Fukuoka, Katsunori Makihara and Seiichi Miyazaki "Formation of High-Density Magnetic Nanodots on Ultrathin SiO<sub>2</sub> Induced by Remote H<sub>2</sub> Plasma", 7th International WorkShop on New Group IV Semiconductor Nanoelectronics and JSPS Core-to-Core Program Joint Seminar "Atomically Controlled Processing for Ultralarge Scale Integration", Tohoku University, Sendai, Japan, January 27-28, 2014, P-10.
17. R. Fukuoka, **H. Zhang**, K. Makihara, Y. Tokuoka, T. Kato, S. Iwata and S. Miyazaki, "High density formation of FePt alloy nanodots on SiO<sub>2</sub> induced by remote hydrogen plasma", Magnetics and Optics Research International Symposium (MORIS2013), Omiya, December 2-5, 2013, We-P-07.
18. **H. Zhang**, R. Fukuoka, Y. Kabeya, K. Makihara and S. Miyazaki, "Formation of High Density Fe-Nanodots on Ultrathin SiO<sub>2</sub> Induced by Remote H<sub>2</sub> Plasma", 2013 International Symposium on Dry Process (DPS 2013), Jeju, Korea, August 29-30 2013, P-37.
19. **H. Zhang**, R. Fukuoka, Y. Kabeya, K. Makihara and S. Miyazaki, "High Density Formation of Iron Nanodots on SiO<sub>2</sub> Induced by Remote Hydrogen Plasma", 3rd International Conference on Advanced Engineering Materials and Technology (AEMT 2013), Zhangjiajie, China, May 11-12, 2013, AE8668.
20. R. Fukuoka, **H. Zhang**, Y. Kabeya, K. Makihara, A. Ohta, M. Ikeda and S. Miyazaki, "High Density Formation of CoPt Alloy Nanodots Induced by Remote H<sub>2</sub> Plasma", The 8th International Conference on Silicon Epitaxy and Heterostructures (ICSI-8) and the 6th International Symposium on Control of Semiconductor Interfaces (ISCSI-VI), Fukuoka, June 3-7, 2013, P2-37.
21. R. Fukuoka, **H. Zhang**, Y. Kabeya, K. Makihara, A. Ohta and S. Miyazaki, "High Density Formation and Characterization of CoPt Alloy Nanodots as Memory Nodes", 6th International WorkShop on New Group IV Semiconductor Nanoelectronics and JSPS Core-to Core Program Joint Seminar "Atomically Controlled Processing for Ultralarge Scale Integration" (Sendai, Feb. 22-23, 2013), 10.

22. **Hai Zhang**, Masaya Ichimura “ Fabrication of CuO/ZnO hetero-structure solar cells by paste coating ”, The 5th International Conference on PLASMA-Nano Technology & Science (IC-PLANTS 2012), Inuyama, Aichi, Japan, March 9-10, 2012, P-51.